

AD-A173 633

DEVELOPMENT OF MODELS FOR INFRARED EMISSION IN THE

UPPER ATMOSPHERE(U) ARCON CORP WALTHAM MA

P P WINTERSTEINER ET AL 01 MAY 86 AFGL-TR-86-0163

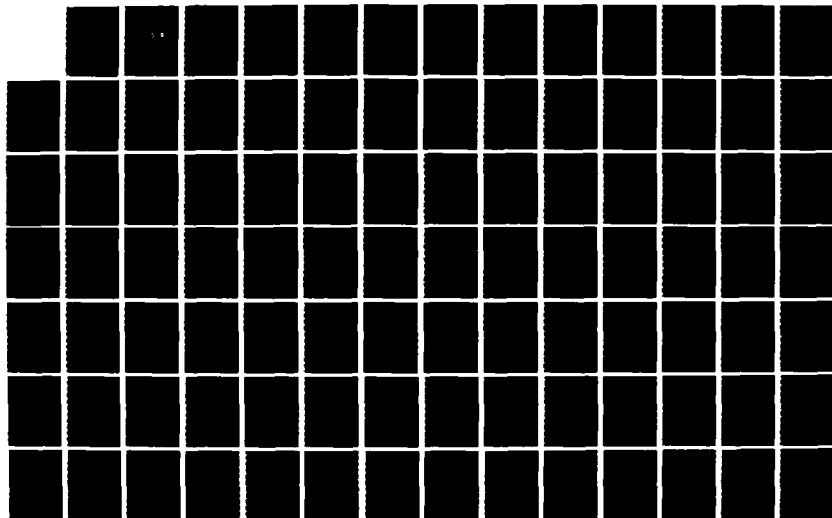
F19628-84-C-0071

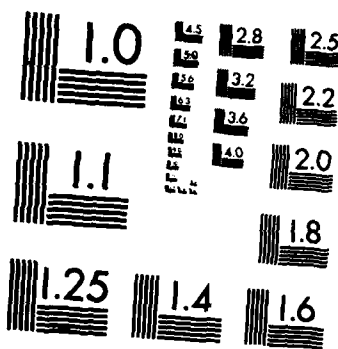
1/2

UNCLASSIFIED

F/G 4/1

NL





MICROCOPY RESOLUTION TEST CHART
NATIONAL BUREAU OF STANDARDS-1963-A

AFGL-TR-86-0163

Development of Models for Infrared Emission
in the Upper Atmosphere

Peter P. Wintersteiner
Robert A. Joseph

Arcon Corporation
260 Bear Hill Road
Waltham, MA 02154

DTIC
SELECTED
NOV 04 1986
S D

1 May 1986

Final Report
5 January 1984-4 January 1985


APPROVED FOR PUBLIC RELEASE; DISTRIBUTION UNLIMITED


AIR FORCE GEOPHYSICS LABORATORY
AIR FORCE SYSTEMS COMMAND
UNITED STATES AIR FORCE
HANSOM AIR FORCE BASE, MASSACHUSETTS 01731

AD-A115 633

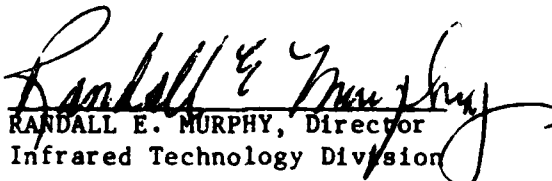
DTIC FILE COPY

"This technical report has been reviewed and is approved for publication"


ARTHUR CORMAN, Contract Manager
Infrared Dynamics Branch
Infrared Technology Division


ROBERT R. O'NEIL, Chief
Infrared Dynamics Branch
Infrared Technology Division

FOR THE COMMANDER


RANDALL E. MURPHY, Director
Infrared Technology Division

This report has been reviewed by the ESD Public Affairs Office (PA) and is releasable to the National Technical Information Service (NTIS).

Qualified requestors may obtain additional copies from the Defense Technical Information Center. All others should apply to the National Technical Information Service.

If your address has changed, or if you wish to be removed from the mailing list, or if the addressee is no longer employed by your organization, please notify AFGL/DAA, Hanscom AFB, MA 01731. This will assist us in maintaining a current mailing list.

Do not return copies of this report unless contractual obligations or notices on a specific document requires that it be returned.

REPORT DOCUMENTATION PAGE

1a. REPORT SECURITY CLASSIFICATION Unclassified			1b. RESTRICTIVE MARKINGS		
2a. SECURITY CLASSIFICATION AUTHORITY			3. DISTRIBUTION/AVAILABILITY OF REPORT Approved for public release; Distribution unlimited		
2b. DECLASSIFICATION/DOWNGRADING SCHEDULE			5. MONITORING ORGANIZATION REPORT NUMBER(S) AFGL-TR-86-0163		
4. PERFORMING ORGANIZATION REPORT NUMBER(S)			7a. NAME OF MONITORING ORGANIZATION Air Force Geophysics Laboratory		
6a. NAME OF PERFORMING ORGANIZATION Arcon Corporation		6b. OFFICE SYMBOL (If applicable)		7b. ADDRESS (City, State and ZIP Code) Hanscom AFB Massachusetts 01731	
6c. ADDRESS (City, State and ZIP Code) 260 Bear Hill Road Waltham, MA 02154		8a. NAME OF FUNDING/SPONSORING ORGANIZATION		8b. OFFICE SYMBOL (If applicable)	
8c. ADDRESS (City, State and ZIP Code)		9. PROCUREMENT INSTRUMENT IDENTIFICATION NUMBER F19628-84-C-0071			
11. TITLE (Include Security Classification) Development of Models for Infrared Emission in the Upper Atmosphere		10. SOURCE OF FUNDING NOS.		15. PAGE COUNT 98	
12. PERSONAL AUTHOR(S) Peter P. Wintersteiner, Robert A. Joseph		PROGRAM ELEMENT NO. 61102F		PROJECT NO. 2310	
13a. TYPE OF REPORT Final Report		13b. TIME COVERED FROM 5 Jan 84 TO 4 Jan 85		TASK NO. G4	
14. DATE OF REPORT (Yr., Mo., Day) 1985 May 1		16. SUPPLEMENTARY NOTATION		WORK UNIT NO. BC	
17. COSATI CODES		18. SUBJECT TERMS (Continue on reverse if necessary and identify by block number)			
FIELD	GROUP	SUB. GR.	Infrared emission, vibrational temperatures, non-LTE		
			transmission, auroral radiance, ← AARC		
			band radiance, line-by-line Voigt		
19. ABSTRACT (Continue on reverse if necessary and identify by block number)					
<p>The efforts summarized in this final report all relate to modelling infrared emission from non-LTE regions of the upper atmosphere. Included are (1) the results of ^{the} our study of emission from solar-pumped CO₂ in the 2.7 μm region and a description of the methods ^{we} used to calculate the solar pumping rates and the vibrational temperatures; (2) improvements ^{we} made in ^{the} our non-LTE radiance code, NLTE, including the new Voigt-profile algorithm; and (3) improvements ^{we} made in the AFGL Atmospheric Auroral Radiance Code (AARC).</p>					
20. DISTRIBUTION/AVAILABILITY OF ABSTRACT UNCLASSIFIED/UNLIMITED <input type="checkbox"/> SAME AS RPT. <input type="checkbox"/> DTIC USERS <input type="checkbox"/>			21. ABSTRACT SECURITY CLASSIFICATION Unclassified		
22a. NAME OF RESPONSIBLE INDIVIDUAL Arthur Corman			22b. TELEPHONE NUMBER (Include Area Code)		22c. OFFICE SYMBOL AFGL/LSI

TABLE OF CONTENTS

<u>Section</u>	<u>Page</u>
PREFACE	
I. INTRODUCTION	1
II. METHODS AND RESULTS OF THE CO ₂ 2.7 μ m MODELLING EFFORT	3
1. Introduction	3
2. General Approach to Calculation of Vibrational-Level Populations	4
3. Solar Pumping Calculations	13
4. Vibrational Populations and Excitation Rates	20
5. Radiance Calculations	34
6. Modifications to the Basic Model	39
7. Comparison with Experimental Results	45
8. Discussion	48
9. Conclusion	50
10. References	52
III. IMPROVEMENTS IN THE NLTE ALGORITHM	53
1. Introduction	53
2. Program Organization	53
3. Voigt Profile Algorithms	57
3.1 Lineshape Considerations	57
3.2 Basic Representation	58
3.3 Rybicki's Algorithm	59
3.4 Pierluissi's Algorithm	59
3.5 Tests for Accuracy and Speed	61
3.6 Function ZVGT	69
4. Numerical Integration Algorithm	72
4.1 General Description	72
4.2 Integration Rule	73
4.3 Adjustments for Different Lines	75
4.4 Truncation Procedure	77
4.5 References	79



Accession For		
NTIS	CRA&I	<input checked="" type="checkbox"/>
DTIC	TAB	<input type="checkbox"/>
Unannounced		<input type="checkbox"/>
Justification		
By		
Distribution /		
Availability Codes		
Dist	Avail and/or Special	
A-1		

TABLE OF CONTENTS (Continued)

<u>Section</u>	<u>Page</u>
IV. ATMOSPHERIC AURORAL RADIANCE CODE	81
1. Introduction	81
2. Calculation of Electron-Ion Pair Production Profile	82
3. Calculation of Volume Emission Rate	85
4. Calculation of Radiance at the Observation Point	87
5. Generation of Synthetic Spectrum	89
6. References	89
V. APPENDIX	90

PREFACE

The analysis, computer programs, and results discussed herein are the result of analytical research performed for:

Air Force Geophysics Laboratory
Hanscom Air Force Base, Massachusetts 01731

I. INTRODUCTION

A large portion of the work performed in 1984 under the provisions of contract F19628-84-C-0071 consisted of developing a model for infrared emission from CO_2 molecules in the upper atmosphere. This effort included the development and refinement of computer codes having the purpose of 1) calculating the rate coefficients for absorption of solar flux in the upper atmosphere; 2) calculating the steady-state populations of vibrational levels of CO_2 as a function of altitude for specified conditions by equating the excitation and de-excitation rates of all important collisional and radiative processes; and 3) predicting the radiance to be observed by hypothetical sensors in limb- and zenith-look geometry. These codes have been applied to a special problem, namely determining the limb radiance in the 2.5-2.9 μm wavelength region due to emission in the 101 combination bands of CO_2 during daylight hours. In our first three quarterly reports we have outlined the principal physical results of this study; in Section II of this final report we present a more detailed version of our methods and conclusions.

The absorption and radiance codes, although applied to the CO_2 radiance problem, were developed for use with other absorber and emitter molecules as well; in fact, they are quite general line-by-line codes.

During the last quarter we improved the NLTE algorithm, which is the basic radiance calculation, by making it more efficient. It is now fast enough, for all CO_2 bands, to run in iterative applications where it may be invoked many times in a single job. Some of these improvements are discussed in Section III.

The other major emphasis of the fourth quarter was on the A.F.G.L. Auroral Model. The codes comprising this model, known collectively as the Auroral Atmospheric Radiance Code (AARC), were extensively revised and made compatible with each other so that they could be used in a single interactive application. In Section IV we describe the calculations performed by each component of AARC and the modifications which were made.

The other tasks carried out during the life of this contract were described in the first two quarterly reports. Notable among these is program NLTEA for auroral radiance, which will be incorporated into AARC. This task was summarized in the second quarterly.

II. METHODS AND RESULTS OF THE CO₂ 2.7 μ M MODELLING EFFORT

1. INTRODUCTION

In order to learn more about emission in the infrared from non-LTE regions of the atmosphere, and in order to provide a vehicle for developing a comprehensive line-by-line model for CO₂, we have carried out a detailed set of calculations of CO₂ limb radiance in the 2.7 μ m wavelength region for daylit atmospheres. Under the assumed conditions, which simulate those of the daylit scans of the SPIRE experiment <1-3>, the principal physical processes involved are the absorption of solar flux by high-lying ro-vibrational states of CO₂ molecules at wavelengths of 2.7 μ m or less; the collisional redistribution of populations among the high-lying vibrational levels; spontaneous emission in the 101 combination bands and in other bands; and exchange of vibrational quanta with N₂. In this section we describe calculations which, taken together, constitute a model for infrared emission from CO₂ at 2.7 μ m. We also discuss some of the implications of our results and also of the comparison we make with the experimental results. We do not discuss the codes in detail, but we note that considerable attention has been paid to making them general, flexible, and efficient so that they may be applied to situations other than those which are discussed below.

An earlier study <4> has found that the daytime emission detected by the SPIRE sensor near 2.7 μ m contains, primarily, contributions from the ν_1 and ν_3 fundamentals of water vapor and the 101 combination bands of CO₂. In the latter case it was also established that solar pumping of the 201 and 301 levels followed by fluorescence to 100 and 200, respectively, gives a more significant component of the CO₂ emission than the resonant 101--000 transitions. The significance of the 201-100 transitions, and other conclusions of the earlier work, are confirmed in the present effort. Additional contributions from other bands are evaluated as well. Several collisional excitation and quenching mechanisms which were not previously considered have been included here, and their effect is assessed. The inclusion of these collisional mechanisms decreases the observed emission by only about 30%. However it markedly changes

the spectral distribution of the observed radiance. We also compare our predictions with the SPIRE dataset. This comparison, made in conjunction with certain trial modifications of our basic model, allows us to put limits on the values of some of the poorly-known collisional rate constants entering our calculations.

2. GENERAL APPROACH TO CALCULATION OF VIBRATIONAL-LEVEL POPULATIONS

Before the $2.7\mu\text{m}$ emission from CO_2 can be computed, the steady-state populations of all the radiating levels must be calculated. Figure 1 is an energy level diagram for the principal (626) isotope showing the vibrational states which are necessary for this calculation. The $2.7\mu\text{m}$ transitions, including solar pumping from the ground state, are indicated by the solid lines. The important solar pumping at 2.0 and $1.6\mu\text{m}$ is also indicated. Four groups of high-lying levels, including all the levels radiating at $2.7\mu\text{m}$, are identified. Within each group the vibrational levels are strongly coupled by collisional interactions. The principal radiating levels are $1001x$ ($x=1,2$) in Group 1; $1111x$ ($x=1,2$) in Group 2; $2001y$ ($y=1,2,3$) in Group 3; and $3001z$ ($z=1,2,3,4$) in Group 4. The notation for the vibrational levels is standard AFGL notation $\langle 5 \rangle$, as is the isotopic designation.

Table 1 lists the 26 bands in the $2.7\mu\text{m}$ region whose contribution to the total radiance has been calculated in this modelling effort. These bands are divided into eight sets, A through G, to facilitate our discussion.

The only mechanisms which couple states within any single group are collisional interactions which cause small changes in the internal energy of the CO_2 molecule and reorient the vibrational motion. These result from collisions with air molecules, whose internal energy states remain unchanged.

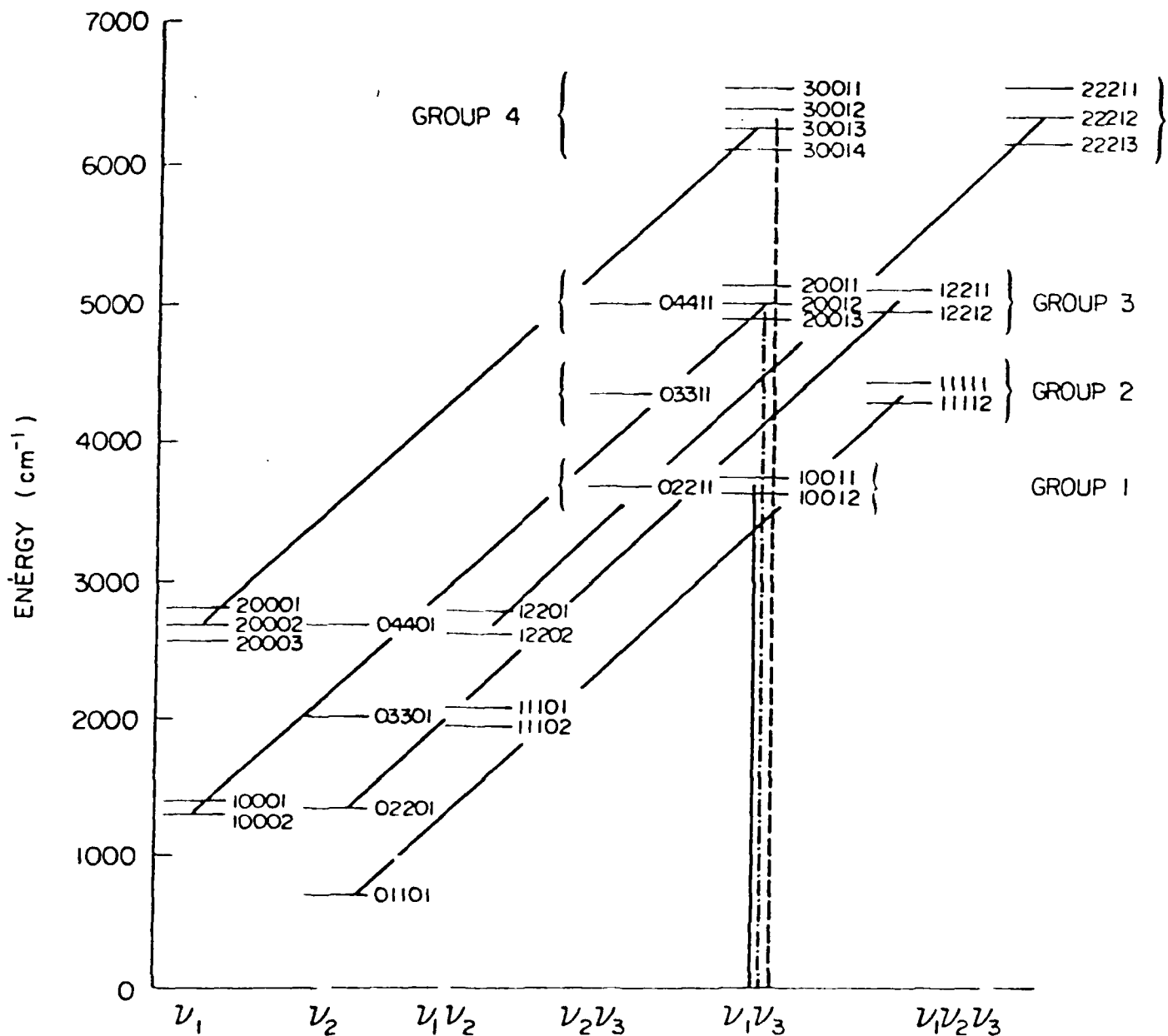


Figure 1. CO₂ energy levels relevant for the 2.7 μ m radiance calculations, including the four groups of high-lying states discussed in the text. Solid lines show 2.7 μ m radiative transitions. Vertical lines show the principal solar pumping channels. For Group 2, the 2.7 μ m resonance bands are the major channels. Channels for quenching by V-V interactions with N₂ are not shown.

Set	Band	Isotope	Vib. Transition		A (sec ⁻¹)
			(cm ⁻¹)	(μm)	
A	10012-00001	626	3612.8	2.77	11.0
	10011-00001	626	3714.8	2.69	16.9
B	20013-10002	626	3568.2	2.80	18.1
	20012-10002	626	3692.4	2.71	24.4
	20012-10001	626	3589.7	2.79	16.0
	20011-10001	626	3711.5	2.69	33.5
C	11112-01101	626	3580.3	2.79	10.8
	11111-01101	626	3723.2	2.69	16.5
D	12212-02201	626	3552.9	2.81	10.6
	12211-02201	626	3726.7	2.68	18.1
E	30014-20003	626	3527.6	2.83	25.2
	30013-20003	626	3679.6	2.72	26.1
	30013-20002	626	3556.8	2.81	28.3
	30012-20002	626	3676.7	2.72	43.9
	30012-20001	626	3550.7	2.82	16.1
	30011-20001	626	3705.9	2.70	49.6
F	22213-12202	626	3518.7	2.84	20.0
	22212-12202	626	3703.5	2.70	24.1
	22212-12201	626	3527.8	2.83	12.8
	22211-12201	626	3713.8	2.69	41.4
G	10012-00001	636	3527.7	2.83	8.7
	10011-00001	636	3632.9	2.75	15.7
	10012-00001	628	3571.1	2.80	13.5
	10011-00001	628	3675.1	2.72	13.1
	10012-00001	627	3590.9	2.78	12.1
	10011-00001	627	3693.6	2.71	15.6

Table #1 CO₂ vibrational bands whose contributions to the total radiance observed near 2.7 μm have been calculated in this study. Bands are grouped into sets A through G to facilitate the discussion.

The individual states within each group are also coupled to other (lower lying) CO_2 states by the absorption and emission of radiation, mostly at $2.7\mu\text{m}$ and $4.3\mu\text{m}$, and by exchange of vibrational quanta with N_2 molecules <6-8>. The latter process, the net effect of which is usually to quench CO_2 $2.7\mu\text{m}$ emission, involves a change of ± 1 in the ν_3 quantum number. In general, then, radiative transitions near $4.3\mu\text{m}$ are in parallel with collision-induced V-V transitions coupling the same vibrational levels. The populations of the lower-lying states, which are needed to calculate excitation rates, are taken to be static. This is a reasonable approximation, as these levels are more strongly coupled to each other than to the higher lying levels in which we are primarily interested. The static populations that we used were obtained through the courtesy of T. Degges of Visidyne Corp. from a simulation of the conditions of the SPIRE experiment using the A.F.G.L. High-Altitude Infrared Radiance Model (IRR)<9>. We shall see that the lower-lying excited states are important for our calculations only at altitudes below 60 km. In this altitude range our static populations are practically the same as LTE populations.

The four groups of states are treated as independent of each other. This is a good approximation because the possible transitions between states in different groups are very much weaker than other transitions involving them. That is, because of larger energy differences, collisional transfer rates are lower between groups than within groups. The most important radiative transitions between groups, ν_2 transitions, turn out to be a minor perturbation in the overall picture.

In order to calculate the steady-state populations of vibrational levels within a group, one simply equates the sum of excitation rates for each level due to all important mechanisms with the sum of de-excitation rates for that

Reaction	Forward Rate Constant
1. $\text{CO}_2(10011) + \text{M} \rightleftharpoons \text{CO}_2(10012) + \text{M}$	$k_{13} = 3 \times 10^{-11}$
2. $\text{CO}_2(02211) + \text{M} \rightleftharpoons \text{CO}_2(10012) + \text{M}$	$k_{12} = 1.5 \times 10^{-13}$
3. $\text{CO}_2(10011) + \text{M} \rightleftharpoons \text{CO}_2(02211) + \text{M}$	$k_{23} = 2k_{12}$
4. $\text{CO}_2(10012) + \text{N}_2(0) \rightleftharpoons \text{CO}_2(10002) + \text{N}_2(1)$	$k_v = 5 \times 10^{-13} \left(\frac{300}{T} \right)^{\frac{1}{2}}$
5. $\text{CO}_2(02211) + \text{N}_2(0) \rightleftharpoons \text{CO}_2(02201) + \text{N}_2(1)$	
6. $\text{CO}_2(10011) + \text{N}_2(0) \rightleftharpoons \text{CO}_2(10001) + \text{N}_2(1)$	

Table #2 Reactions resulting in non-radiative transitions involving the three states of Group 1. The forward rate constants are also listed.

level. We illustrate this by considering the 10012 state alone, and then a group of states (10012, 02211, 10011) which were treated simultaneously.

In the simplest view, 10012 is populated by solar pumping from the ground state, quenched by collisions with ground-state nitrogen and additionally depleted by spontaneous radiation in the $4.3\mu\text{m}$ and $2.7\mu\text{m}$ bands. If we allow the subscript "1" to stand for 10012, and "G" for the ground state denoted by 00001, the rates for these three processes are $J_{1G}n_T$, $k_v[N_2(0)]n_1$, and A_1n_1 , respectively. The solution for the desired number density n_1 is found by equating the first rate with the sum of the second and third.

In these expressions, J_{1G} is the number of photons/sec absorbed in the band 00001-10012 per molecule of CO_2 , n_T is the total number density of CO_2 , A_1 is the total Einstein coefficient for 10012, k_v is the rate constant for quenching by nitrogen, and $[N_2(0)]$ is the ground-state population of nitrogen. All these quantities are presumed known. A_1 has a value of about 455 photons/molecule-sec, with a branching ratio of about 40:1 in favor of the $4.3\mu\text{m}$ transition. One can see, then, that of all the solar energy pumped into the 10012 level, very little re-emerges as radiation at $2.77\mu\text{m}$ even at altitudes where collisional quenching is negligible. This is the principal justification for neglecting the pumping due to $2.7\mu\text{m}$ emission from CO_2 molecules in the atmosphere.

This simple picture is complicated only very slightly by the recognition that, with a sufficiently large population in the low-lying 10002 level (which is symbolized by the subscript A), excitation of 10012 may occur because of collisions with excited-state nitrogen $[N_2(1)]$ and also because of solar pumping the $4.3\mu\text{m}$ band. That is, another solar pumping coefficient J_{1A} must be determined, and additional excitation rates $J_{1A}n_T$ and $k'_v[N_2(1)]n_A$ must be included in the equation.

Because of the expected strong collisional coupling of the 10012 level with the 02211 and 10011 levels, this simple picture is inadequate to determine the population of 10012. One must identify the important collisional

interactions (see Table 2), put in collisional rate constants, and solve simultaneous equations for the populations of all three levels. Before writing these equations, it is desirable to comment on the effect of doing this.

First of all, the discussion, above, of the 10012 level also applies to 10011 to the extent that one can ignore collisional coupling. The 02211 level, however, is different because its radiative transitions to and from the ground level, and to and from 01101, are forbidden. As a result, what population there is comes from absorption of solar photons around $4.3\mu\text{m}$ by the thermally populated state (02201) at 1335 cm^{-1} . The pumping is therefore much weaker than that for the other two levels. The mechanisms for quenching emission at $2.7\mu\text{m}$, on the other hand, consist of V-V interactions with nitrogen molecules and radiation at $4.3\mu\text{m}$, and are comparable in strength to those of the other two levels. The result, then, of coupling 02211 to 10012 and 10011 is to provide a pathway whose net effect is to deplete the populations of the latter two states. (At least, this is true for altitudes at which a sufficient number of collisions occur to couple these states effectively.)

The second notable effect of coupling the levels within this group is to deplete the higher-lying levels (e.g., 10011) in favor of the lower-lying ones. This causes a larger fraction of the emitted radiation to appear at $2.77\mu\text{m}$ ---and a smaller fraction at $2.69\mu\text{m}$ ---than would otherwise be the case, and thus affects the distribution of radiation in the wavelength region under consideration. In general, the levels split by Fermi-resonance---levels differing only in the fifth index---are probably coupled to each other much more strongly than to the other nearby levels such as 02211, which have a different symmetry. (We call these other levels "side levels" for want of a better term.) They are therefore likely to be in equilibrium with each other at quite high altitudes, considerably higher than the altitudes at which they are effectively decoupled from the "side levels".

The equations which need to be solved for the number densities of the three states are written in matrix form, below. The matrix elements are

coefficients derived from the rate constants describing the collisional interactions, V-V interactions with N_2 , and from the radiative transition probabilities. The subscripts (1,2,3) refer to (10012, 02211, 10011), respectively, and the subscripts (G,A,B,C) refer to (00001, 10002, 02201, 10001). J_i is the sum of all solar pumping rates for level i ($i = 1, 2$, or 3). A_i is the sum of the Einstein coefficients for level i , and the K_{ij} are the rate coefficients for reactions coupling states i and j , including those for which i and j are within the same group and those for which i or j represents a lower-lying state. The diagonal elements of the matrix are the de-excitation rate coefficients and all the other terms, including the inhomogeneous ones, represent excitation mechanisms. The result is

$$\begin{pmatrix} A_1 + K_{A1} + K_{21} + K_{31} & -K_{12} & -K_{13} \\ -K_{21} & A_2 + K_{B2} + K_{12} + K_{32} & -K_{23} \\ -K_{31} & -K_{32} & A_3 + K_{C3} + K_{13} + K_{23} \end{pmatrix} \begin{pmatrix} n_1 \\ n_2 \\ n_3 \end{pmatrix} = \begin{pmatrix} J_1 n_T + K_{1A} n_A \\ J_2 n_T + K_{2B} n_B \\ J_3 n_T + K_{3C} n_C \end{pmatrix} \quad (1)$$

The rate coefficients for quenching (e.g., K_{A1}) and excitation (e.g., K_{1A}) due to exchange of quanta with nitrogen are given by

$$K_{A1} = k_v [N_2(0)] \quad (2a)$$

$$K_{1A} = k'_v [N_2(1)] \quad (2b)$$

where k_v is listed in Table 2. The reverse rate constant is

$$k'_v = k_v \exp[-C_2(E_1 - E_A - 2330)/T] \quad (3)$$

where $C_2 = 1.4388$ is the second radiation constant and T is the kinetic temperature.

The rate coefficients for intramolecular exchange of quanta are

$$K_{13} = k_{13}[M] \quad K_{31} = k'_{13}[M] \quad (4a)$$

$$K_{12} = k_{12}[M] \quad K_{21} = k'_{12}[M] \quad (4b)$$

$$K_{23} = k_{23}[M] \quad K_{32} = k'_{23}[M] \quad (4c)$$

	Upper State	Lower State	00001	01101	10002	02201	10001	11102	03301	11101	20003	12202	20002	04401	12201	20001
GROUP 1	10012		J		J,V											
	02211				J,V											
	10011		J		J,V											
GROUP 2	11112			J				J,V								
	03311							J,V								
	11111			J				J,V								
GROUP 3	20013		J		J						J,V					
	12212		J		J						J,V					
	20012		J		J		J				J,V					
	04411										J,V					
	12211		J		J						J,V					
	20011		J				J				J,V					
GROUP 4	30014		J													
	22213										J					
	30013		J													
	22212										J				J	
	30012		J													
	22211														J	
	30011		J													

TABLE 3. Excitation mechanisms considered in the calculation of the populations of the vibrational levels. "J" stands for solar pumping and "V" stands for excitation by exchange of vibrational quanta with N₂. The important de-excitation mechanisms are just the processes which are complementary to these, except that the seven levels in Group 4 are also quenched by N₂ collisions and spontaneous emission at 2.7 μ m and 4.3 μ m. Collisional interactions within each group are not listed.

where $[M]$ is the number density of air molecules and the forward rate constants are given in Table 2. Since we have written the forward rate constants with two subscripts, with the first identifying the lower state and the second the upper state, the reverse rate constants are given by

$$k'_{ij} = k_{ij} \frac{g_i}{g_j} \exp[-C_2(E_j - E_i)/T] \quad (5)$$

where the g 's are the statistical weights and the E 's are the vibrational energies in wavenumbers.

The three other groups of states are treated in ways which are analogous to that described above. Table 3 lists the mechanisms by which the various levels in each group are coupled to lower-lying levels. In addition, each level in each group is coupled to all the other levels in its own group. In both cases, collisional processes are represented by rate constants which are identical or analogous to those in Table 2 and rate coefficients like those in Eqs. (2) and (4). The precise energy levels can be found in Reference 11, as can the band strengths which were used to calculate the Einstein coefficients for all possible spontaneous transitions.

In the next two sections we give some of the results of the solar-pumping and vibrational-population calculations, and indicate the relative importance of some of the factors we have considered.

3. SOLAR PUMPING CALCULATIONS

A line-by-line code, SABS, which uses data collected in the A.F.G.L. Atmospheric Absorption Line Parameters Compilation <5, 12> computes the absorption of solar flux as a function of altitude. We used a standard solar-flux profile <13> and a solar elevation angle of 12° , which closely corresponds to the conditions of the first daylight scan of the SPIRE experiment. Given the temperature and total CO_2 profiles, the program calculates the transmission through and absorption within shells one kilometer thick starting

at the top of the atmosphere and proceeding downward to an altitude of 40 km. The program assumes all atmospheric parameters to be constant within each shell, uses a rotational temperature equal to the kinetic temperature, and represents the shape of each absorption cross-section with a Voigt function. The absorption profiles at each altitude are then found at a sufficient number of points within each line to enable integration over frequency. Summing the integrated absorption over lines gives the number of transitions per second per molecule of CO_2 between the lower vibrational state, i , and the upper state, j ---that is, the coefficient J_{ji} .

Figures 2-5 give this absorption as a function of altitude for those transitions of the major isotope which populate states in the four groups under consideration. Some of the curves represent negligible contributions to the total solar excitation of their respective upper states over most or all of the altitude range and are included only for completeness. Curves for the 636 isotope are also included in Figure 2.

Figures 2, 4, and 5 demonstrate that greatest absorption usually occurs in bands originating in the ground state, while the hot bands make smaller contributions. However, it is important to note that hot bands do not always give negligible contributions. They also illustrate the point that the shape of the curves for the hot bands reflects the assumed lower-state population more than anything else. In Figure 4, for example, the curves representing absorption from the 1000x levels have maxima and minima at the same altitudes as the corresponding vibrational-temperature profiles, and mimic them in other ways as well. (We reiterate that in the low-altitude regions where these bands are important, the vibrational temperatures nearly equal the kinetic temperature.) These generalizations are of course only valid where the incident solar radiation has not been bleached out at higher altitudes.

The absorption which occurs along the paths used to calculate these curves ranges from negligible ("thin" lines) to severe ("thick" lines) to extreme. A convenient figure of merit, τ_c , is the optical depth (at a given altitude) at the center of the strongest line of a band, from which one can crudely estimate the attenuation by comparing its value with unity.

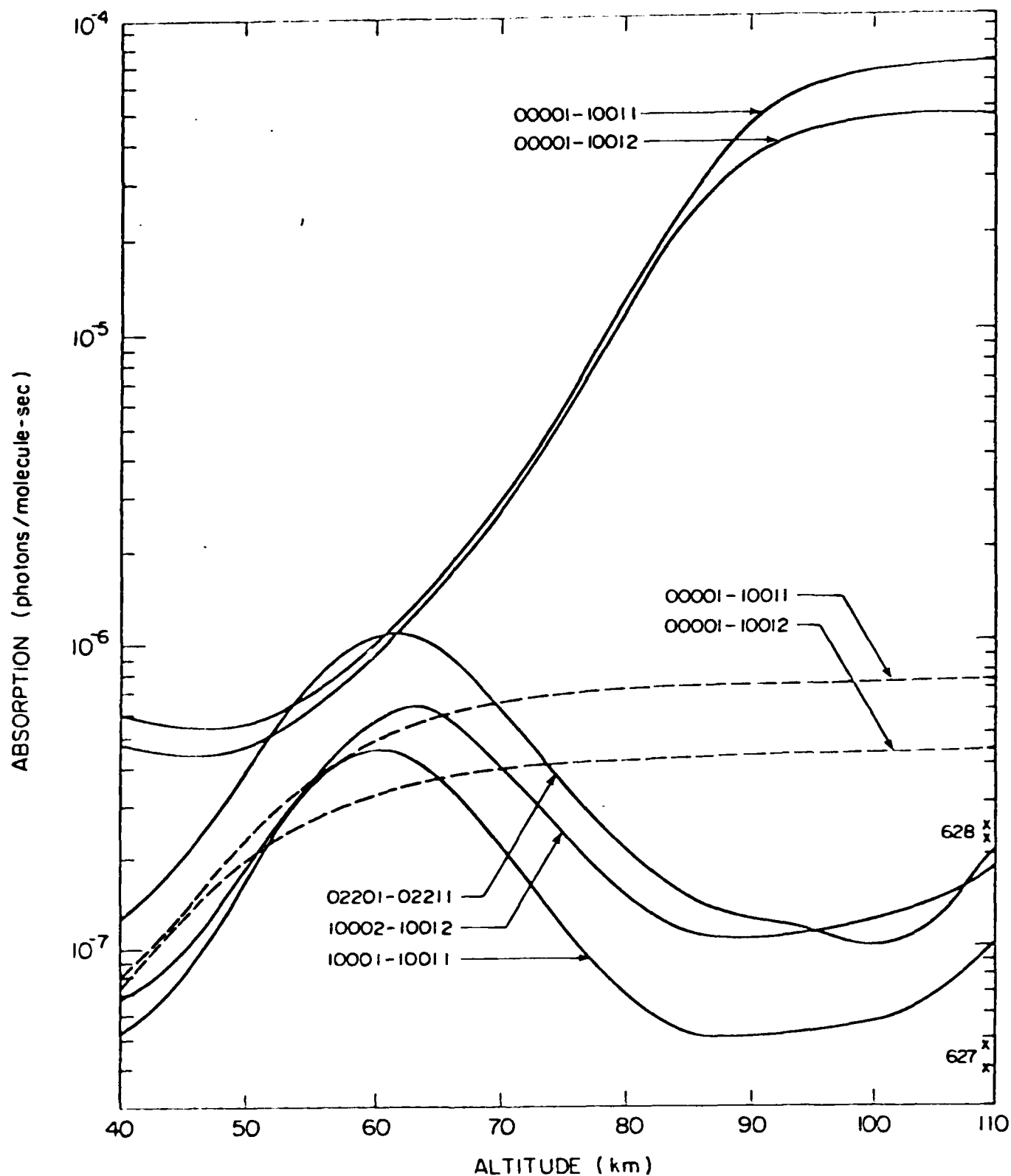


Figure 2. Solar flux absorption coefficients for bands populating the states in Group 1, as a function of altitude. Solid lines refer to bands of the 626 isotope, dashed lines to those of the 636 isotopes. Xs mark high-altitude limits for absorption in the $2.7\mu\text{m}$ bands of the 627 and 628 isotopes. Hot-band curves are sensitive to the static population assumed for the lower states, but these are nearly LTE for altitudes at which important contributions result.

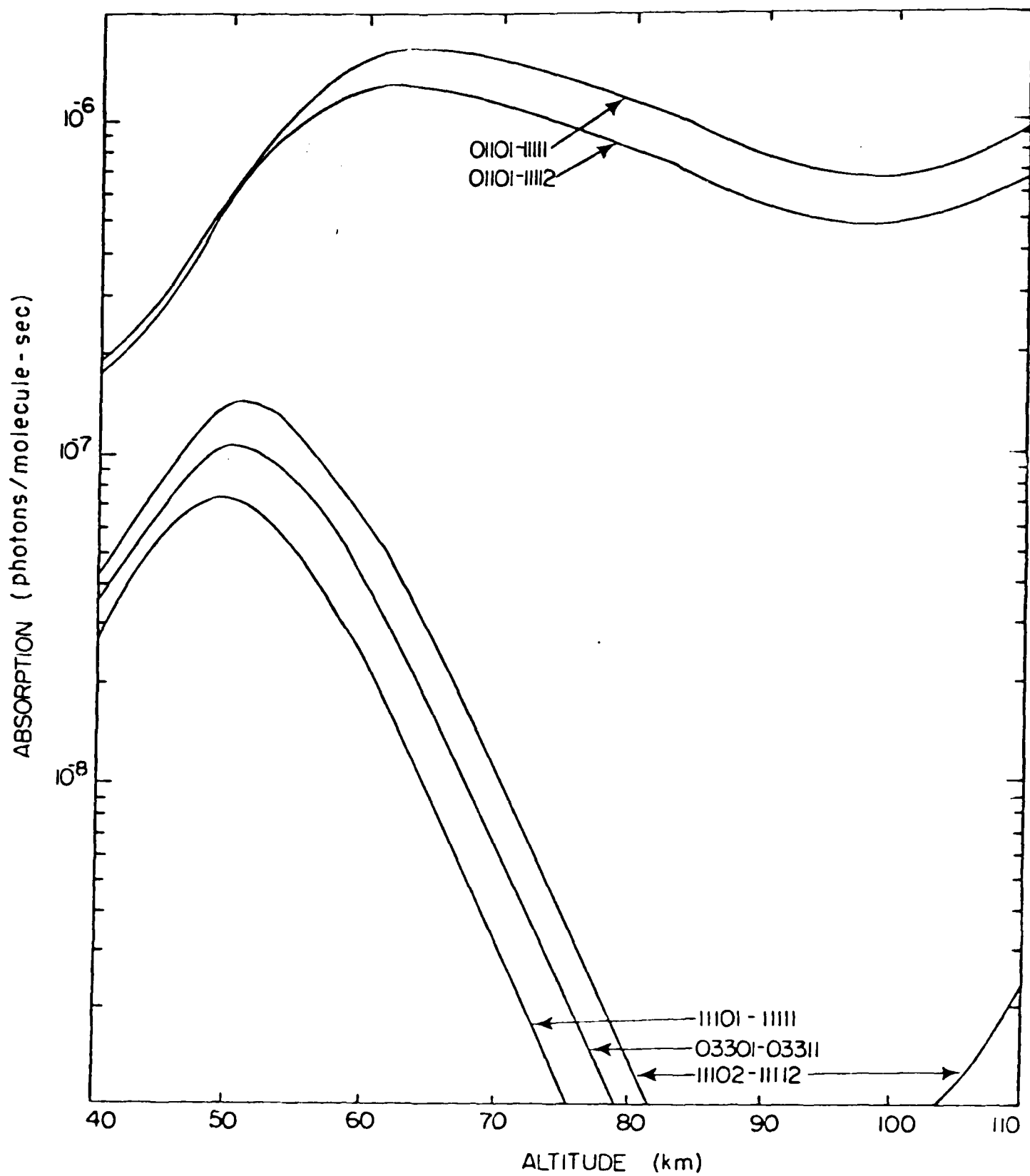


Figure 3. Solar flux absorption coefficients for bands populating the states in Group 2, as a function of altitude for the 626 isotope.

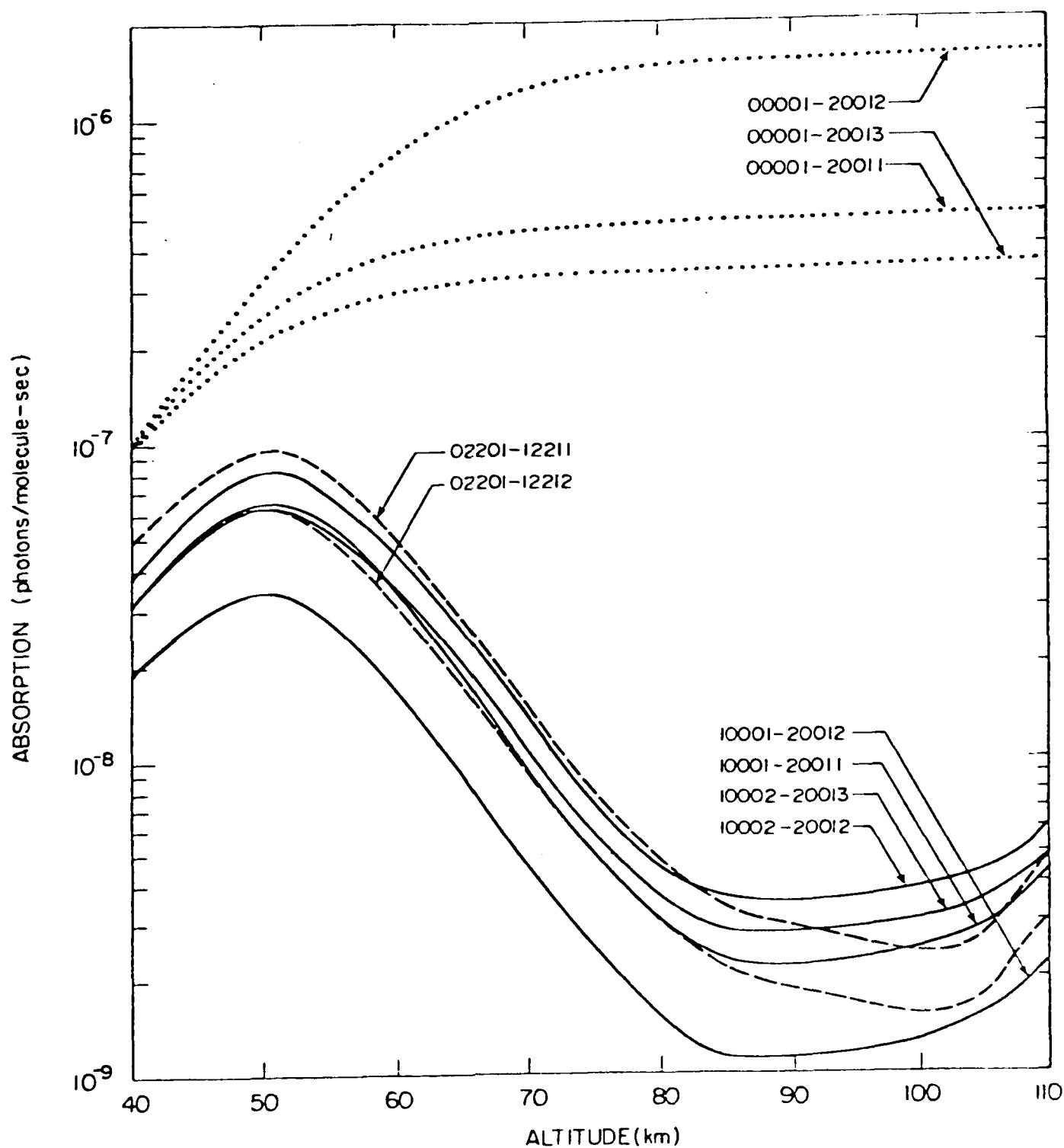


Figure 4. Solar flux absorption coefficients for bands populating the states in Group 3, as a function of altitude. All curves refer to the 626 isotope.

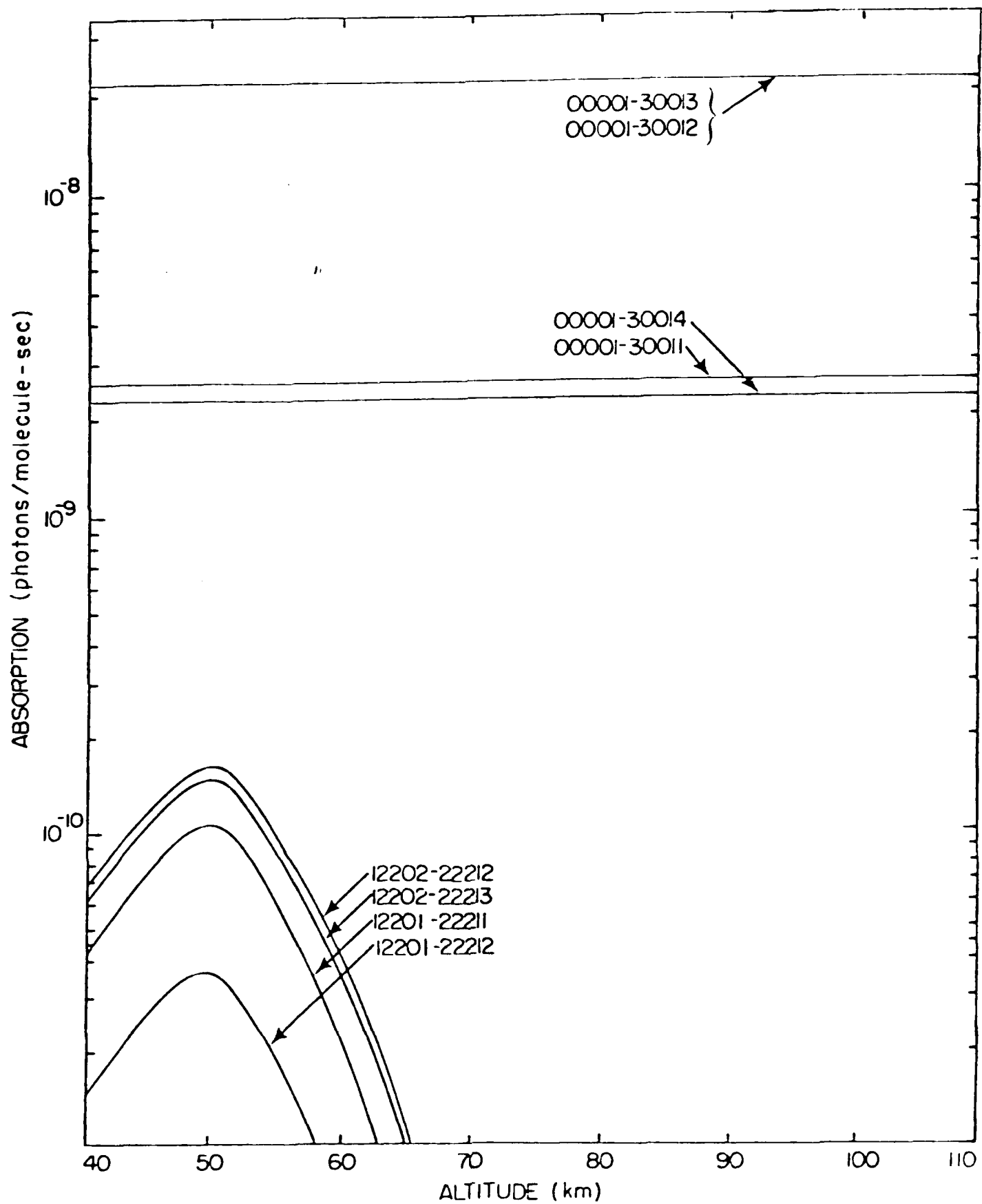


Figure 5. Solar flux absorption coefficients for bands populating states in Group -, as a function of altitude. All curves refer to the 626 isotope.

The two uppermost curves in Figure 2, giving the transitions up from ground to the 1001x levels, exhibit the full range of possibilities. At the highest altitudes the curves are nearly flat because the CO_2 density is too low to significantly deplete the incident radiation. Between 100 and 55 km the solar excitation drops by two orders of magnitude because of the severe absorption taking place in this region. The optical depth parameter, τ_c , at these two altitudes is approximately .1 and 200, respectively. The extreme case is illustrated by the upturn near 50 km. This occurs because of absorption in the wings of the Voigt lines, which become more prominent because of collision-broadening. At these altitudes the flux at the line-centers is completely absorbed out but because of the small collision width at greater altitudes, that in the wings is not diminished at all. Thus, the increasing breadth of the absorption lineshape is responsible for the increase in absorption, which now occurs far from the line centers. This behavior of course does not occur when a Doppler lineshape is used to describe the cross-sections; rather, the monotonic decrease with decreasing altitude is maintained below 60 km for all reasonable temperature profiles.

For the other bands originating in the ground state (c.f., Figures 2, 4, and 5) the onset of severe attenuation occurs at lower altitudes, reflecting weaker transitions, or, in the case of minor isotopes, smaller ground-state populations. In Figure 2 the absorption curves for the 636 isotope, which comprises about 1.1% of the total CO_2 , are flat down to about 70 km, where the lines begin to become thick. Curves for the 628 and 627 isotopes are similar, with comparable attenuation at about 60 and 47 km, respectively. In all these cases, 10% attenuation corresponds to values of about .12 for τ_c . The high-altitude limits of the 626 and 636 curves are in practically the same ratio as the isotopic abundances; for the nonsymmetrical isotopes this is also nearly true despite the presence of twice as many lines in each band.

The differences between the 10012 and 10011 curves (Figure 2) and, more notably, between the 20012 curve (top, Figure 4) and the others in the 00001-2001y family, occur because of different transition strengths. Attenuation

of solar photons has the effect of equalizing the pumping rates at lower altitudes, but at higher altitudes these differences strongly affect the vibrational level populations and thus the distribution of radiation in the $2.7\mu\text{m}$ window.

As mentioned earlier, the absorption in the hot bands is most strongly determined by the populations of the lower states. In the absence of attenuation, the absorption curves have the same altitude-dependence as the vibrational-temperature profiles used to calculate these populations. These profiles all have maxima at about 49 km and most of the hot-band curves in Figures 2-5 also peak at this altitude. Exceptions occur for the bands whose upper states are in Group 1 (Figure 2) and Group 2 (Figure 3), where the maximum absorption lies above 60 km because of the attenuation of incident flux. The optical depth parameter, τ_c , at 49 km is approximately 12, 12, and 5 for these three cases, indicating that absorption is significant across much of the bands. In fact, the sharp dropoff in absorption between 60 and 40 km occurs more because of the attenuation in the solar flux than because of the decreasing population of available absorbers.

The effect of changing the solar elevation angle, and hence the distance traversed through the atmosphere by sunlight, is important only when attenuation of incident flux is significant. The four daylight scans of SPIRE actually correspond to angles between 12° and 6° . Within this range the traversal distance ($\sim \sec \theta$) varies by a factor of two. Thus, although the high-altitude limits are the same for all angles, the absorption occurring at altitudes below which attenuation of incident flux is significant is reduced (by comparison to the curves given) as the elevation angle decreases. This is particularly important for the 00001-1001x bands below 100 km, and for the 00001-2001y bands (Figure 4) below 75 km.

4. VIBRATIONAL POPULATIONS AND EXCITATION RATES

Given the solar-pumping results discussed in the previous section, it was a straightforward matter to set up and solve the equations--(e.g., Eq. (1)--

for the populations of the levels in the four chosen groups. We present the results as the ratio of the population in each vibrational level to ground-state CO_2 because this permits the easiest graphical visualization of the effect of subtle but important changes. We also present curves giving, for the most important vibrational levels, the excitation and de-excitation rates (in units of transitions/sec-cm³) as a function of altitude. In particular, we break out the separate effects of radiative excitation and de-excitation, and also the net effects of the N_2 vibrational-quantum exchange, the collisional interactions connecting the Fermi-resonance-split states, and the collisional interactions connecting the principal radiating levels with the side levels.

We have already discussed, qualitatively, the excitation and de-excitation mechanisms responsible for the populations of states in Group 1. In Figure 6 we give the population ratios, and in Figures 7 and 8 the rates for 10012 and 10011, respectively. As expected, solar pumping is dominant for populating these two levels. Over a narrow range of altitudes near 50 km the net effect of N_2 V-V interactions is to excite these states. In fact the prominent peaks at 50 km in Figure 6 result from a combination of this excitation by N_2 and the solar pumping in the wings of the Voigt lines which was discussed in the previous section. Between 54 and 80 km, however, N_2 V-V interactions constitute a strong quenching mechanism which is largely responsible for limiting the radiation at 2.7 μm and 4.3 μm . Only above 75 km does the spontaneous emission become the most important mechanism for depopulating these levels.

The effect on the two 1001x levels of including the collisional interactions with the side level 02211 is, as mentioned earlier, to deplete both. The depletion rate can be seen from Figures 7 and 8 to be modest but not negligible. Coupling the Fermi-resonance-split levels, on the other hand, is important even up to 100 km, where its net effect is 30% of the solar pumping rate.

The three levels comprising Group 2---11111, 03311, 11112---differ from those of Group 1 in that all the radiative transitions to ground are very

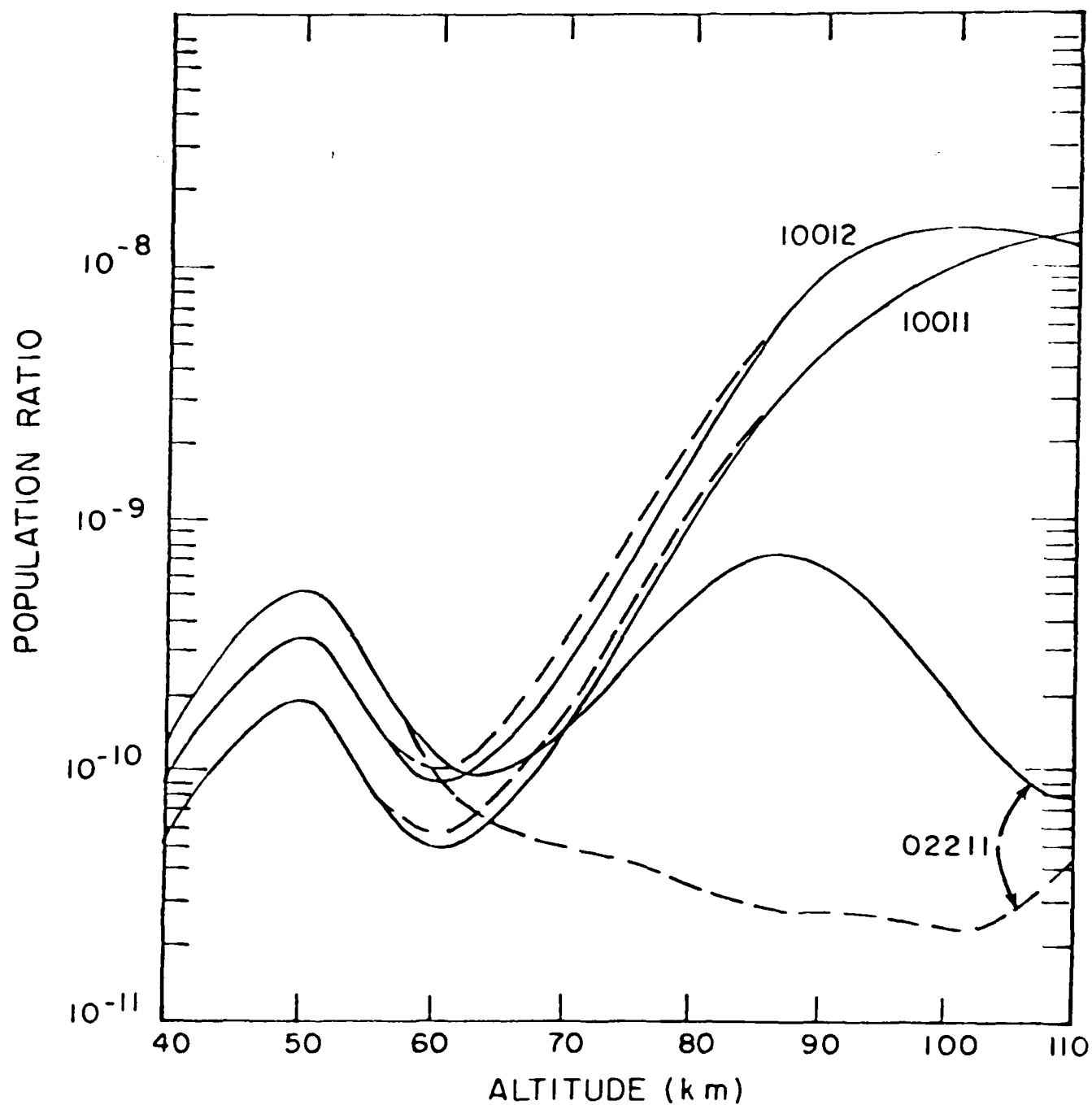


Figure 6. Ratios of the populations of the three vibrational levels in Group 1 to that of the ground state for the 626 isotope. Solid lines give results from the basic model and dashed lines give results from MOD1 (see text, section 6).

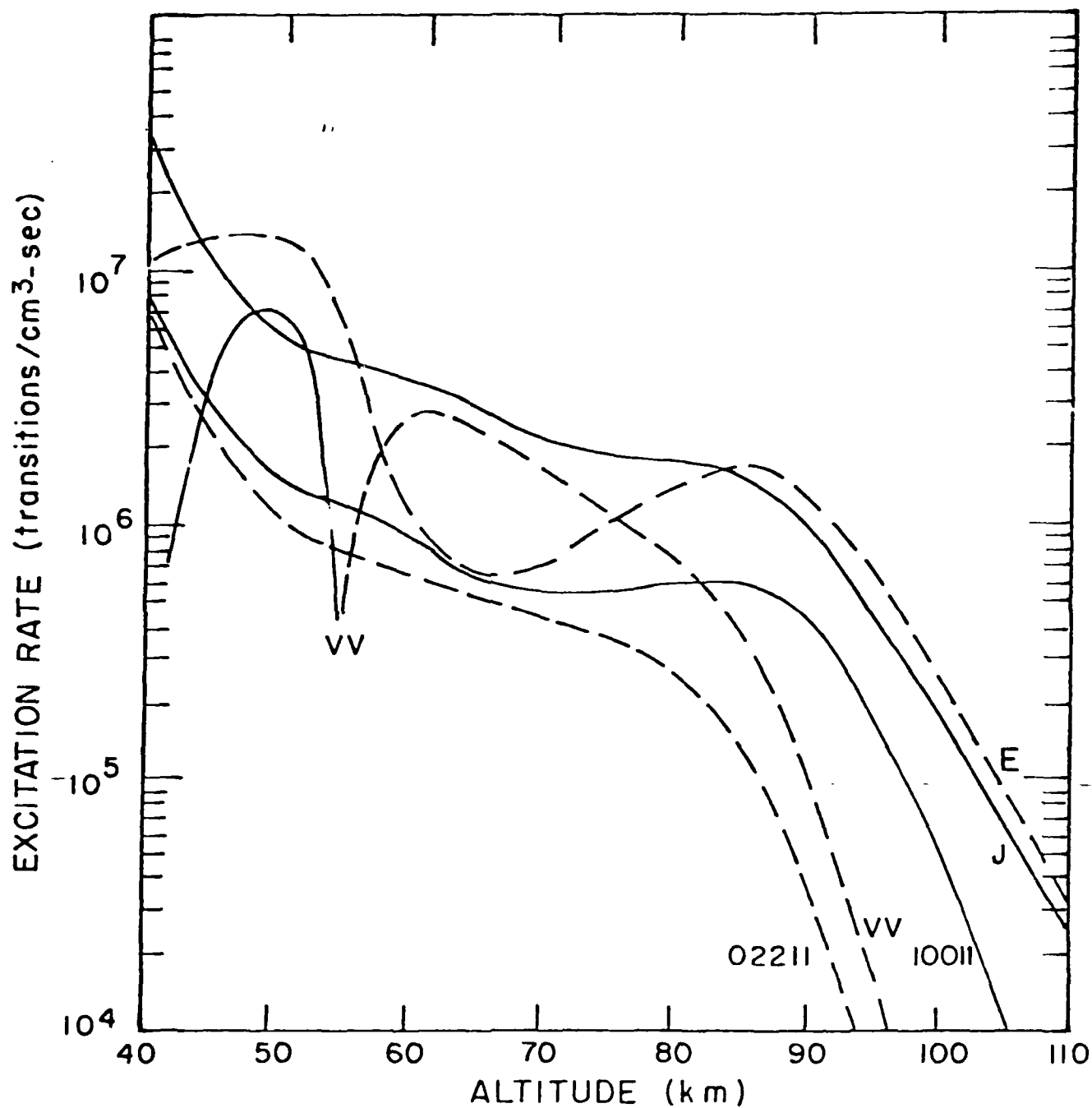


Figure 7. Excitation rates (solid lines) and de-excitation rates (dashed lines) due to mechanisms coupling the 10012 level with other levels. "J" represents solar pumping from lower states (primarily ground), "E" represents total spontaneous emission, "VV" represents N_2 collisions, and "10011" and "02211" represent collisional interactions with those two levels.

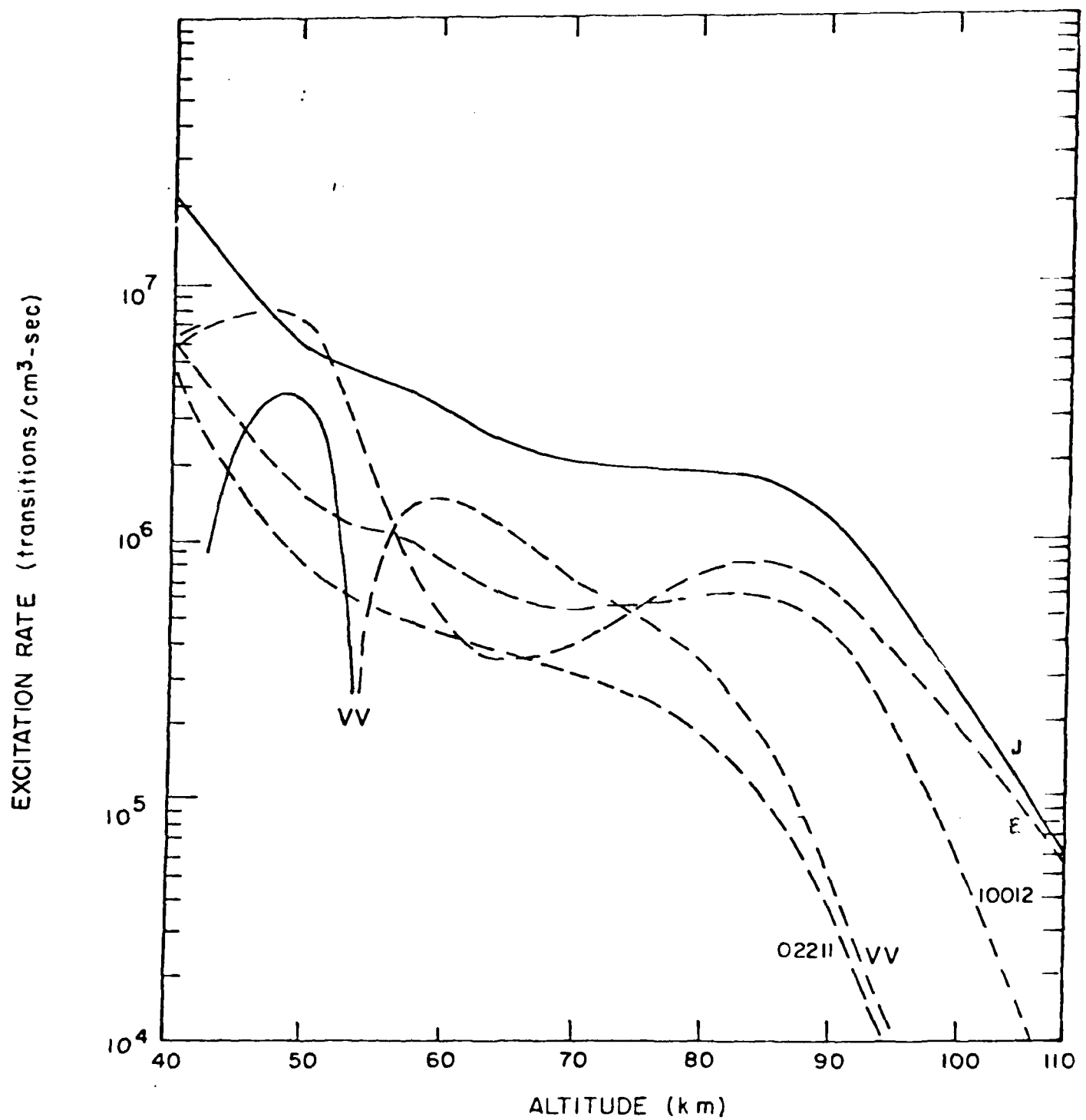


Figure 8. Same as Figure 7, but for the 10111 level.

weak. Nevertheless there is strong radiative coupling to the low-lying 01101 state, which is populated strongly enough by various collisional and radiative processes that solar pumping to the 1111x levels is very important. There is also radiative and N_2 -collision V-V coupling to the 11101 and 11102 levels, which are not so highly populated. The net effect of both of the latter is to quench the higher states, but in the altitude range below 55 km it is important not to discard the excitation component of these processes and retain only the obvious de-excitations. Above 55 km, however, these omissions would be of little consequence.

Reference to Figures 9-11 shows that, apart from the collisional exchanges among themselves, 11112 and 11111 are populated almost entirely by solar pumping. Depletion is primarily due to V-V interactions with N_2 below 74 km and spontaneous emission above this altitude. The collisional interactions rearrange the populations within the group, as before. The collisional coupling to the 03311 side level, which is quenched by the same processes but lacks an important radiative excitation channel, tends to deplete the other two levels.

The third group of states, including the 2001y levels, is simpler to discuss because the only excitation mechanism of any importance is solar pumping. (The net effect of V-V interactions with N_2 is so strongly to quench these states that it makes no difference if this is disregarded as an excitation mechanism.) The bulk of the pumping comes from ground to the 2001y levels, but near 50 km there are, as reference to Figure 4 shows, important contributions due to absorption near $2.7\mu m$ both to these main levels and also to the 12211 and 12212 side levels. Nevertheless for altitudes above 60 km the populations of the six states can be explained almost completely by absorption of $2.0\mu m$ solar flux, redistribution by collisional interactions, and quenching by N_2 at lower altitudes and by radiation at higher ones. 74 km is again the altitude at which these quenching mechanisms are of equal importance. As is typical, the side levels 1221x are mostly populated by energy transfer from the 2001y levels. Since these also have the possibility of radiating at $2.7\mu m$, however, including them does not greatly diminish the total emission

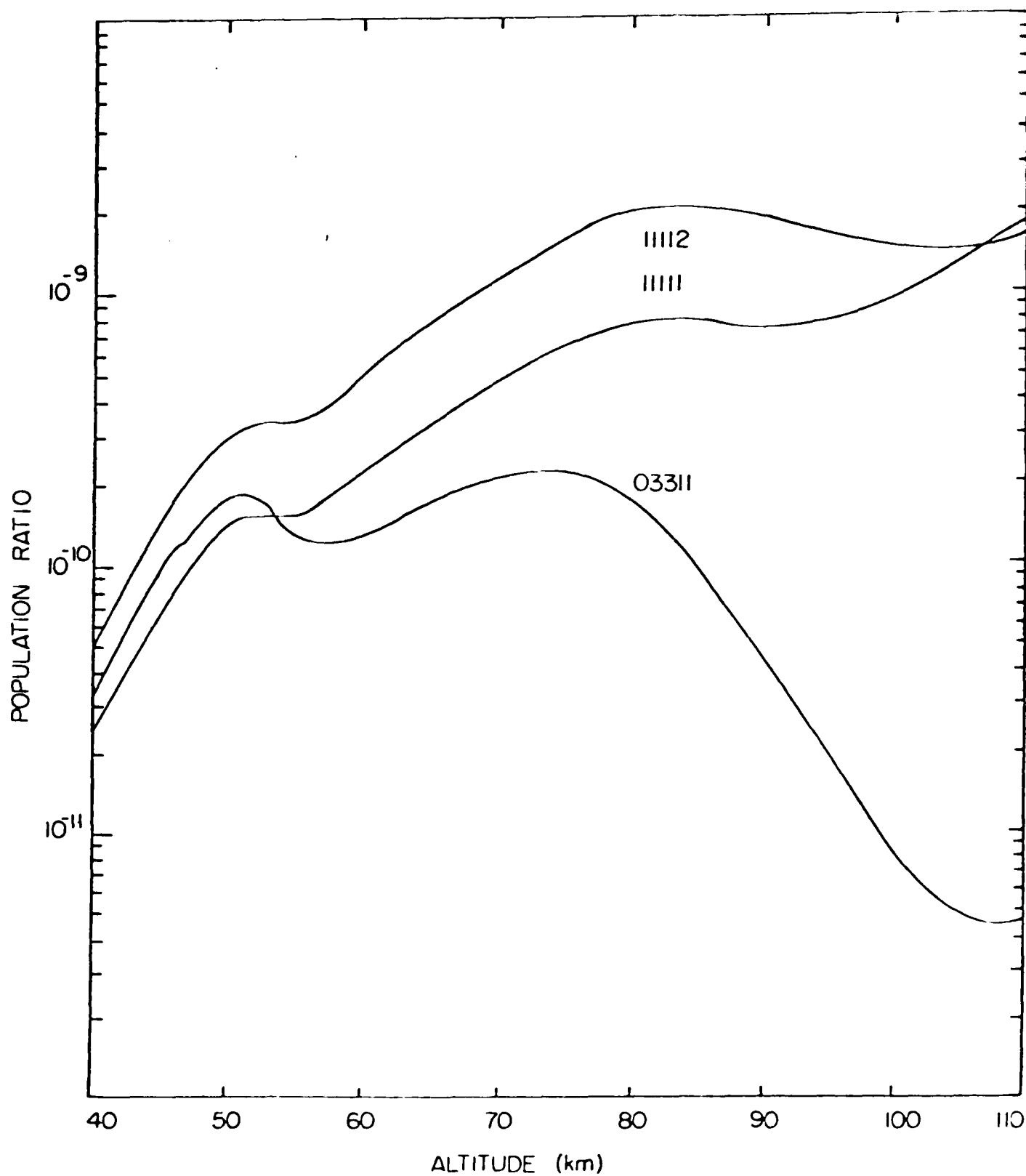


Figure 9. Ratios of the populations of the three vibrational levels in Group 2 to that of the ground state for the 626 isotope.

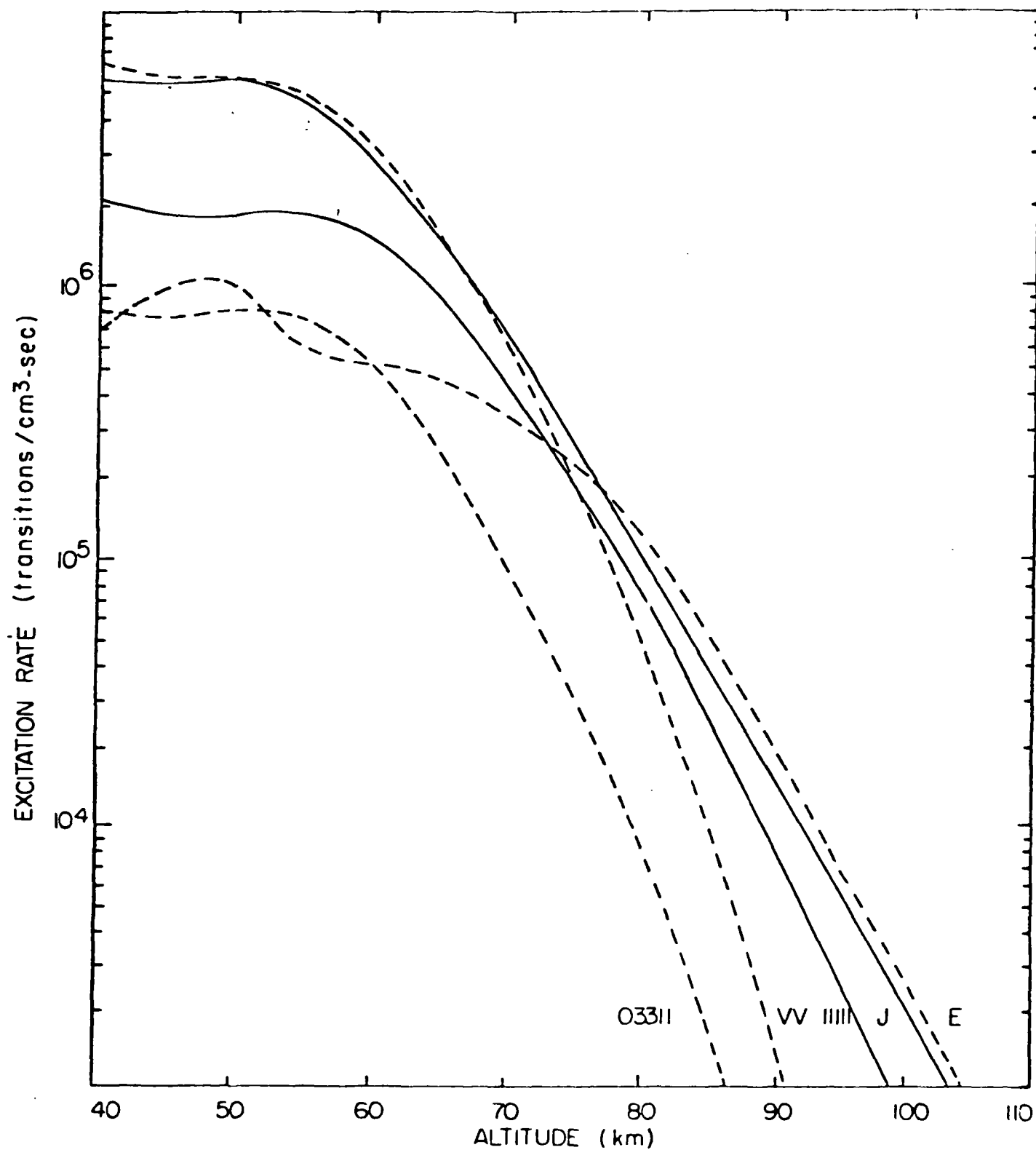


Figure 10. Excitation and de-excitation rates for the 11112 level. Symbols have the same meanings as in Figure 7.

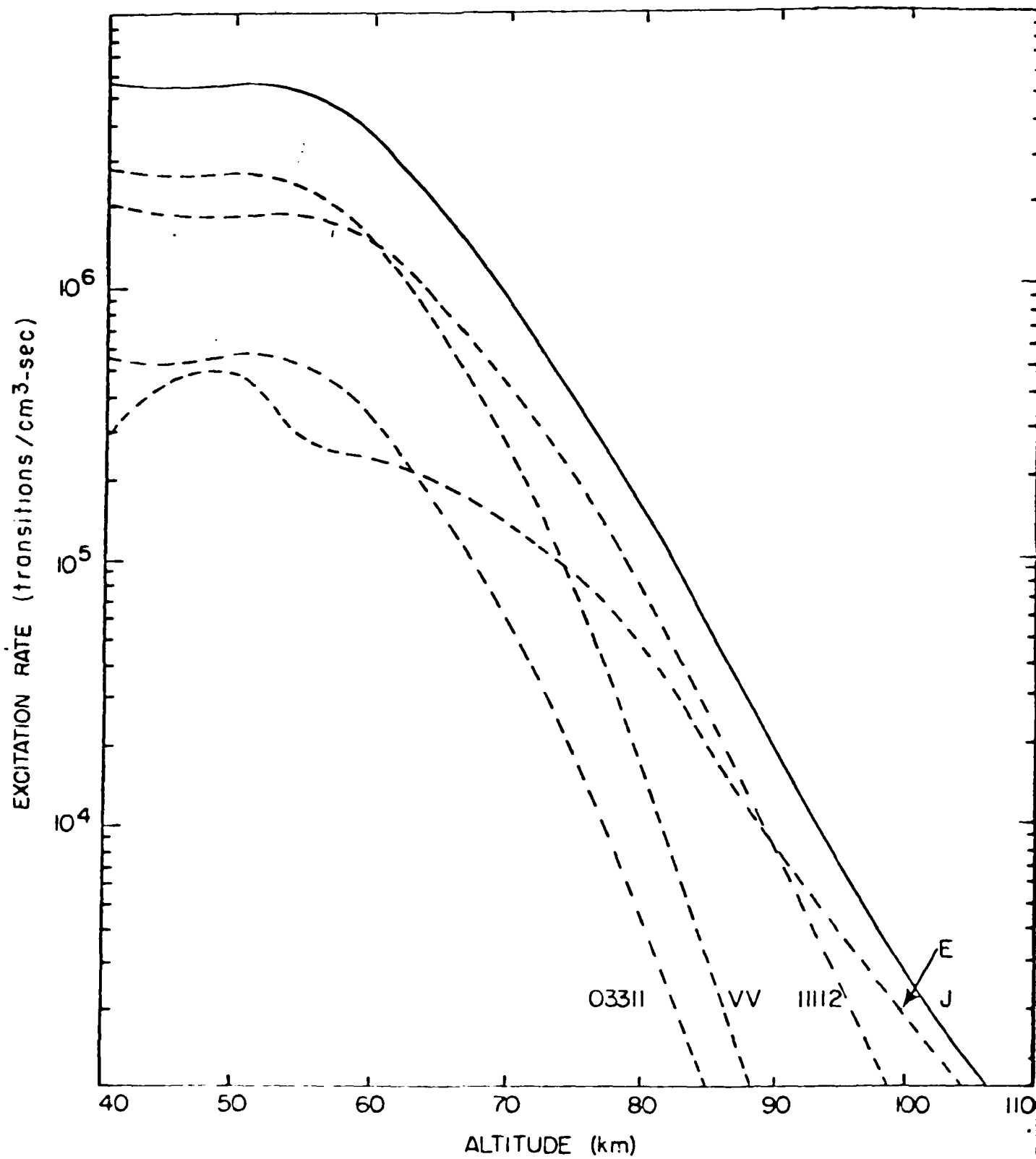


Figure 11. Same as Figure 10, but for the 11111 level.

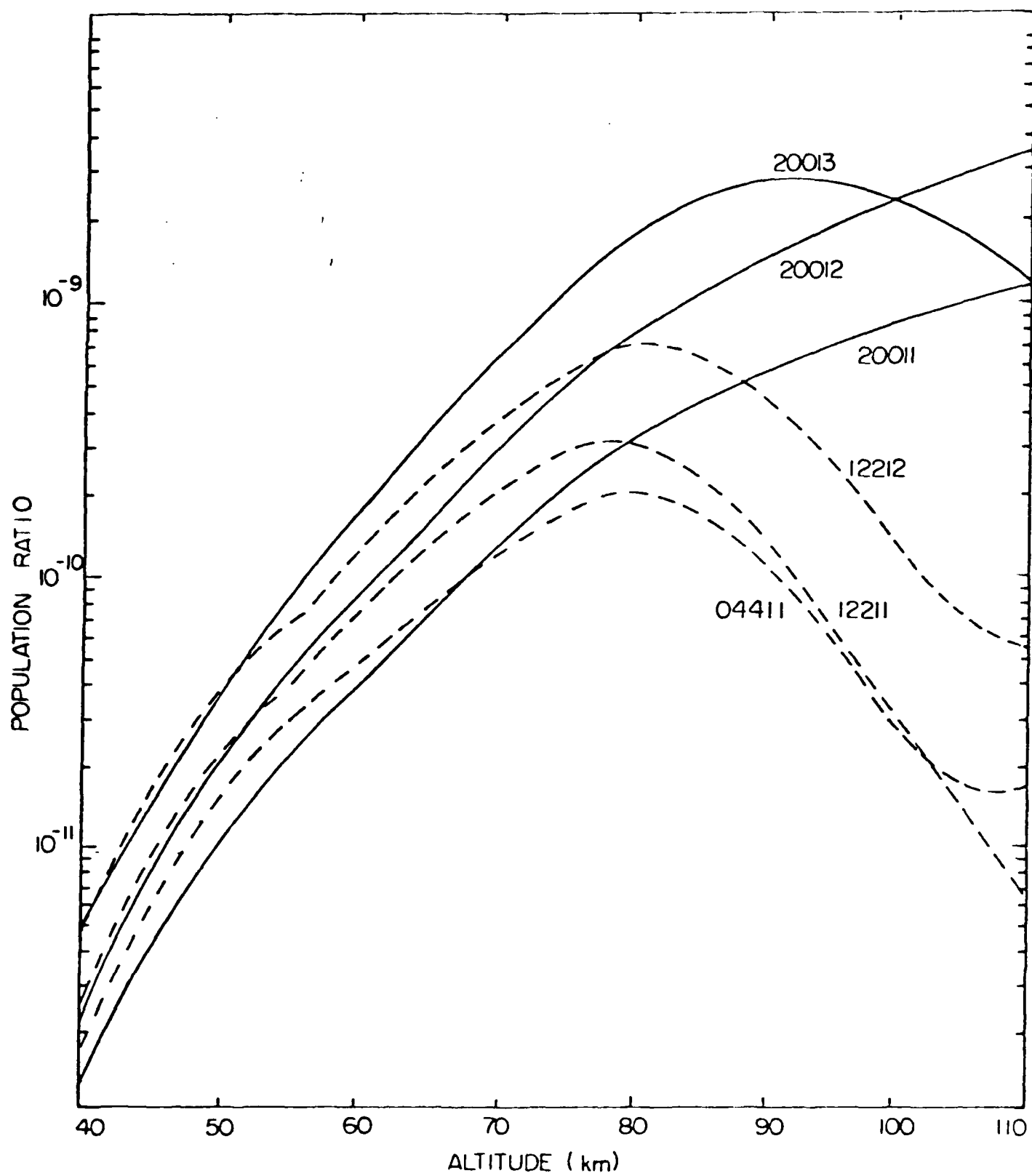


Figure 12. Ratios of the populations of the six vibrational levels in Group 3 to that of the ground state for the 626 isotope.

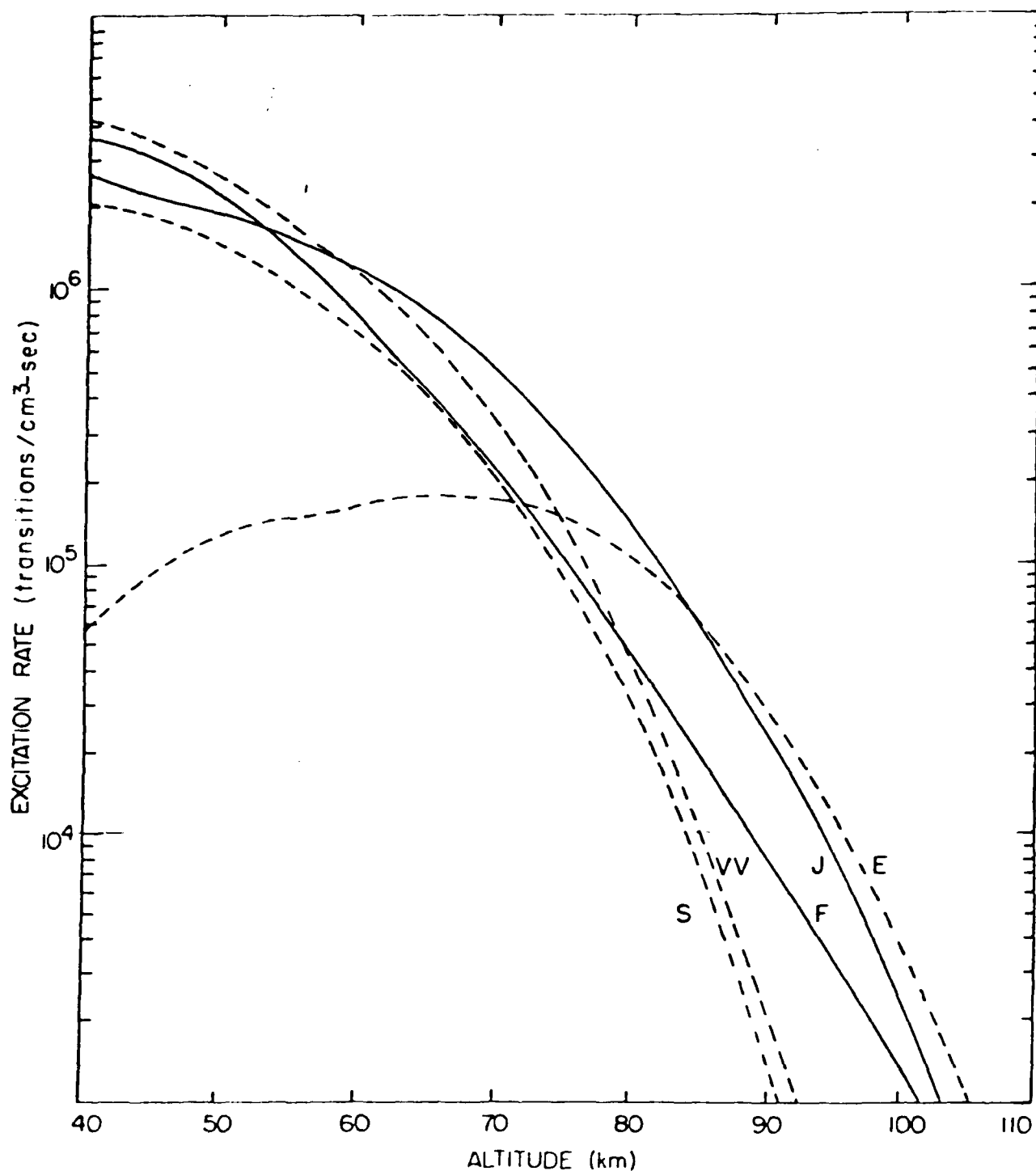


Figure 13. Excitation and de-excitation rates for the 20013 vibrational level. Solid lines represent net excitation; dashed ones, net de-excitation. "J" refers to solar pumping, "E" to spontaneous emission, "VV" to collisions with N_2 molecules, "F" to collisional interactions with other Fermi-resonance split states in Group 3 (20011, 20012), and "S" to collisional interactions with the three remaining levels in Group 3.

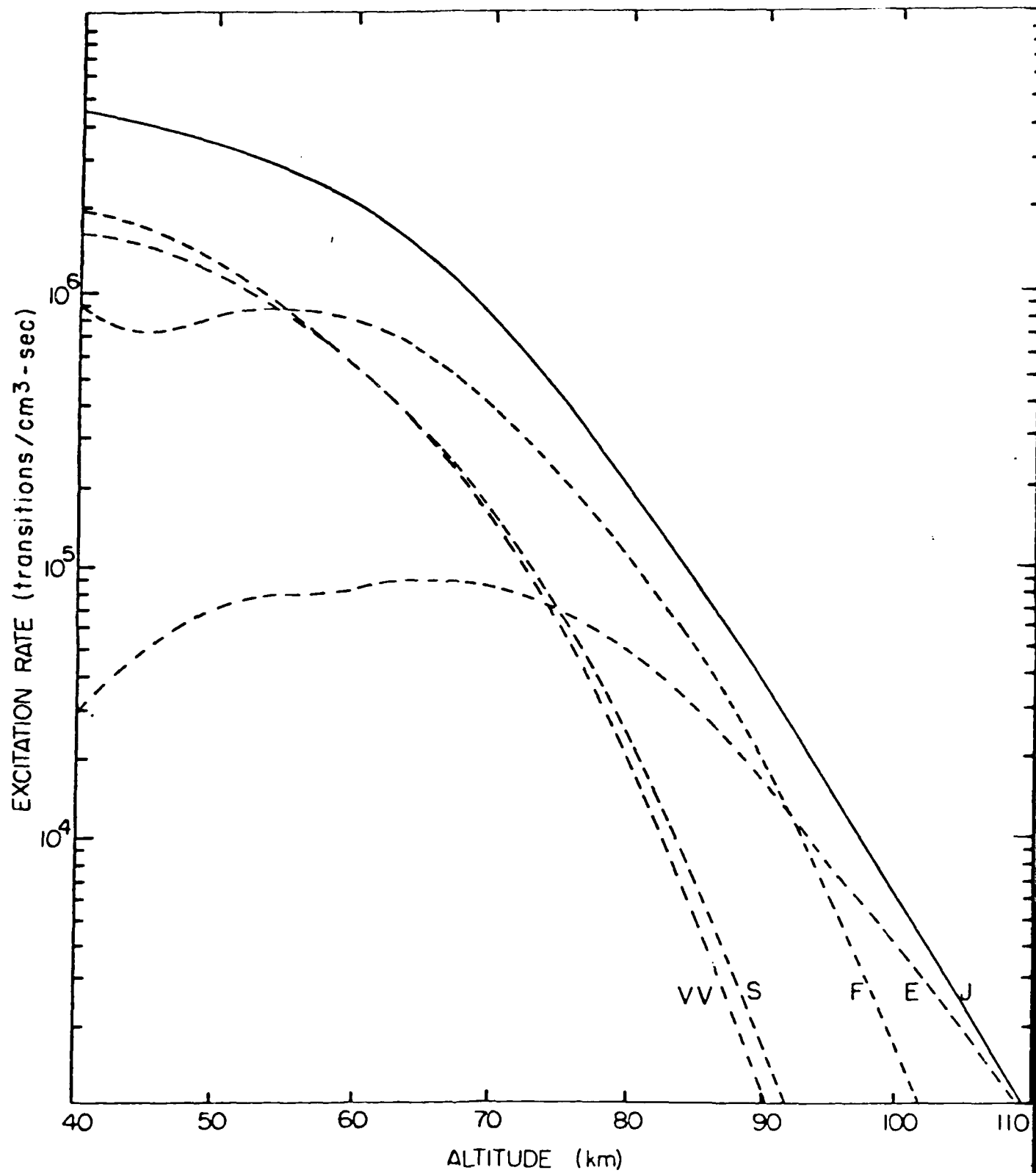


Figure 14. Same as Figure 13, but for 20012.

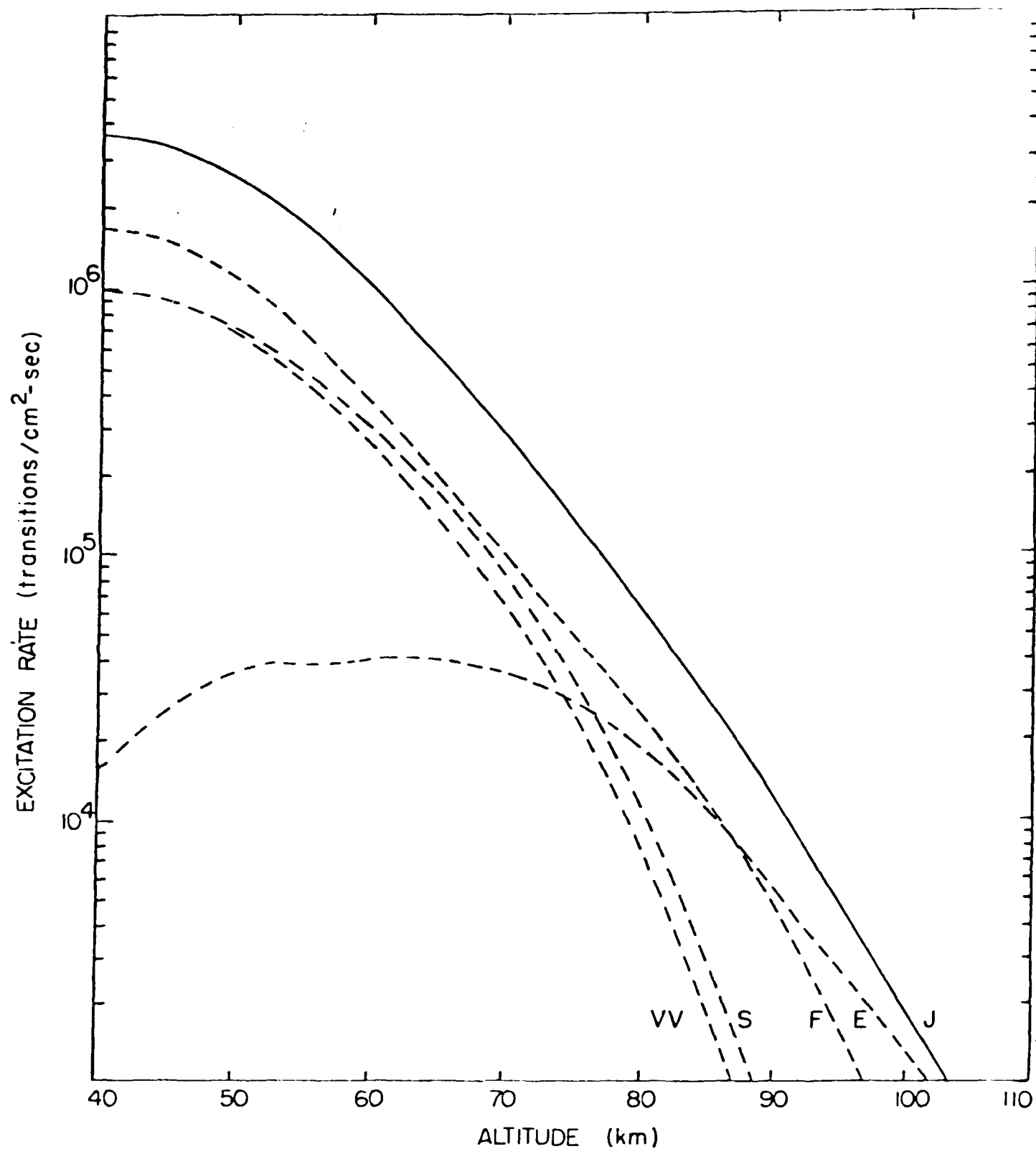


Figure 15. Same as Figure 13, but for 2001.1.

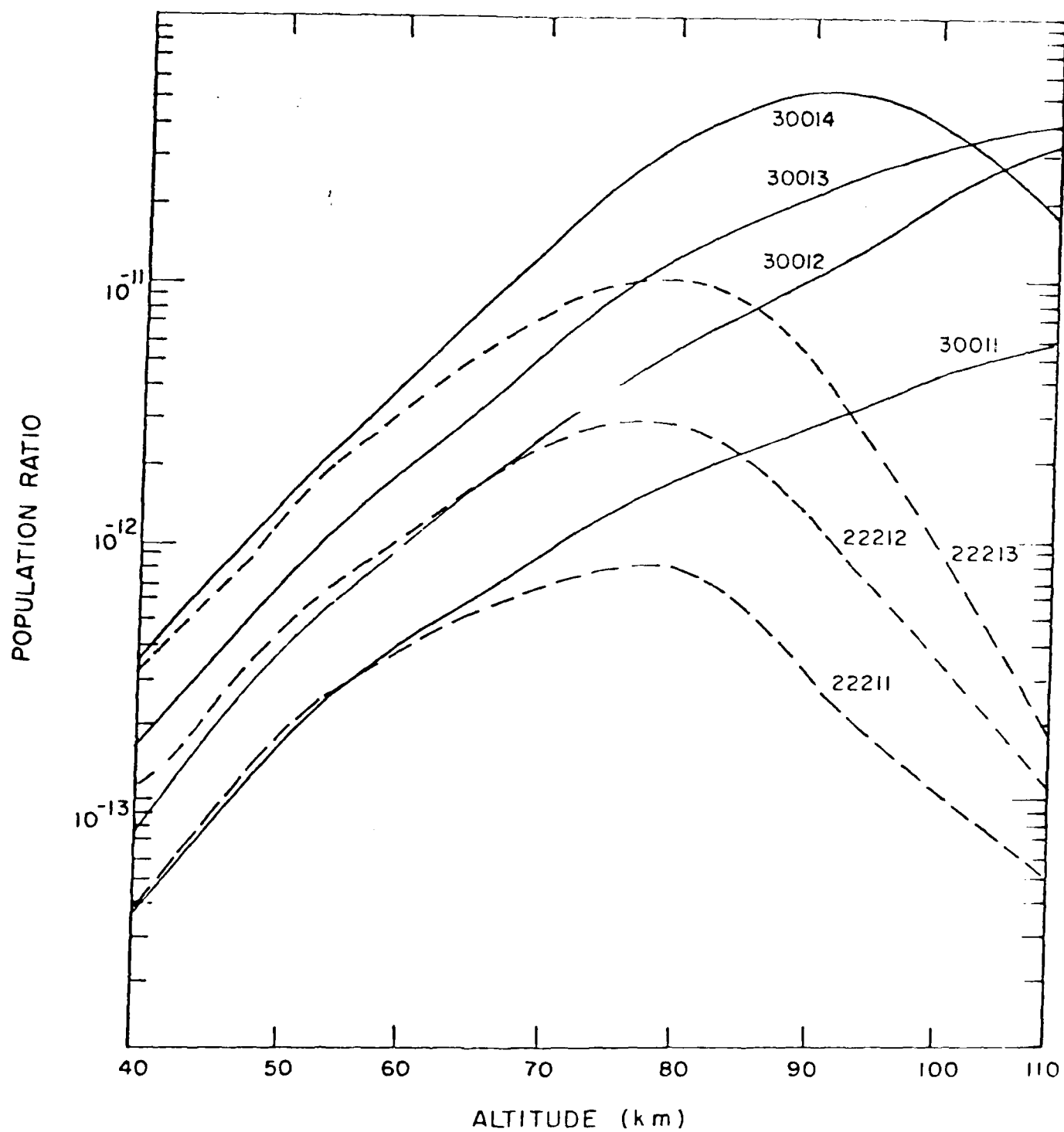


Figure 16. Ratios of the populations of the seven vibrational levels of Group 4 to that of the ground state for the 626 isotope.

calculated in the end, even if there is some redistribution in frequency. This is, however, not true of the other side level, 04411.

Figures 12-15 give the quantitative results.

Most of the comments used to describe Group 3 also apply to Group 4. In this case, however, the solar pumping is much weaker and the end result is populations which are not large enough to contribute appreciably to the total observed radiance. We plot the populations of these levels in Figure 16 for the sake of completeness.

5. RADIANCE CALCULATIONS

The radiance calculations were performed using the line-by-line code NLTE<14> in limb-look geometry. Most of the procedures are similar to those mentioned in connection with program SABS, except that it is now necessary to account for continuous emission along the whole line-of-sight path.

The most important result of this study is presented in Figure 17, which gives the total integrated radiance in the $2.7\mu\text{m}$ region as a function of the tangent height of the line-of-sight path, and also breaks it down into contributions from the sets of bands identified in Table 1. It is clear from these curves that the dominant contribution at high altitudes comes from the resonant transitions, set A, while at low altitudes the fluorescent bands of set B, bands involving transitions 200ly-1000x, are the most important component. (Their contributions are equal for the path with a tangent-height of approximately 77 km.) Next in importance are the bands of set C, and the resonant bands of the minor isotopes, summed (set G). Set D gives 10% of the total for the 60 km path but drops rapidly in importance with increasing altitude, as do all bands whose upper states are populated primarily as a result of collisions. The two lowest curves, resulting from states in Group 4, contribute at most 2% of the total and need not be considered. In addition, the 200ly-1000x bands of the minor isotopes, not shown, fall in the range between these last two curves.

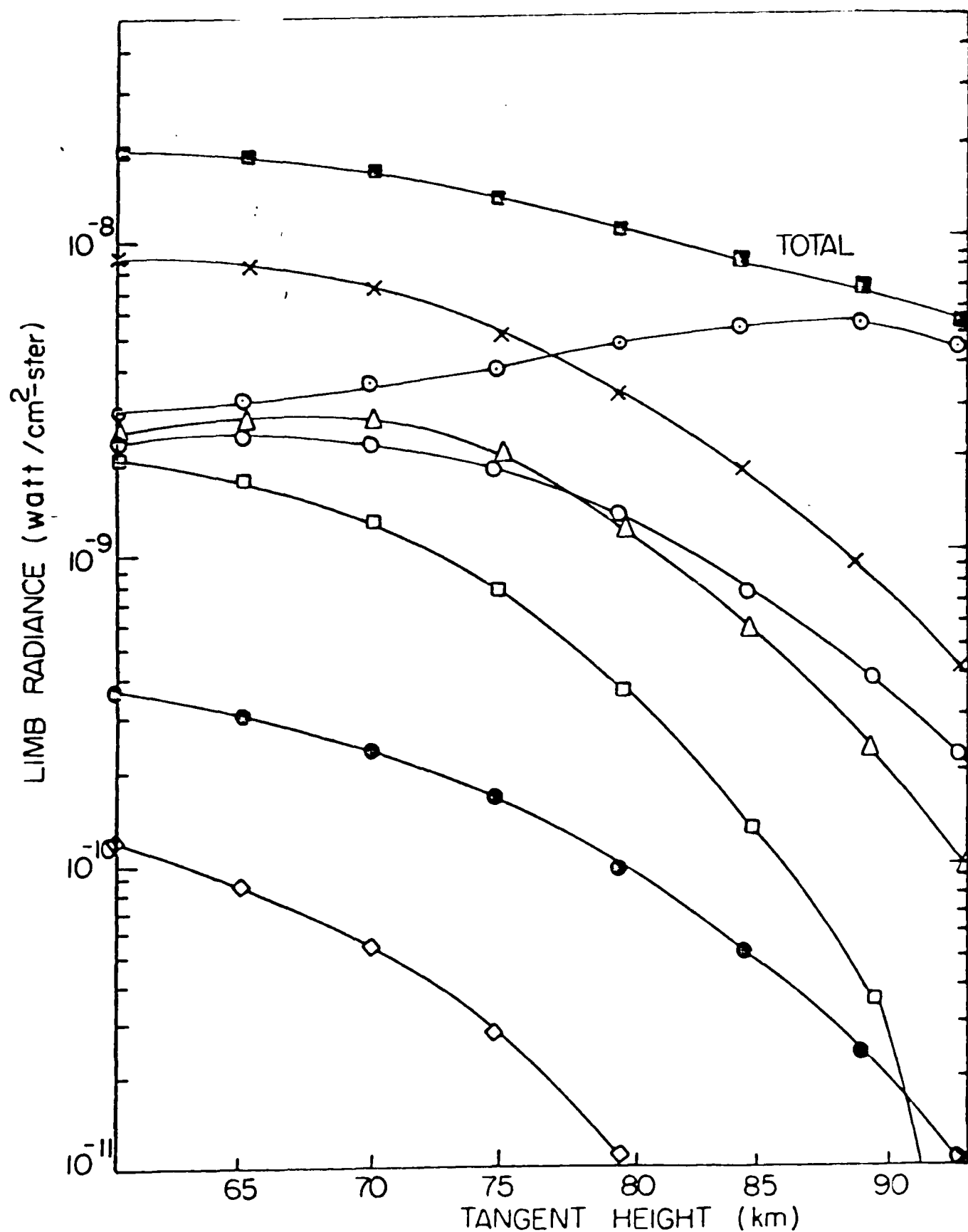


Figure 17. Band radiance in the 2.6-2.9 μm range, as a function of tangent height. Contributions from the different sets of bands identified in Table 1 are:
 ○ Set A, x Set B, Δ Set C, ● Set E, ◇ Set F, ○ Set G.

The radiance contributed by the major-isotope resonant bands, set A, changes very little over the range of line-of-sight paths because self-absorption is important even for the highest paths. On the 100 km path, for which these bands comprise 90% of the total radiance, the optical depth parameters, τ_c , are about 1.3 and 2.0 for 10012-00001 and 10011-00001, respectively, and the actual contributions are greater than for the 60 km path. All the other bands have only thin lines on the 100 km path, and their contributions simply reflect the upper-state populations, which of course decrease rapidly with increasing altitude. In fact, the only other bands for which self-absorption plays an important role at any altitude above 60 km are the minor-isotope resonance bands, set G, and the major-isotope 1111x-01101 hot bands of set C, whose lower state is only 667 cm⁻¹ above ground. At 60 km the largest τ_c value for any band in set B is about .5, which implies a little attenuation along that path.

One can see from Figure 17 that between 60 and 75 km it is important to consider at least five contributions to the total radiance. No single family comprises more than 45% of the total in this altitude range. On the 60 km path the contributions from sets B, A, C, G, and D are 45%, 16%, 13%, 13% and 11% respectively; for the 75 km path they are 37%, 28%, 15%, 14% and 5%.

Figures 18 and 19 give the spectral distribution of radiation between 2.6 μ m and 2.9 μ m. In order to obtain this, the NLTE output for each line was convolved with an instrumental scanning function appropriate to the SPIRE experiment. The lines were approximated by delta functions with amplitudes equal to the integrated radiance. A triangular scanning function with a FWHM of 52 cm⁻¹, or .038 μ m (<2 σ) was used to simulate the effect of this instrument.

Figure 18 gives the total predicted spectral radiance from all the CO₂ bands for paths with tangent heights between 60 and 100 km. One notable feature is that the relative size of the two peaks changes substantially with tangent height. This occurs because of the diminishing importance, with increasing altitude, of collisional excitation and de-excitation mechanisms as compared with radiative mechanisms. That is, collisions have the effect

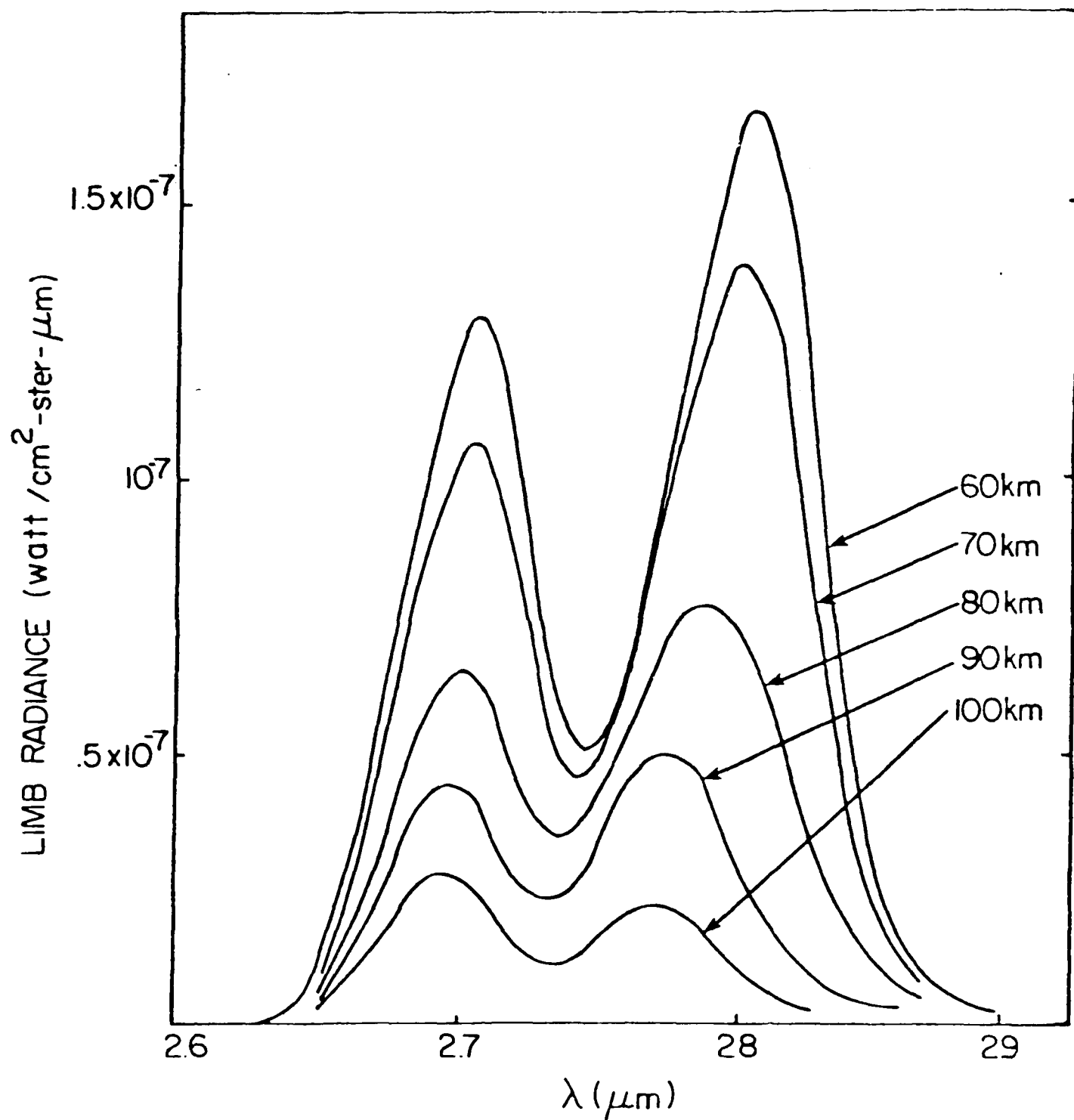


Figure 18. Spectral distribution of limb radiance, from the basic model. Curves refer to tangent heights between 60 and 100 km.

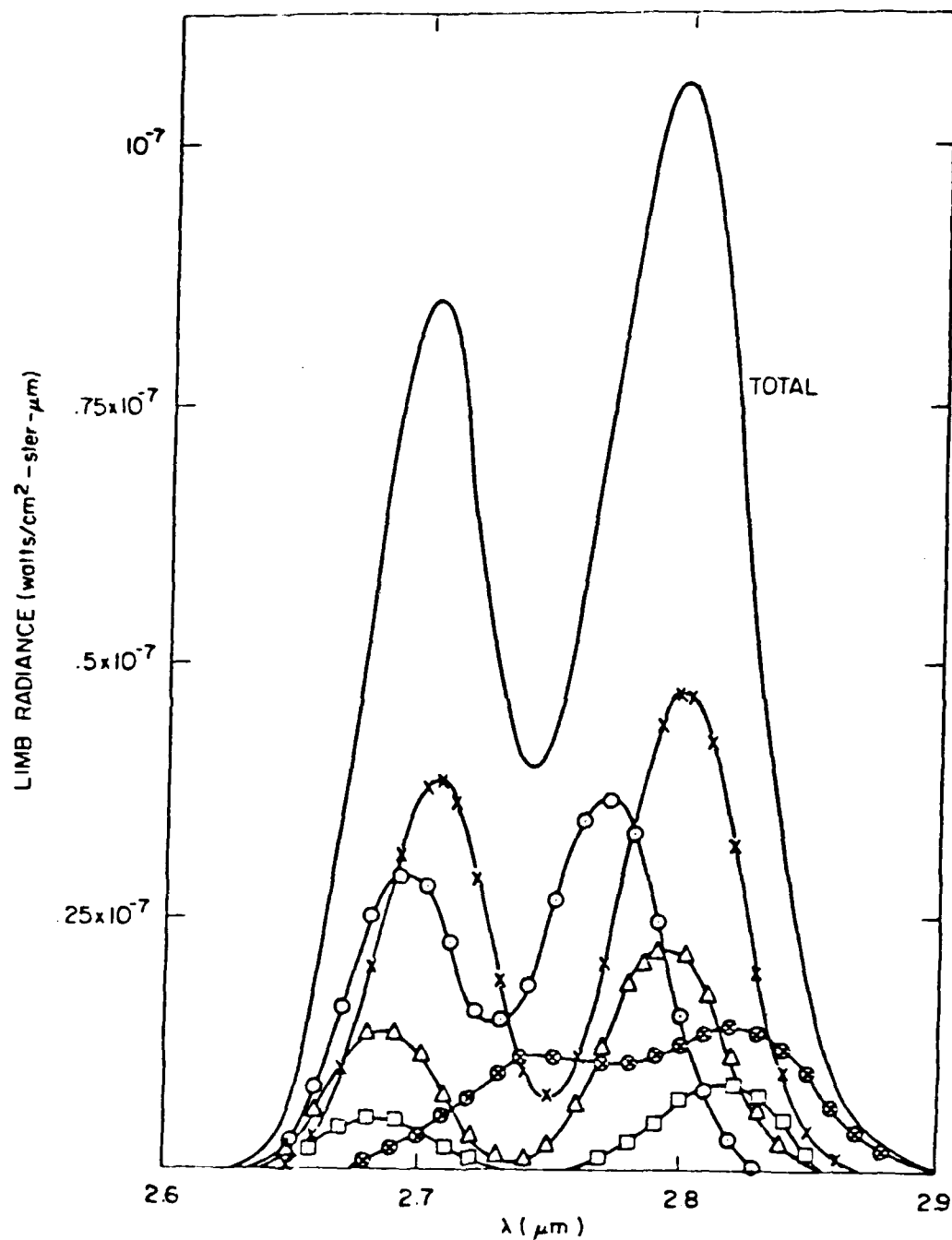


Figure 19. Spectral distribution of limb radiance for the path with a tangent height of 75 km. Components are sets of bands as in Figure 17, except that \otimes refers to G and sets E and F not included.

of diminishing the population of higher-lying levels within each group and enhancing that of the lower ones, and the net result for lower altitudes is more radiation at longer wavelengths. On the other hand, at 100 km the radiative excitation and de-excitation mechanisms stand alone and (because the pumping to the 10011 level is more likely than that to 10012, as discussed above) the shorter-wavelength peak is larger for paths that traverse regions near and above this altitude.

Another point worth noting is the shifting of the longer-wavelength peak from about $2.80\mu\text{m}$ to about $2.77\mu\text{m}$ as the tangent-height increases from 60 to 100 km. This is a result of the decreasing importance of two of the fluorescent bands in set B, which peak at slightly longer wavelengths, when compared to the resonant band at $2.77\mu\text{m}$. The shorter-wavelength peaks are more nearly coincident.

Figure 19 gives a breakdown of the total spectral radiance seen on the 75 km path by sets of bands, including only the five most prominent contributions. It is interesting to note that the long-wavelength tail of the distribution ($\lambda > 2.85\mu\text{m}$) is primarily determined by the minor-isotope emission.

6. MODIFICATIONS TO THE BASIC MODEL

In order to assess quantitatively the effects of including the intra-group collisional interactions, we performed the vibrational-population and radiance calculations using alternative values for the rate constants.

The first modification (Mod1) consisted of setting those rate constants which couple the side levels to the principal radiating levels---e.g., k_{12} in Table 2---equal to zero. This has the effect of eliminating the influence of these levels (02211 in Group 1; 03311 in Group 2; 12211, 12212, and 04411 in Group 3; 22211-22213 in Group 4) on the vibrational population calculations.

In modification number 2 (Mod2) the rate constants coupling the Fermi-resonance split states---e.g., k_{13} in Table 2---as well as those coupling

them to the side levels were set equal to zero, thereby making all levels of each group independent of all others. This results in calculations which are most like those previously reported <4>.

Modification number 3 (Mod3) is the same as the basic model, except that the rate constants connecting the Fermi-resonance split levels were increased by a factor of 100. These levels are thereby coupled more strongly to each other.

Figures 20 and 21 summarize the overall effect of making these alterations by plotting, respectively, the total radiance as a function of tangent height and the $2.7\mu\text{m}$ spectral radiance for the 75 km tangent-height path, each calculated under the assumptions of the basic model and those of Mod1 and Mod2. Mod3 produces radiances which hardly differ from those of the basic model.

Two things become clear from comparing the results of the basic model to those of Mod1 and Mod2. First of all, the rate at which collisions redistribute the populations of the Fermi-resonance split levels among themselves has a great influence not only on the spectral distribution, but also on the total emission. Secondly, the decoupling of the side levels has the anticipated effect of increasing the emission from the principal radiating levels, but it is by an amount which is considerably less than that resulting from decoupling all the levels. A more detailed examination of the results reveals that the principal differences between the Mod2 curves and the others comes from much greater populations of, and hence emission from, certain states of Group 3, primarily 20012.

The most general conclusion that can be drawn is that the observed radiance depends very strongly on the collisional interactions among the high-lying states, and that it is very important to know the rate constants for the reactions coupling these states.

To see how the changes depicted in Figures 20 and 21 arise, we examine Mod1 and Mod2 in more detail. Mod1 decouples the side levels completely and removes a quenching mechanism for the more important radiating states. In

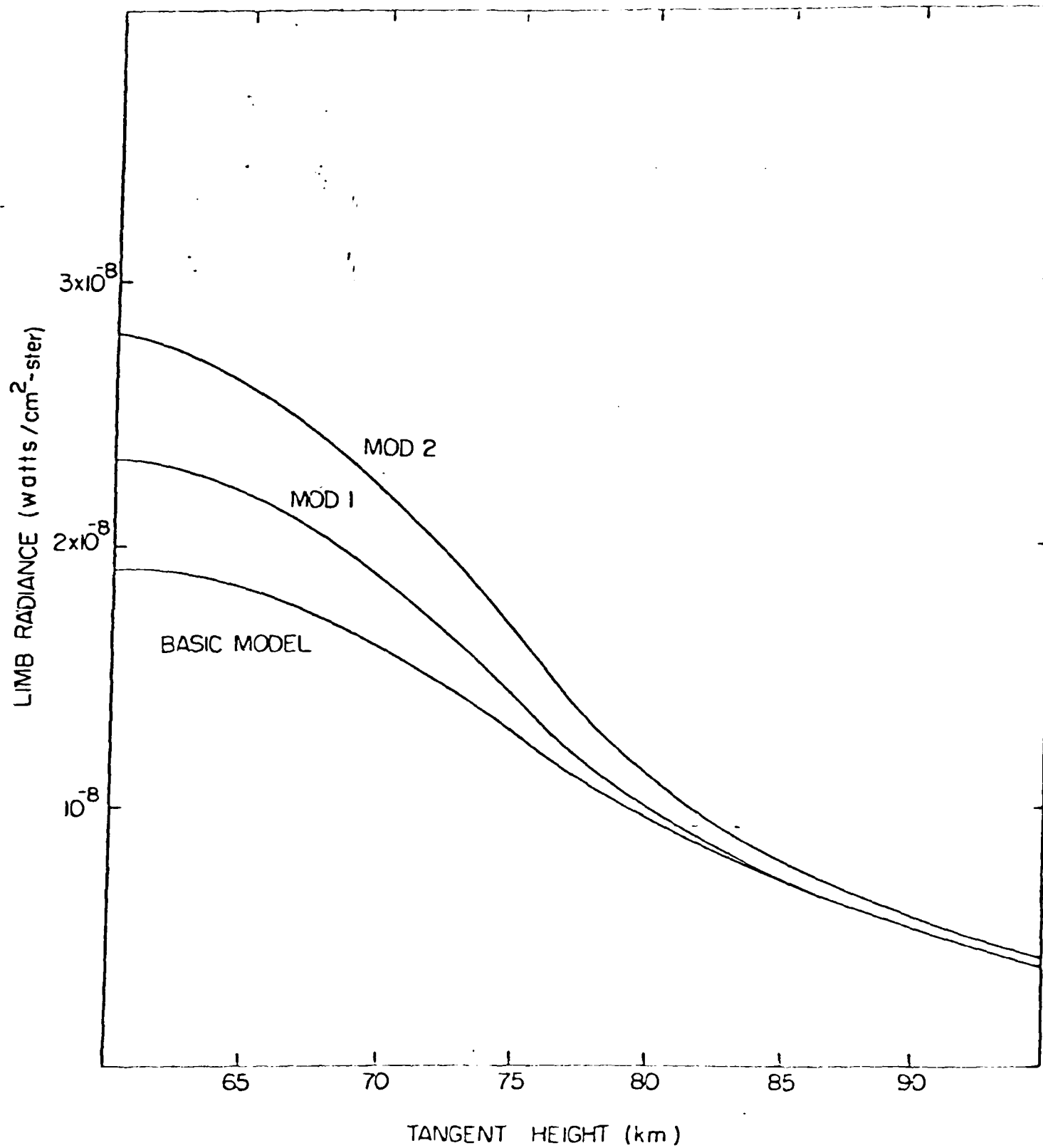


Figure 20. Integrated limb radiance from the basic model and from two modifications, as a function of tangent height.

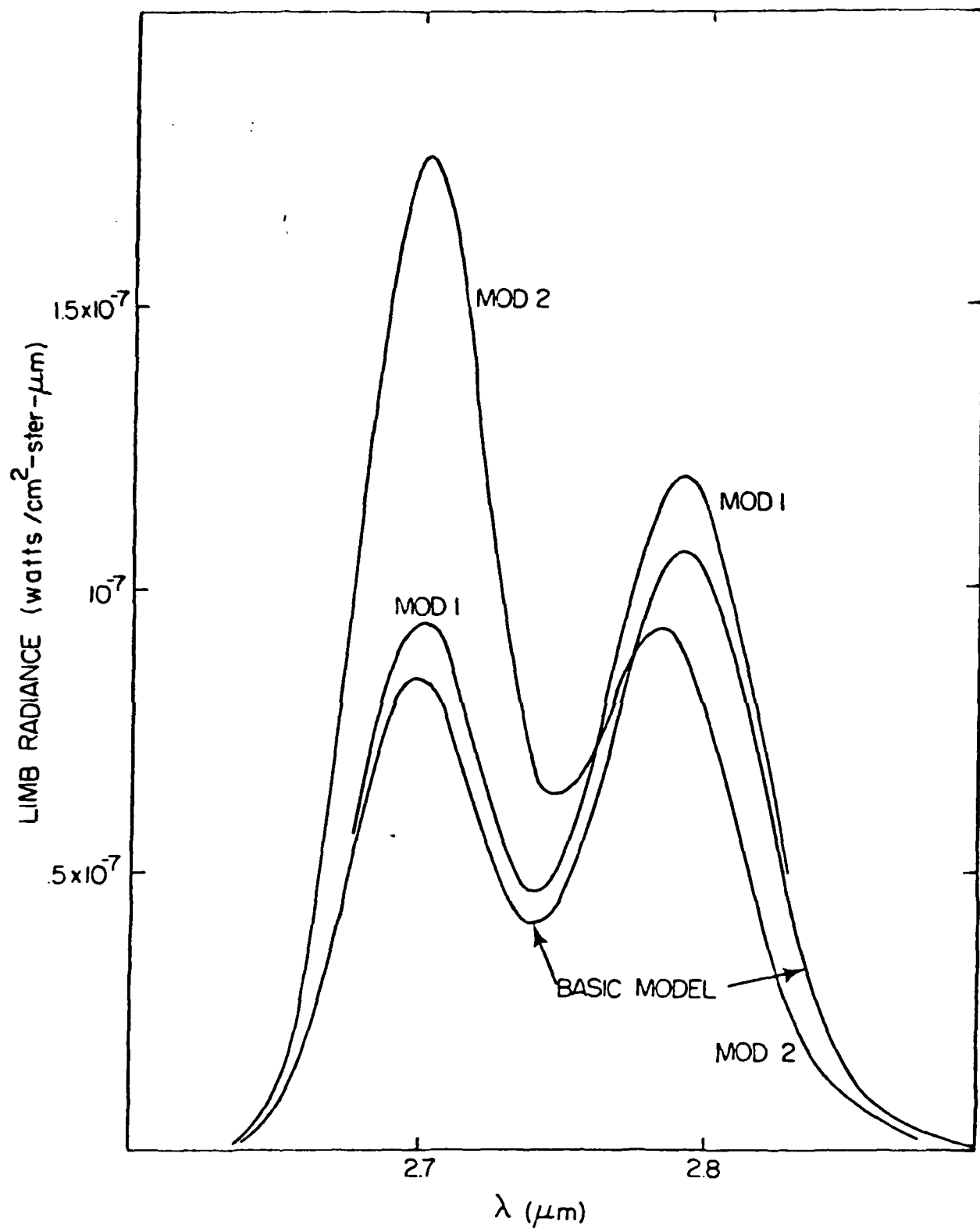


Figure 21. Spectral distribution of limb radiance from the basic model and from two modifications for a path with a tangent height of 75 km.

Figure 6 the dashed line gives the populations of Group 1 states under these assumptions. It shows that above the altitude (approximately 55 km) where N_2 excitation is unimportant the 02211 state is not highly populated. The 1001x populations are augmented by as much as 20% between 60 and 80 km, but the limb radiance resulting from them is increased by a smaller percent because of self-absorption. In Group 2, the 1111x populations are augmented by 15% or less.

Mod1 strongly affects the populations of the 2001y states of Group 3, with increases of 80% at some altitudes and appreciable effects all the way from 40 to 90 km. This more dramatic response to the decoupling of the side levels reflects the lower excitation rates and the greater number of quenching channels (compared to the 1001x levels) for these states. The change in the total limb radiance from the basic model is mostly due to these augmented populations, and occurs despite the near-complete elimination of the contribution from the bands of set D originating in the 1221x side levels.

The Mod1 spectral distribution is not significantly different from that of the basic model.

The second modification---namely, decoupling all the high-lying states from each other---has very important implications. In Mod1 the Fermi-resonance split states are still strongly coupled, so the additional limitation imposed by Mod2 results only in the redistribution of the populations of the excited states, compared to Mod1. One would thus expect little change in the total emission from Mod1 to Mod2. This neglects, however, the important fact that the states which are most strongly coupled to ground---and which therefore are more strongly pumped---may radiate more (or less) strongly in their respective $2.7\mu\text{m}$ bands than other states in the same group. The absence of the collisional redistribution will therefore result in more (or less) total emission from these states. This is a pertinent consideration for the 1001x levels and the 2001y levels. In fact, the Einstein A coefficient for the transition to ground of the 10011 level (16.9 sec^{-1}) is about 50% greater than that of the 10012 level (11.0 sec^{-1}), so (as can be seen from Figure 2 above 90 km) the solar pumping of this level is greater

and also the probability of radiation at $2.7\mu\text{m}$ from this level is greater. Since this level is actually depleted in favor of 10012 by collisional interactions, the proper result is less emission than is found when (as in Mod2) these levels are assumed to be independent.

The same result holds for the 2001y family of Group 2. One can see from Figure 4 that for altitudes at which attenuation of sunlight is unimportant the 20012 level is much more strongly pumped than the other two. It happens that the total Einstein coefficient for emission at $2.7\mu\text{m}$ from 20012 is greater than that of the lower-lying 20013 (18.1 sec^{-1}) and higher-lying 20011 (33.5 sec^{-1}). The net effect of decoupling these levels, then, is to keep the more weakly-radiating lowest level from acquiring the large population collecting in the middle and upper levels. Mod2 therefore predicts a considerably greater total emission near $2.7\mu\text{m}$ than the basic model, as shown in Figure 20. This result calls attention to the need to carefully consider the collisional interactions.

Figure 21 shows that the changes which constitute Mod2 give a strikingly different spectral distribution from that of the basic model. This occurs because of the greater weighting of Mod2 accords the higher-lying states, which radiate more prominently in shorter-wavelength bands.

Mod3 is, in some sense, the opposite of Mod1 and Mod2 because it couples the principal radiating states more, rather than less, strongly. The quantitative result is that the populations are weighted slightly more heavily toward the lower vibrational levels, as one would expect. Below 85 km the population differences are too small to be seen on the logarithmic scale of Figures 2-5; above 85 km the redistribution is more obvious. By the converse of the logic employed in the discussion of Mod2 in the last two paragraphs, one expects this to reduce the observed radiation. This turns out to be the case, but since emission from Group 3 is relatively unimportant above 85 km the limb radiance is not affected dramatically.

7. COMPARISON WITH EXPERIMENTAL RESULTS

The $2.7\mu\text{m}$ emission seen by SPIRE <4-6> and other experimental probes has components due to molecules other than CO_2 . The most important of these is H_2O , which radiates in four bands between $2.68\mu\text{m}$ and $2.75\mu\text{m}$. The possibility of contributions from the OH fundamental on the long-wavelength side cannot be ruled out, either.

Modelling the water contribution is made difficult by the uncertainty in, and variability of, the mixing ratio for H_2O . Degges <15> has determined that the SPIRE data at $6.3\mu\text{m}$ and $2.7\mu\text{m}$ for paths with tangent heights up to 75 km are consistent with a mixing ratio of 1.5 parts per million by volume, although higher values are not ruled out. He has calculated the H_2O contribution in the $2.5\text{--}2.9\mu\text{m}$ region on this basis. In Figure 22 we compare the results of our basic model for CO_2 , Degges' results for H_2O , and the total of these quantities with the SPIRE dataset for tangent heights between 50 and 90 km.

Figure 22 shows that below 70 km there is good agreement between the total predicted limb radiance and the experimental values, which do not vary strongly with altitude. Above 75 km the emission falls off rapidly into the range of detector noise. In fact, the data are very noisy at these altitudes, and it is only possible to say that the actual emission must be less than $1.6 \times 10^{-8} \text{ watt/cm}^2\text{-ster}$, the noise level. Since the CO_2 prediction is less than this, no conclusion can be drawn regarding it. The H_2O prediction of limb radiance is significantly above this for tangent heights between 75 and 85 km, however, a fact that suggests that the correct water vapor mixing ratio over most of the range above 75 km must be less than 1.5 ppm.

Figure 23 presents spectral data in the $2.5\text{--}3.5\mu\text{m}$ region, with the background subtracted out. These data correspond to a tangent height of 73 km. We also show the H_2O component <15> and the combined CO_2 and H_2O prediction. The latter provides a respectable representation of the data. It somewhat overestimates the experiment at $2.70\mu\text{m}$, in the shorter wavelength CO_2 peak

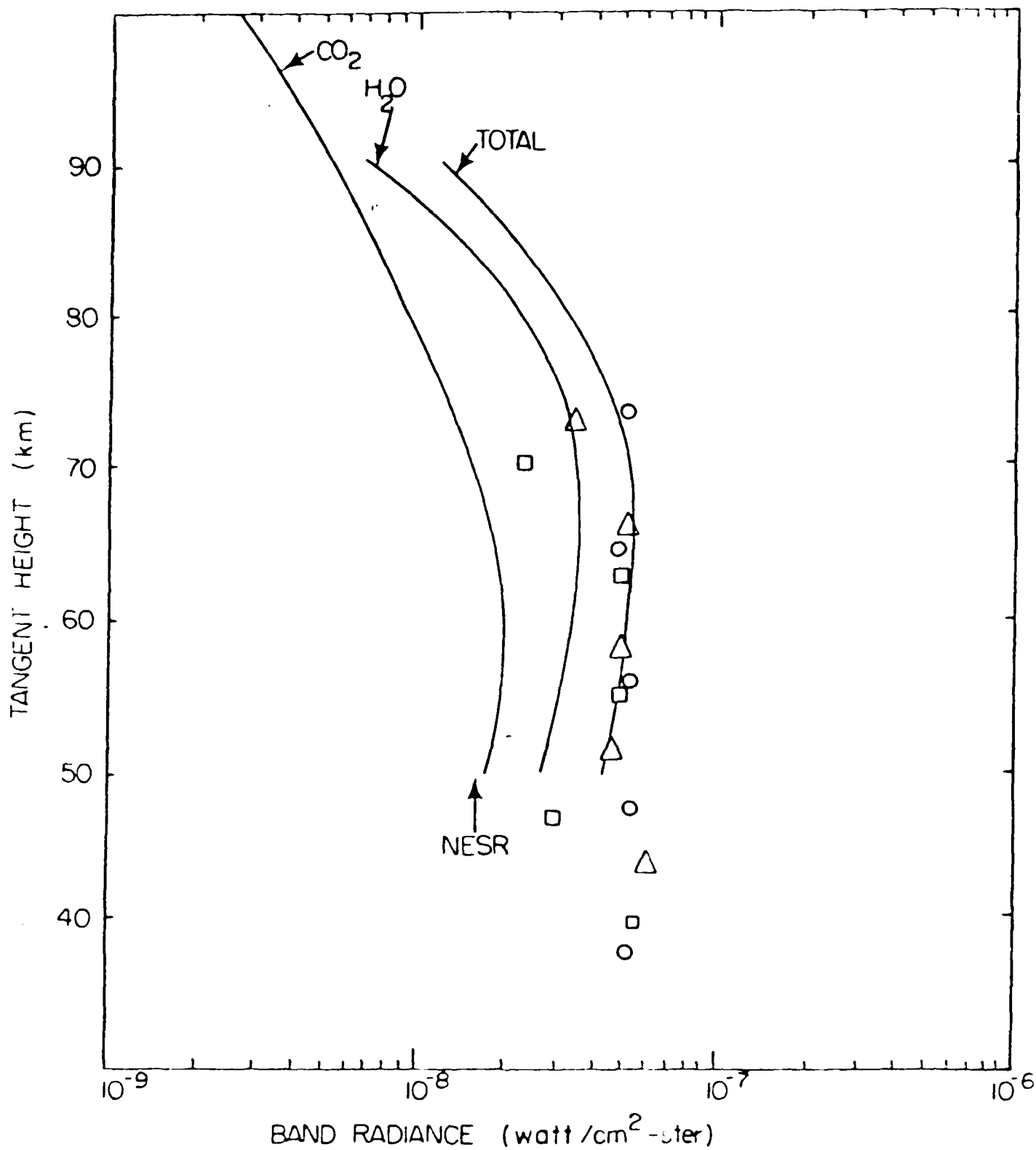


Figure 22. Band radiance, 2.5 to 2.9 μ m, from scan 9 (O), scan 10 (Δ) and scan 11 (\square) of the SPIRE experiment; and the results of the CO₂ model, the H₂O model <15>, and their total. Detector noise limit is indicated by the arrow.

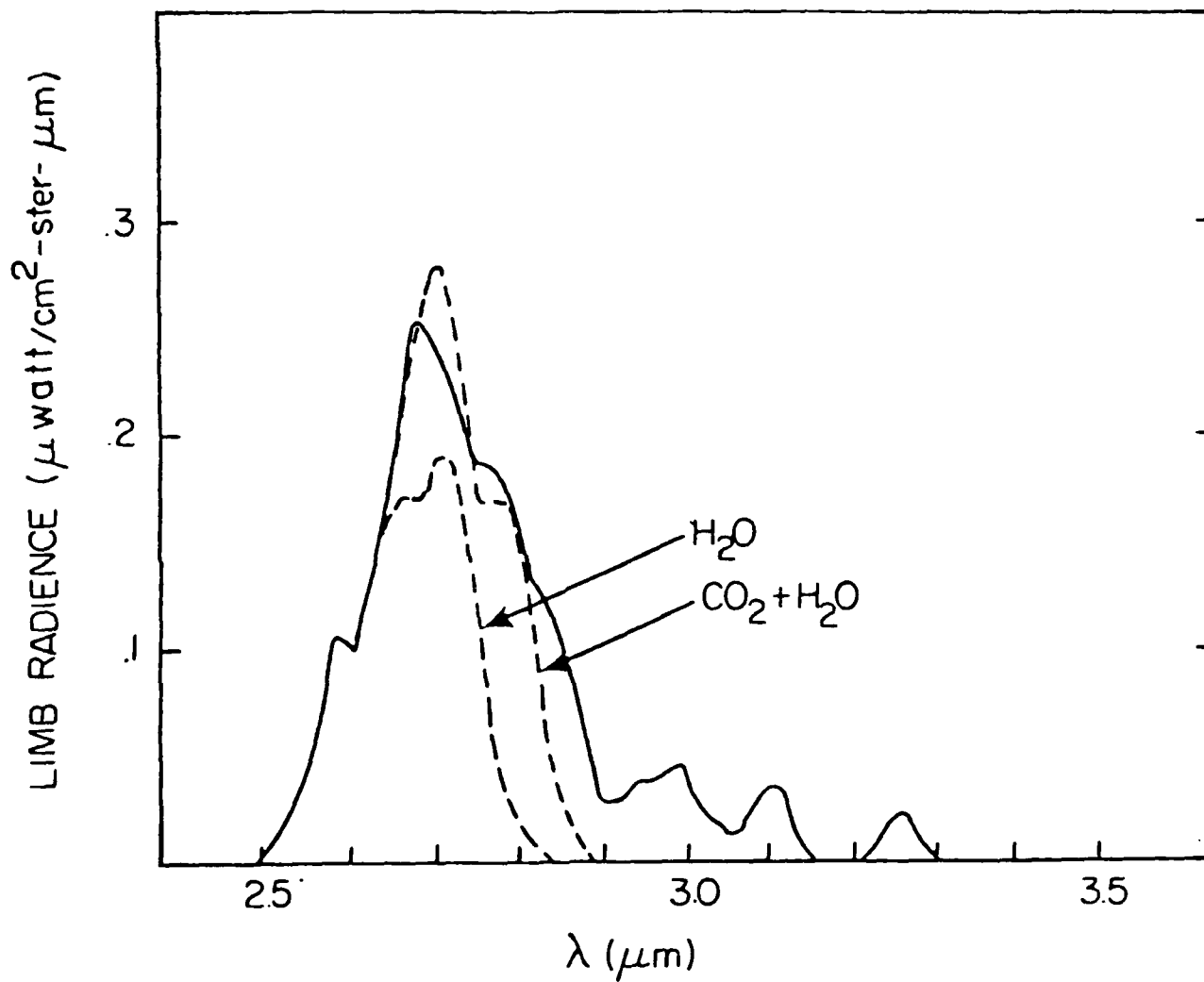


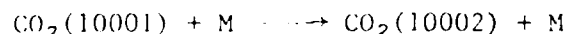
Figure 23. Limb radiance from the SPIRE experiment (solid line) in comparison with predictions of contributions from CO_2 (this model) and H_2O (IRR<9%).

(c.f. Figure 18); and it underestimates it on the long-wavelength side of the CO₂ spectrum and beyond. This fit illustrates quite clearly the importance of including the collisional interactions in the CO₂ model. That is, if the results of the basic model were replaced by the Mod2 results (c.f. Figure 21) both the overestimate of the experiment at 2.70μm and the underestimate beyond 2.80μm would be exaggerated rather than diminished.

It should be pointed out that the water calculation is a band model calculation, and may not represent the spectral distribution as precisely as appears necessary to resolve the discrepancies between the combined model and the experiment in the 2.7-2.8μm region.

8. DISCUSSION

It is clear from the discussion of the last two sections that the interactions coupling the states within each of the groups of high-lying states play a major, albeit not dominant, role in determining the CO₂ contribution to the 2.7μm radiance. The values of the rate constants used in the basic model, given in Table 2, were chosen to be the same as those coupling the 10001-02201-10002 states in IRR <9>. In fact, k_{13} is the lower limit proposed by Taylor <10> for the rate constant characterizing



These values are not known with great accuracy, and we also do not know exactly what differences can be expected between the constants coupling states of this low-lying group and those characterizing our four high-lying groups. The values used in our basic model thus represent educated guesses of how strong the interactions are. The purpose of making the changes described as Mod1-Mod3 was to crudely evaluate the effect of these guesses on the observed radiance.

The effect of reducing k_{13} can be seen, from Mod2, to be to increase the 2.7μm emission. If the H₂O contribution predicted by Degges <15> is

correct, the overall fit in the 50-70 km region precludes the possibility of a larger CO₂ component. Thus the value we have used for k_{13} could be a lower limit, in accord with Taylor <10>. We have not shown that some lower values are inconsistent with the data, but since k_{13} determines the largest de-excitation rate for the very important 20012 and 20011 states (c.f. Figures 14 and 15) it is likely that modest reductions in its value will lead to larger populations, and therefore greater emission.

Because the Fermi-resonance split levels are in near equilibrium with each other up to about 85 km, increasing k_{13} (Mod3) has little effect on the emission in the region where good data are found. Above 85 km the reduction in the predicted radiance is less than the uncertainty in the H₂O contribution. For these reasons, it is impossible to decide from this model whether a larger value for k_{13} is appropriate.

The effect of reducing k_{12} is to weaken the coupling between the principal radiating levels and the side levels, and thus to increase the populations of the former. This results in greater emission from them. By reasoning similar to that pertaining to k_{13} , we conclude that the value for k_{12} found in the basic model represents a lower limit. In contrast, larger values cannot be ruled out. An order-of-magnitude increase in k_{12} causes a decrease in emission which removes the overall H₂O-CO₂ prediction from agreement with the experiment. However a larger water mixing ratio---2 ppm in the 50-70 km range, which is still consistent with the SPIRE results in the 6.3 μ m region <15>---could make up the difference. A smaller value of k_{13} might have the same effect.

One result which has not been mentioned can be seen in Figures 7 and 8: in a range of altitudes between 42 and 52 km the net effect of collisions between N₂ and CO₂ molecules is to excite, rather than deplete, the 1001x levels of CO₂. Generally this mechanism quenches high-lying CO₂ levels. In this altitude range LTE is believed to prevail for the low-lying levels involved in these transitions (e.g., 1000x, 02201), and the resulting populations happen to be great enough that reactions 4 and 6 in Table 2 run in

reverse. One implication of this result is that for paths intersecting this altitude range some $2.7\mu\text{m}$ emission should appear even for night-time conditions. The SPIRE detectors did not observe night-time emission at this wavelength. This is explained by the fact that in the absence of solar pumping our model predicts limb radiances from these bands on the order of 10^{-9} watt/cm²-ster, which is well below the noise level of the instruments.

9. CONCLUSION

A model for the prediction of CO₂ emission in the $2.7\mu\text{m}$ region has been developed, and tested by simulating the conditions of the SPIRE experiment. A new line-by-line code has been used to evaluate the rates of absorption of solar flux in many relevant bands. These rates have been combined with assumed rates for inter- and intra-molecular collisional interactions to evaluate the populations of high-lying levels responsible for emission in the 101 combination bands. The limb radiance has been calculated from these populations. In combination with emission from water vapor predicted by another model <15>, it has been compared with the SPIRE dataset for daylight conditions. Rate constants for the intramolecular collisional interactions have also been altered to test the effect of possible errors in their values.

In general the model has been found to give good agreement with the experiment. It has also established the need to include the intramolecular collisional interactions in calculating the vibrational populations of the high-lying levels. Among our specific conclusions are that (1) the resonant transitions 1001x-00001 dominate the limb radiance above 75 km; (2) the fluorescent transitions 2001y-1000x are most significant on lower viewing paths, but several other sets of bands, including those of minor isotopes, contribute a sizable portion of the observed radiance; (3) the principal excitation mechanism is solar pumping over the entire range of altitudes considered, even when the line centers are so completely bleached out that absorption occurs primarily in the Voigt wings; (4) the high-lying levels are de-excited primarily through radiative processes above 75 km and through collisions

with N_2 below 75 km; (5) the intramolecular collisional transfer rates strongly affect the (integrated) limb radiance and also the spectral shape of the emission; and (6) the values of the rate constants used to characterize these interactions could be adjusted upward without causing conflict with the data, but a significant downward revision appears to be inappropriate.

10. REFERENCES

1. A. T. Stair, Jr., R. D. Sharma, R. M. Nadile, D. J. Baker, and W. F. Grieder, "Observations of Limb Radiance with Cryogenic Spectral Infrared Rocket Experiment (SPIRE), to be published.
2. R. D. Sharma, "Infrared Airglow", in Handbook of Geophysics, Chapter 13 (in press).
3. R. M. Nadile, N. B. Wheeler, A. T. Stair, Jr., D. C. Frodsham, and L. C. Wyatt, "SPIRE Spectral Infrared Experiment," SPIE 24 - Modern Utilization of Infrared Technology, 18-24, 1977.
4. R. Sharma, R. Nadile, A. T. Stair, Jr., and W. Gallery, "Earthlimb Emission Analysis of Spectral Infrared Rocket Experiment (SPIRE) Data at 2.7 Micrometers," SPIE 304 - Modern Utilization of Infrared Technology, 139-142, 1981.
5. R. A. McClatchey, W. S. Benedict, S. A. Clough, D. E. Burch, R. F. Calfee, K. Fox, L. S. Rothman, and J. S. Garing, "AFCRL Atmospheric Absorption Line Parameters Compilation," AFCRL-TR-73-0096 (1973), NTIS #AD762904.
6. R. D. Sharma and C. A. Brau, "Energy Transfer in Near-Resonant Molecular Collisions due to Long-Range Forces with Application to Transfer of Vibrational Energy from ν_3 Mode of CO_2 to N_2 ", J. Chem. Phys. 50, 924 (1969).
7. J. B. Kumer and T. C. James, " $\text{CO}_2(001)$ and N_2 Vibrational Temperatures in the 50 <z< 130 km Altitude Range," J. Geophys. Res., 79, 638 (1974).
8. J. B. Kumer, "Atmospheric CO_2 and N_2 Vibrational Temperature at 40- to 140-km Altitude," J. Geophys. Res., 82, 2195 (1977).
9. T. Degges and H.J.P. Smith, "A High-Altitude Infrared Radiance Model," AFGL-TR-77-0271 (1977).
10. R. L. Taylor, "Energy Transfer Processes in the Stratosphere," Can. J. Chem. 52, 1436 (1974).
11. L. S. Rothman and L.D.G. Young, "Infrared Energy Levels and Intensities of Carbon Dioxide - II", J. Quant. Spectrosc. Radiat. Transfer 25, 505 (1981).
12. L. S. Rothman, R. R. Gamache, A. Barbe, A. Goldman, J. R. Gillis, L. R. Brown, R. A. Toth, J. M. Flaud, and C. Camy-Payret, "AFGL Atmospheric Absorption Line Parameters Compilation: 1982 Edition," App. Opt. 22, 2247 (1983).
13. M. P. Thekaekara, Solar Energy 14, 109 (1973), summarized in J. T. Houghton, The Physics of Atmospheres, Cambridge, Univ. Press, 1977.
14. R. D. Sharma, R. Siani, M. Bullitt, and P. P. Wintersteiner, "A Computer Code to Calculate Emission and Transmission of Infrared Radiation through a Non-Equilibrium Atmosphere," AFGL-TR-83-0168 (1983), NTIS #ADA137162.
15. T. Degges and R. Nadile, "Determination of Mesospheric Water Vapor Concentrations from Earth Limb Radiance Measurements at 6.3 and 2.7 Micrometers" (to be published).

III. IMPROVEMENTS IN THE NLTE ALGORITHM

1. INTRODUCTION

The radiance calculation involved in the comprehensive CO₂ model and in other projects which we have undertaken is carried out by program NLTE. In this section we describe modifications which were recently made to improve the efficiency and running speed of the code.

To use NLTE, it is necessary to specify a band, a branch, or a single ro-vibrational transition of a particular molecule and isotope. One then provides an atmospheric profile including, most importantly, the kinetic temperature and the number densities of the vibrational states involved in the transitions (or equivalent information), and also data from the A.F.G.L. Atmospheric Absorption Line Parameters Compilation <1-3> which pertains to the transitions in question. The program then calculates the band radiance and the spectral radiance which a hypothetical sensor would detect in either limb- or zenith-looking geometry. Radiance along many viewing paths may be determined simultaneously.

The algorithm upon which the code is based was reported in 1983 <4>, along with the initial release of the program and instructions for its use. Augmented versions of this first release have been applied to many radiance problems in the intervening period. The relatively long execution time required by this detailed calculation has been only a minor drawback to its use. In the future, however, we contemplate its use in multiple or iterative applications, within larger programs. This makes it essential to have more efficient code. The changes we report in this section have cut the run time, without a sacrifice in accuracy, by factors ranging between 5 and 30 for different problems we have considered. CO₂ bands can now be run in less than 20 seconds, using 80 atmospheric layers and 5 viewing paths.

2. PROGRAM ORGANIZATION

The flow chart in Figure 24 blocks out the subtasks performed by the main program after the input and initialization steps are complete. This chart, and

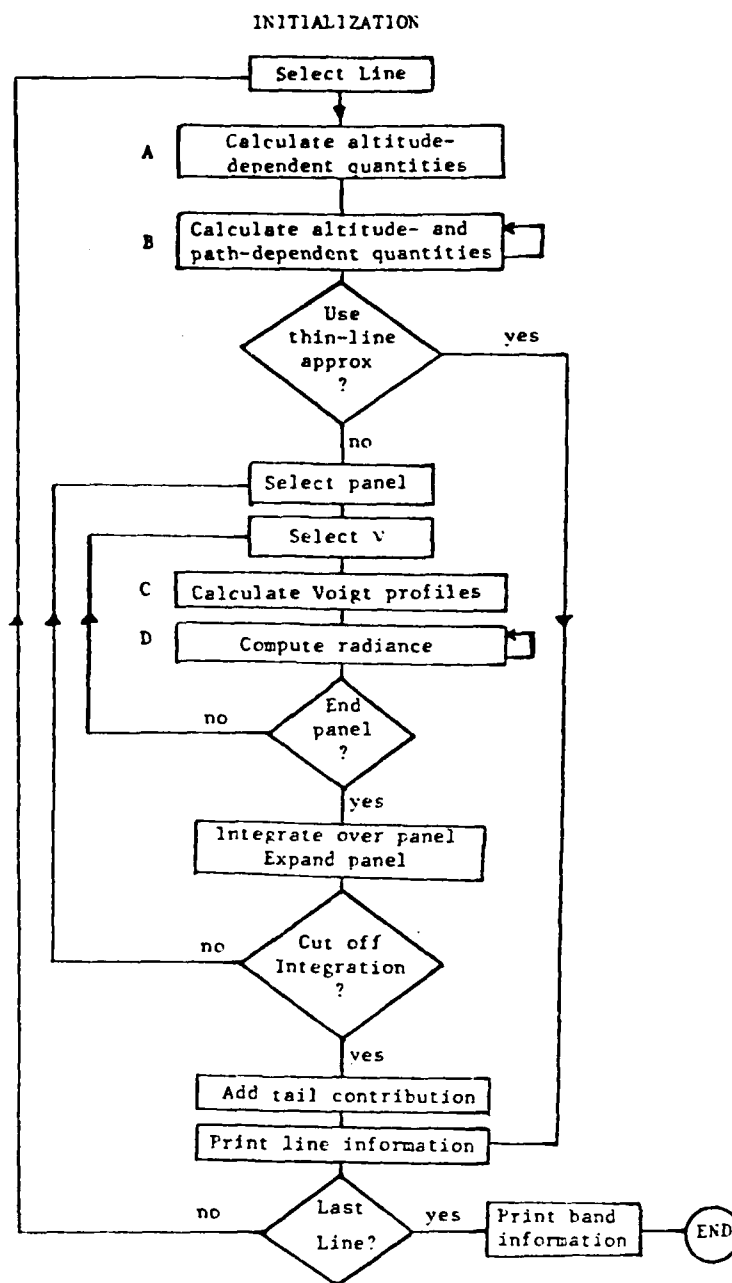


Figure 24. Partial flow chart for NLTE. Steps A, B, C, and D imply a loop over the required range of altitudes. B and D loop over the line-of-sight paths also, as indicated.

the description of the radiance calculation given below, are meant to be an introduction only to the organization of the program and are used to provide a context for our description of the program modifications. The physical assumptions and the quantities we actually calculate are given in more detail in Reference 4.

The hierarchy of information required to complete the radiance calculation can be identified as follows: (1) quantities which are independent of the transition in question, such as atmospheric profile arrays; (2) line-dependent quantities which also depend on altitude, such as the Doppler width and corrected line strengths; (3) line- and altitude-dependent quantities which also depend on the path, such as path column densities; and, (4) quantities which, in addition to the above, also depend on the frequency, ν . Given that all this information is available, the program sets ν equal to the resonance frequency, ν_0 , and begins by determining the radiance at the near edge of the farthest layer of the atmosphere on all the line-of-sight paths. (See Figure 25.) Proceeding inward toward the observer, the radiance on the near edge of the second layer is the sum of the (attenuated) contribution from the first layer and the contribution from the second layer for each path. This summation continues from layer to layer until the contribution from the last (nearest) layer is added in to give the observed radiance (in photons/sec-cm²-ster-cm⁻¹) at ν_0 . These steps constitute block D in Figure 24. Then ν is changed and the procedure repeats. When a sufficient number of points have been evaluated to provide a complete radiance profile, or spectral lineshape, a numerical integration over frequency is performed to get the total line radiance. In the end, the contributions from all the lines give the band radiance.

One can see that the radiance calculation, block D, with its loops over altitude and path, contains the most deeply embedded calculations the program. It turns out, however, that the most time-consuming calculations are those of the Voigt lineshape function, block C, which is also deeply embedded but which loops only over altitude. The obvious strategy for improving the speed of the program is therefore to substitute a faster Voigt profile routine and to reduce the number of calls to this routine. These tactics in fact are responsible for

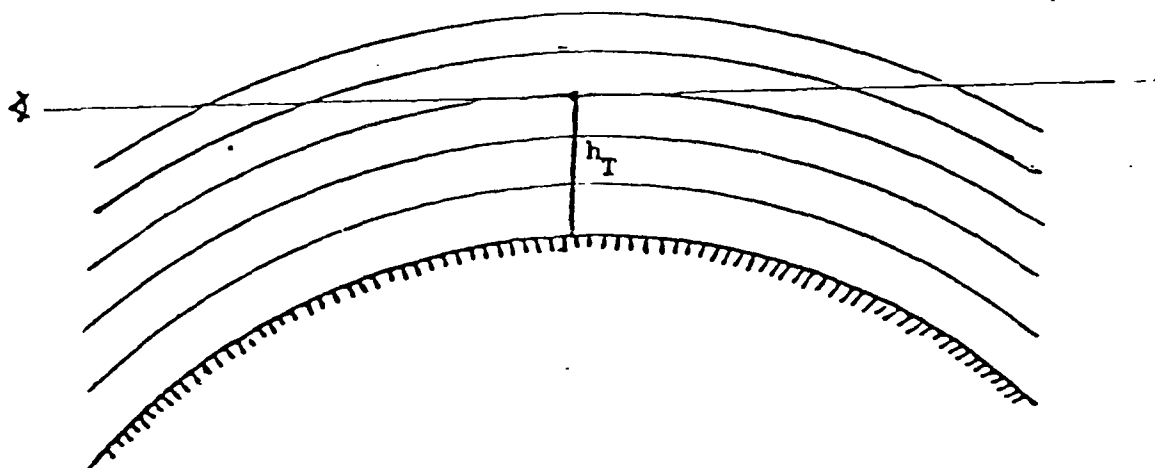


Fig. 25 Schematic diagram of a stratified atmosphere showing a line-of-sight path for exoatmospheric limb viewing. The tangent height for the path, h_T , is indicated.

the enhanced program efficiency we are reporting. In Section 3 we describe our adaptation of an existing Voigt profile algorithm which is five to six times faster, on average, than the procedure we used previously. In Section 4 we describe a new semi-adaptive integration algorithm which requires far fewer points than the compounded Simpson's rule previously in use. We also describe an analytical approximation to the tail of the radiance profile which eliminates the need to carry the computation very far from the line center.

3. VOIGT PROFILE ALGORITHMS

3.1. Lineshape Considerations

One physical assumption of the NLTE algorithm is that the frequency-dependence of the absorption cross-section (and hence the emission lineshape) is given by a Voigt profile, which is the convolution of the Doppler lineshape (a Gaussian) and the pressure-broadened lineshape (a Lorentz function). At altitudes where non-LTE conditions prevail the Lorentz component is often very weak, because of the relative infrequency of collisions in the rarified atmosphere. Even with a Lorentz-to-Doppler linewidth ratio of 10^{-2} or 10^{-3} , however, we have shown that use of the Voigt profile, rather than the Doppler lineshape which is easier to compute, is extremely important because of the much slower dropoff in the wing of the Voigt function. That is, many lines may be severely self-absorbed in the line-center even for viewing paths traversing only very high-altitude regions; in such cases the contribution in the wings, where the self-absorption is much less, constitutes a large part of the total radiance profile, and it is necessary to have an accurate representation of the lineshape in the wings. Errors of 50% to 100% can easily be made by neglecting the collision-broadening.

3.2 Basic Representation

The Lorentz, Doppler, and Voigt profiles are defined by

$$L(\nu) = \frac{1}{\pi} \frac{\alpha_L}{(\nu - \nu_0)^2 + \alpha_L^2} \quad (1a)$$

$$D(\nu) = \frac{1}{\alpha_D} \sqrt{\frac{\ln 2}{\pi}} \exp \left(-\ln 2 \left[\frac{\nu - \nu_0}{\alpha_D} \right]^2 \right) \quad (1b)$$

$$V(\nu) = L(\nu) \otimes D(\nu) \quad (2)$$

where α_L and α_D are the pressure-broadened and Doppler linewidths, respectively, and ν_0 is the resonance frequency. The linewidths are altitude-dependent through the pressure and temperature $\langle l \rangle$. Since L and D are each normalized to unity, V is also normalized. By making the substitutions

$$y = \sqrt{\ln 2} \frac{\alpha_L}{\alpha_D} \quad (3a)$$

$$x = \sqrt{\ln 2} \frac{\nu - \nu_0}{\alpha_D} \quad (3b)$$

the following form is achieved:

$$V(\nu) = \frac{1}{\pi \alpha_D} \sqrt{\frac{\ln 2}{\pi}} \int_{-\infty}^{\infty} \frac{y}{y^2 + (x-t)^2} e^{-t^2} dt \quad (4)$$

$V(\nu)$ is thus parameterized by dimensionless quantities, y and x , representing the linewidth ratio and the frequency. It happens to be proportional to the real part of a complex function, $w(z)$,

$$V(v) = \frac{1}{\alpha_D} \sqrt{\frac{\ln 2}{\pi}} \operatorname{Re}[w(x + iy)] \quad (5)$$

where $w(z)$ is related to the complex error function by <5>

$$w(z) = \frac{2iz}{\pi} \int_{-\infty}^{\infty} \frac{e^{-t^2}}{z-t} dt = e^{-z^2} (1 - \operatorname{erf}(-iz)) \quad (6)$$

and x and y are given above. Many algorithms for the Voigt function are based on this representation: one finds an efficient way of calculating $\operatorname{Re}[w(z)]$ starting with Eq. (6).

3.3 Rybicki's Algorithm

Rybicki's algorithm <6>, which was used in the first release of NLTE as function VWERF, determines $\operatorname{Re}[w(z)]$ by expanding e^{-t^2} in a sampling representation and evaluating the resulting integrals by the method of residues. This gives a series which is cut off at 31 terms. It is a highly accurate representation, giving between 8 and 12 correct significant figures over the full range of parameters we tested. Since our accuracy requirements are not nearly so stringent as this, we tried cutting off the series with fewer terms. The speed is worse than directly proportional to the number of terms, however, and the great accuracy quickly disappears for certain portions of the x - y plane when fewer terms are used. A 19-term series is still advantageous, but other methods proved to be better.

Rybicki's algorithm makes use of an asymptotic formula for very large x .

3.4 Pierluissi's Algorithm

Pierluissi et al <7> developed a fast Voigt algorithm which we have modified and adapted to our purposes.

Pierluissi's algorithm, realized as function ZVOIGT, divides the x-y plane into three regions. Region I is specified by $(0 < x < 3, 0 < y < 1.8)$. Region II is bounded by region I on one side and by $x=5, y=5$ on the other. Region III is specified by $(x > 5, y > 5)$.

In Region I, $\text{Re}[w(z)]$ is determined by using a series expansion <5> for the complex error function in Eq. (6). The number of terms in the series is a linear function of x. The maximum number of terms is 29. Each call requires evaluations of one (real) sine, cosine, and exponential. The series computation is between two and three times faster than VWERF in the comparable x-y region. Its accuracy is practically independent of y for $y < 1$, but is very sensitive to the value of x. In fact, for small x, extremely accurate values are obtained. Fractional errors of 10^{-3} and 5×10^{-3} are obtained for $x < 3.6$ and $x < 3.8$, respectively. It is not useful for $y \geq 2$.

In Regions II and III the evaluation of $\text{Re}[w(z)]$ is accomplished by 6- and 4-point Gauss-Hermite quadrature <8,9>. Since the weighting function for this quadrature is exactly the exponential appearing in the integral in Eq. (6), no transcendental function evaluations are required at all and the calculation is very fast.

Generally speaking, the accuracy of the 4- and 6-point rules is excellent for $x > 5$. It improves with increasing x and, for $x > 6$, does not depend on y for the range of y values tested. It rapidly worsens with decreasing values of x, however, especially for small values of y. In fact, within Region II the 6-point rule gives fractional errors of up to 10% for $y = .006$ and practically 100% (e.g., completely wrong results) for values of .001 and less. It is conceivable that this fact was overlooked in the original formulation because of the presumed unimportance of the wings for small y-values. However, many strong infrared bands contain lines for which y is less than .001 at altitudes for which self-absorption is very important. The need to accurately compute the wing contributions therefore made it necessary for us to modify the Pierluissi algorithm before using it.

3.5 Tests for Accuracy and Speed

In order to test different Voigt-function algorithms, we wrote a program to do a brute-force integration of Eq. (4) to serve as a benchmark, and chose a range of parameters within which to evaluate the functions. The ranges are $.000001 \leq y \leq 10$ and $0 \leq x \leq 30$.

All tests were performed on a CYBER 750 machine running under the NOS operating system.

Figure 26 gives, as a function of altitude, an approximate range of values of the parameter y which are encountered when emission in two of the strongest CO_2 bands is calculated. That is, for example, for a given altitude any line in the various ν_2 bands will be characterized by a Lorentz to Doppler linewidth ratio falling between the two top curves in Figure 26. From this and the viewing path one can readily determine the range of y -values for which the Voigt profile will need to be evaluated for any particular run. We use the U.S. Standard Atmosphere 1976 <10> for our pressure-versus-altitude profile.

We made some test runs with NLTE with the CO_2 ν_2 fundamental band at $15\mu\text{m}$ in limb geometry and counted the number of calls to the Voigt function according to ranges of values of x and y . The purpose of this exercise was to make it possible to optimize our algorithm for speed in the regions of the x - y plane encountered most frequently in typical runs. Table 4 gives the percentages of calls in different regions for a run in which paths with tangent heights of 70, 80, 90, and 100 km were done simultaneously. Table 5 gives the percentage of calls within different ranges of the parameter x alone, for jobs in which single paths with tangent heights between 50 and 100 km were run. In all cases, the atmosphere was divided into one-kilometer layers between the tangent point and an altitude of 150 km. For each viewing path, lines for which the analytic "thin-line" approximation is correct to 1% or better were disregarded in these tests.

The results in Tables 4 and 5 are predictable in several respects, notably that the lower viewing paths require a great many calls in the region $x > 5$. This occurs because of the very slow dropoff of the Voigt function in the far wings:

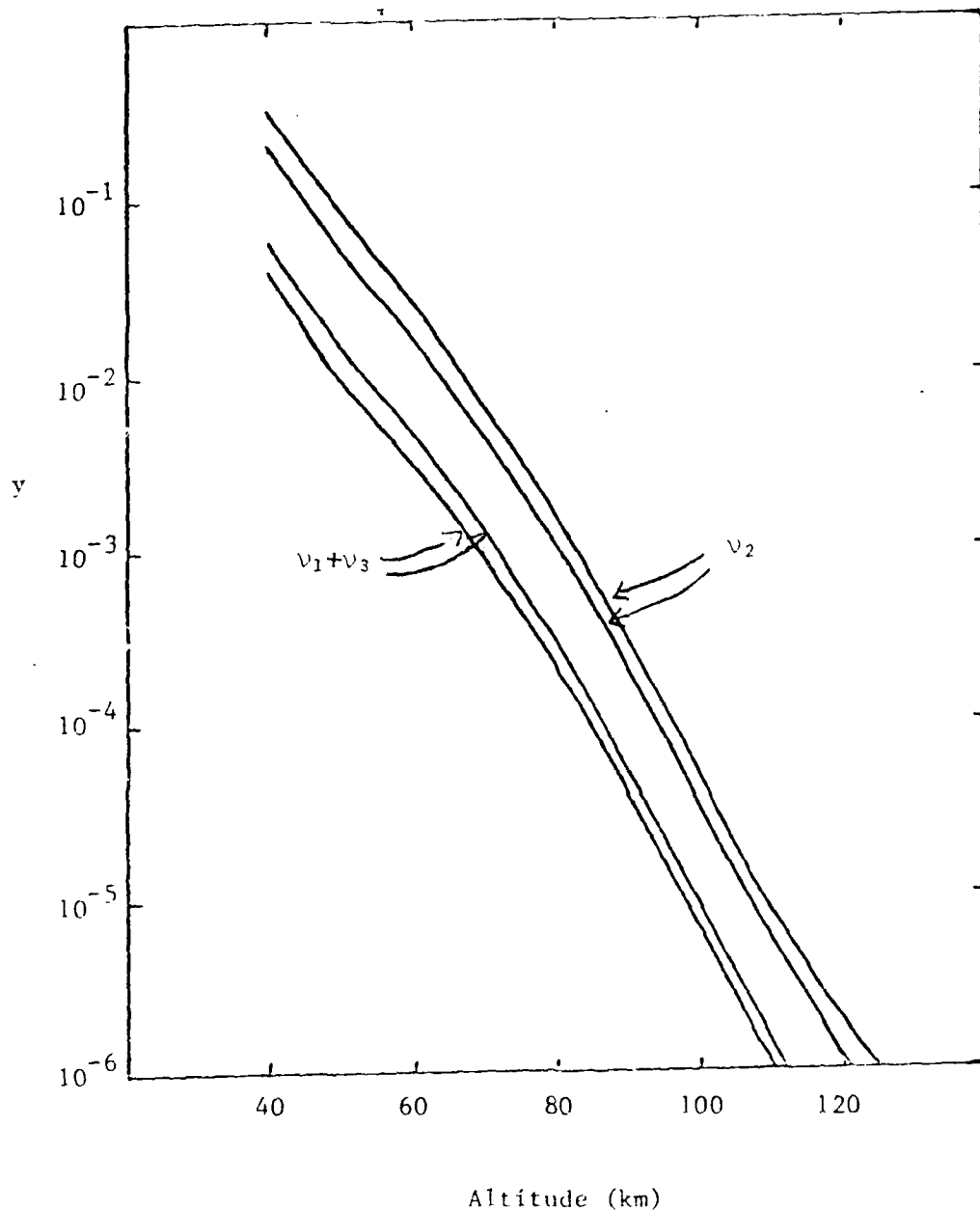


Figure 26. Minimum and maximum values of the Voigt parameter, y , as a function of altitude, for the lines in the CO_2 v_2 bands near $15\mu\text{m}$ and for the lines in the CO_2 v_1+v_3 bands near $2.7\mu\text{m}$. Values for the CO_2 v_3 bands, not shown, are slightly greater than those of the v_1+v_3 bands.

		Percentage			
		0-1.67	1.67-3.33	3.33-5.00	>5
y	x				
	$10^{-3} - 10^{-2}$	4.8	3.6	2.6	4.9
	$10^{-4} - 10^{-3}$	4.8	3.7	2.6	5.4
	$10^{-5} - 10^{-4}$	4.9	3.7	2.6	5.0
	$10^{-6} - 10^{-5}$	7.3	5.2	3.1	4.7
	$0 - 10^{-6}$	14.2	8.2	4.1	4.6
Total		36.0	24.4	15.0	24.6

Table #4 Percentage of calls to the Voigt function for different ranges of x and y, for a run using the ν_2 fundamental of CO_2 in limb geometry. Paths with tangent heights of 70, 80, 90, and 100 km. were evaluated simultaneously. The total number of calls was 286,000.

		Percentage				N
		0-1.67	1.67-3.33	3.33-5.00	>5	
h_T (km)	x					
	50	16.8	13.0	10.7	59.5	889,700
	60	20.9	15.2	11.5	52.4	596,970
	70	43.1	28.2	14.8	13.9	239,760
	80	61.6	31.3	7.1	0	136,150
	90	67.5	27.9	4.6	0	102,540
	100	72.7	24.7	2.6	0	77,250

Table #5 Percentage of calls, and total number (N) of calls, to the Voigt function for four ranges of x, for runs using the ν_2 fundamental of CO_2 in limb geometry and different tangent heights, h_T .

for the very thick lines the optical depth as far out as 25 Doppler widths may be greater than unity even with y -values on the order of 10^{-2} . Conversely, for higher paths the contributions in the far wings are much less significant and the program can cut off the numerical integration much closer to the line center. These results suggest that the design of an algorithm for use in a multitude of such applications should allow for fast execution both near the line center and in the far wings, perhaps at the expense of speed in the region $2 < x < 5$.

We tested many Voigt algorithms for accuracy. These included the three separate procedures embodied in ZVOIGT <7>, a 2-point Gauss-Hermite quadrature formula <11>, and the substitution of a simple Doppler profile. None of these provides an acceptable representation of the Voigt profile over the entire plane, or even over as much of it as Rybicki's sampling representation does in VWERF. In the end we pieced together several procedures satisfying the criterion that the Voigt profile be calculated with a fractional error less than 10^{-3} for $0 \leq x \leq 1.2$ and less than 5×10^{-3} for $x > 1.2$.

The Gauss-Hermite formulas are very fast. They are accurate for large x (more or less independent of y) and also for large y . For a given parameter set (x, y) the 6-point rule is of course more accurate than the 4- or 2-point rules. Figures 27-29 show the regions of the x - y plane where these procedures produce values more accurate than a certain threshold value, F . We have considered fractional errors of 10^{-4} , 10^{-3} , and 5×10^{-3} for F . (Actually, the true boundaries are not nearly so smooth as we have drawn them in these figures. Because the quadrature formulas are polynomial fits to the Voigt function, there are pockets and islands in the x - y plane to the left of the boundaries within which the function is also represented accurately. The accuracy criteria are satisfied, however, everywhere to the right of, and above, these curves.)

Not surprisingly, the Doppler profile $D(v)$ is a useful substitution for $V(v)$ for small values of x and y . Figure 30 gives the "regions of validity" for this substitution for the same three threshold values.

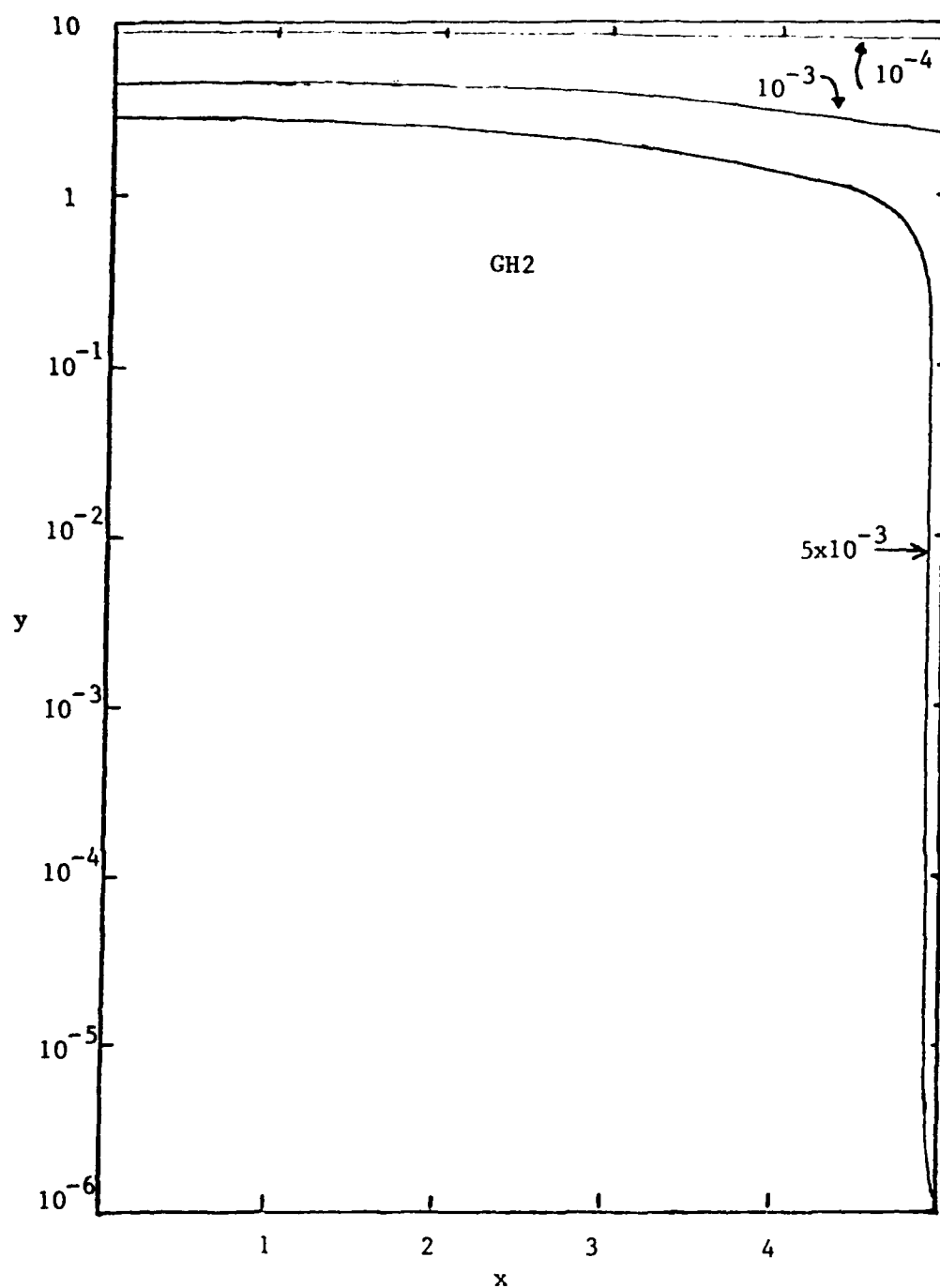


Figure 27. Regions of the x - y plane, within which a 2-point Gauss-Hermite quadrature routine approximates the Voigt function with a fractional error less than F , lie above and to the right of the three curves shown. The curves correspond to $F = 10^{-4}$, 10^{-3} , and 5×10^{-3} .

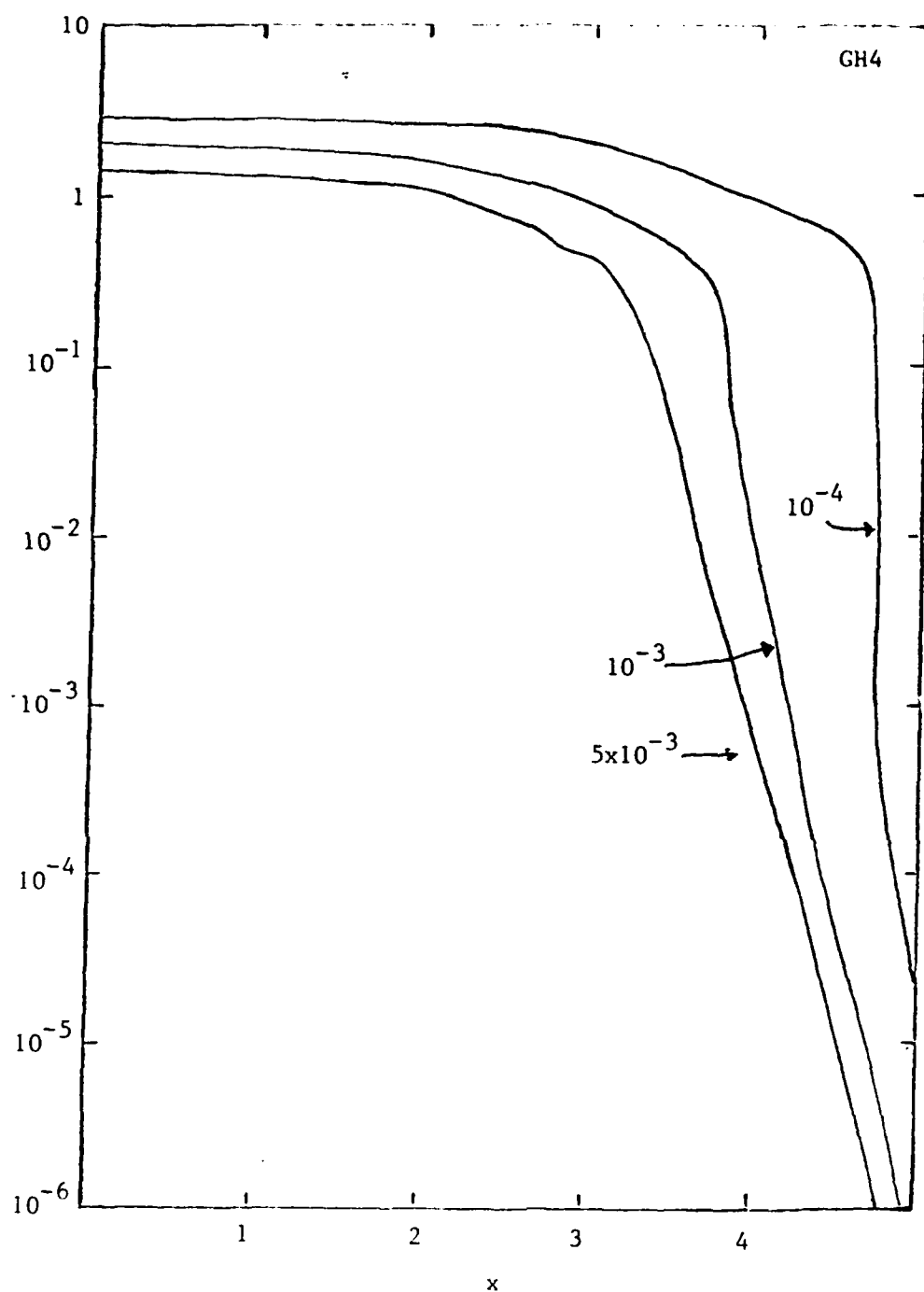


Figure 28. Regions of the x-y plane, within which a 4-point Gauss-Hermite quadrature routine approximates the Voigt function with a fractional error less than F , lie above and to the right of the three curves shown. The curves correspond to $F = 10^{-4}$, 10^{-3} , and 5×10^{-3} .

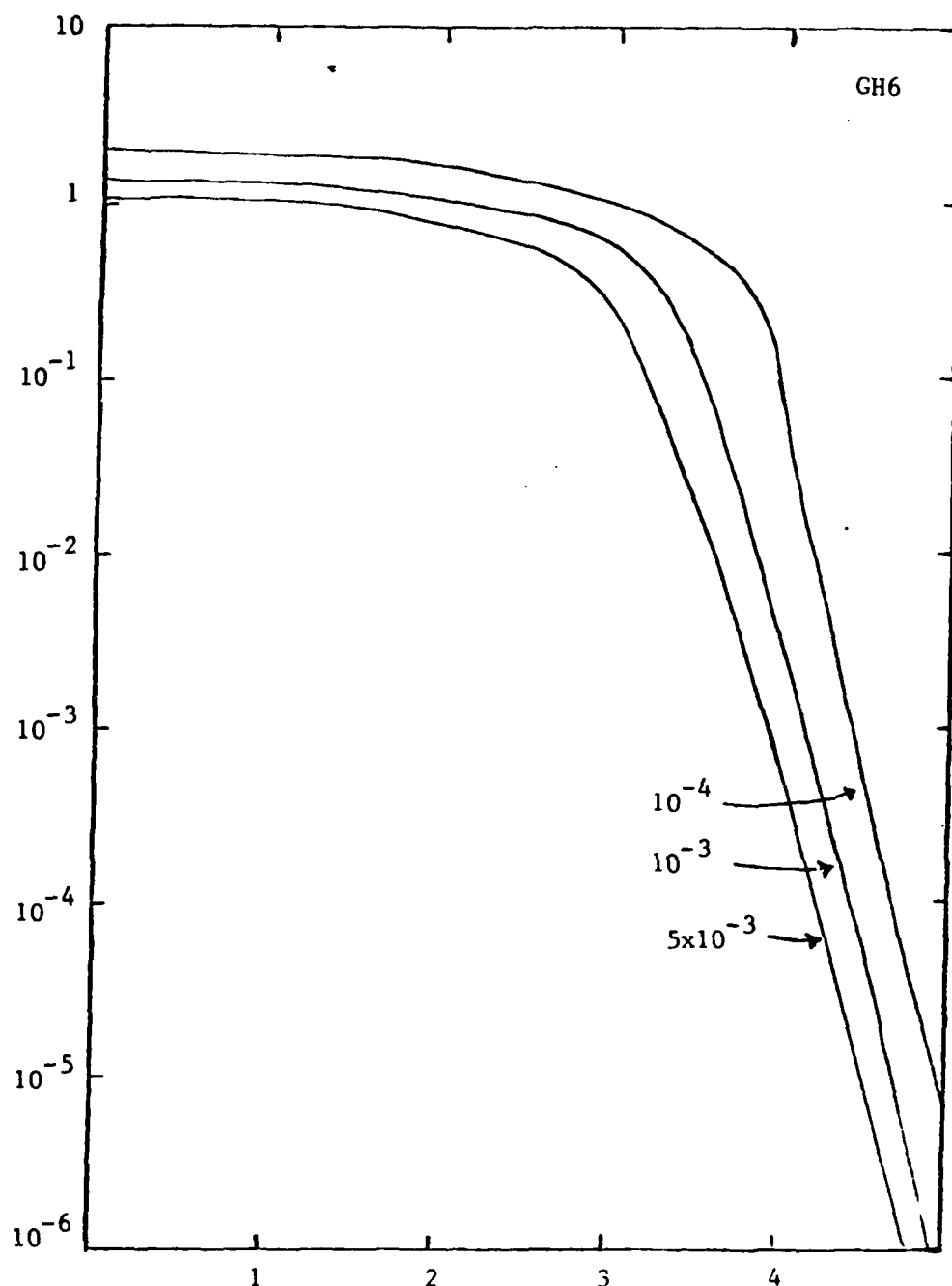


Figure 29. Regions of the x-y plane, within which a 6-point Gauss-Hermite quadrature routine approximates the Voigt function with a fractional error less than F , lie above and to the right of the three curves shown. The curves correspond to $F = 10^{-4}$, 10^{-3} , and 5×10^{-3} .

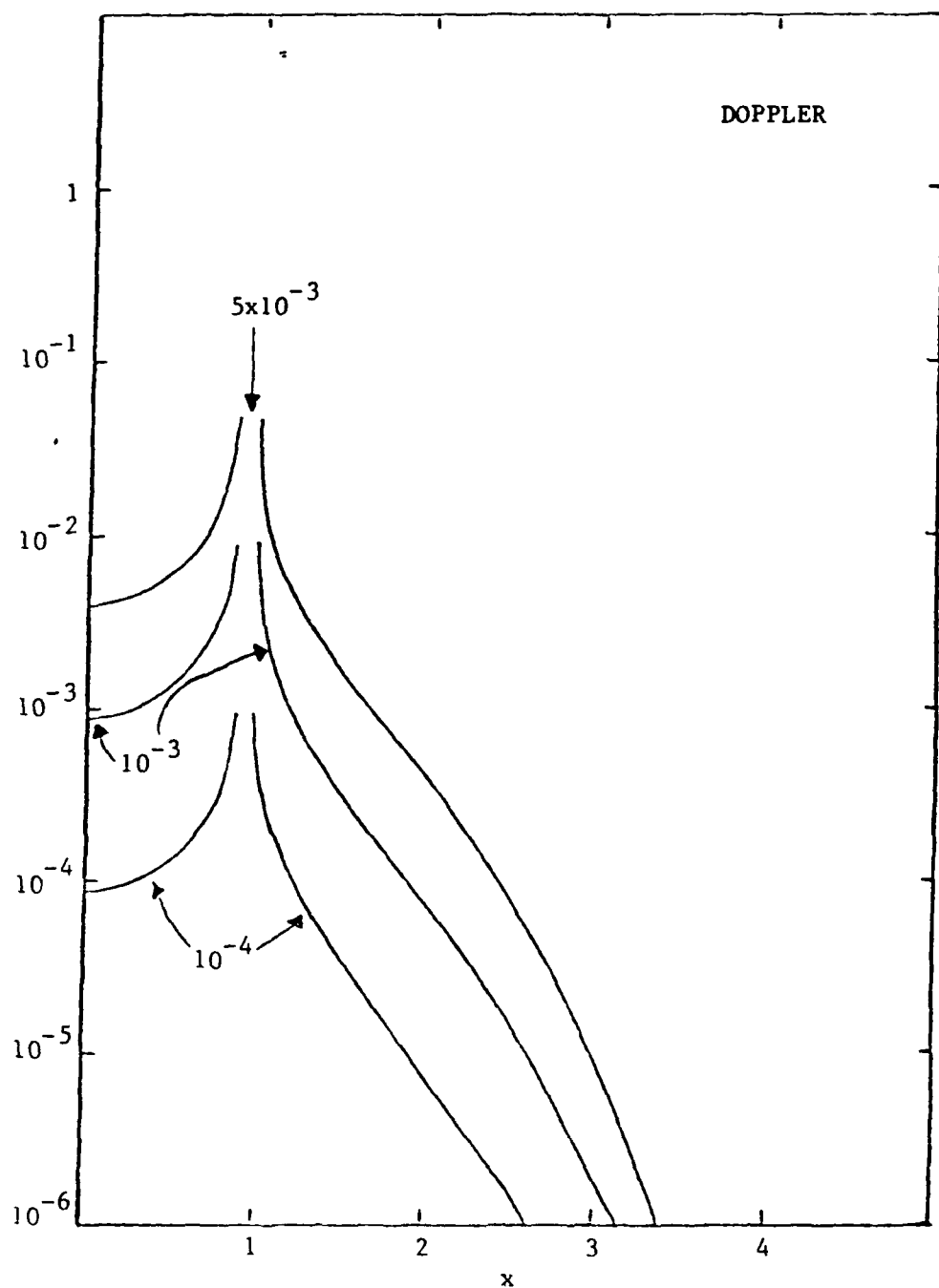


Figure 30. Regions of the x - y plane, within which the Doppler profile can be substituted for the Voigt function with a fractional error less than F , lie below and to the left of the three curves shown. The curves correspond to $F = 10^{-4}$, 10^{-3} , and 5×10^{-3} .

The ZVOIGT series used in Pierluissi's region I is, as noted above, very accurate for small x . Its accuracy deteriorates rapidly with increasing x , and it is not good enough for the series to be used at all for $y > 2$. In order to extend its useful range into the region ($x > 3$, $y \leq 0.01$) we carried it out to a maximum of 55 terms and chose a linear function of x to determine the number of terms to be taken which is somewhat different from Pierluissi's. With its three evaluations of transcendental functions and a multitude of arithmetic operations, this procedure is slower than the others mentioned above.

Table 6 gives the average execution time for six FORTRAN routines used to compute $V(v)$ on the CYBER 750. The routines were compiled in the fast-execute mode (OPT=2 on FTN5). GH2, GH4, and GH6 are the Gauss-Hermite routines. DOPP evaluates the Gaussian function, $D(v)$. SERIES is the ZVOIGT series, modified as described above. It is the only one of these whose execution time depends on the parameters, as the series has fewer terms when x is small. VWERF is Rybicki's algorithm.

In each case cited above the only overhead operations are the single call and return. That is, in the timing tests there were no branching operations or extra arithmetic. Table 6 shows, with the entries DUMMY and GO TO, respectively, the approximate time for the call and return, and the approximate extra time used by a conditional GO TO statement. Also, a real transcendental function takes approximately 10 microseconds to execute within any procedure.

3.6 Function ZVGT

Our Voigt algorithm, realized as function ZVGT, is a combination of four separate procedures: the 2- and 6-point Gauss-Hermite formulas, the Doppler substitution, and the extended ZVOIGT series. Figure 31 indicates the particular division of the x - y plane we use in this procedure. The division is implemented by several conditional GO TO statements. One may note that the Doppler and GH6 regions could be expanded into portions of the region where the slower series operates. The cost of doing this, however, is in each case the evaluation of a logarithmic or exponential function before effecting the conditional branches.

Procedure	Time (μ sec)
GH2	13
GH4	15
GH6	17
DOPP	19
SERIES	97
VWERF	230
DUMMY	9
GO TO	2.5
TRANSC	10

Table #6 Average execution times, in microseconds, for various FORTRAN procedures and operations on the CYBER 750. See text for a full explanation.

<div style="display: flex; align-items: center;"> <div style="writing-mode: vertical-rl; transform: rotate(180deg);">y</div> <div style="writing-mode: vertical-rl; transform: rotate(180deg);">x</div> </div>		Average Execution Time (μ sec), ZVGT			
		0-1.67	1.67-3.33	3.33-5.00	>5
1.5	- 10	21	21	21	15
.1	- 1.5	70	98	123	16
10^{-2}	- 10^{-1}	71	94	121	15
10^{-3}	- 10^{-2}	70	97	122	15
10^{-4}	- 10^{-3}	23	92	120	16
10^{-5}	- 10^{-4}	23	94	122	15
10^{-6}	- 10^{-5}	23	93	122	16
0	- 10^{-6}	23	23	23	15

Table #7 Average execution times (μ sec) for function ZVGT for different regions of the x-y plane.

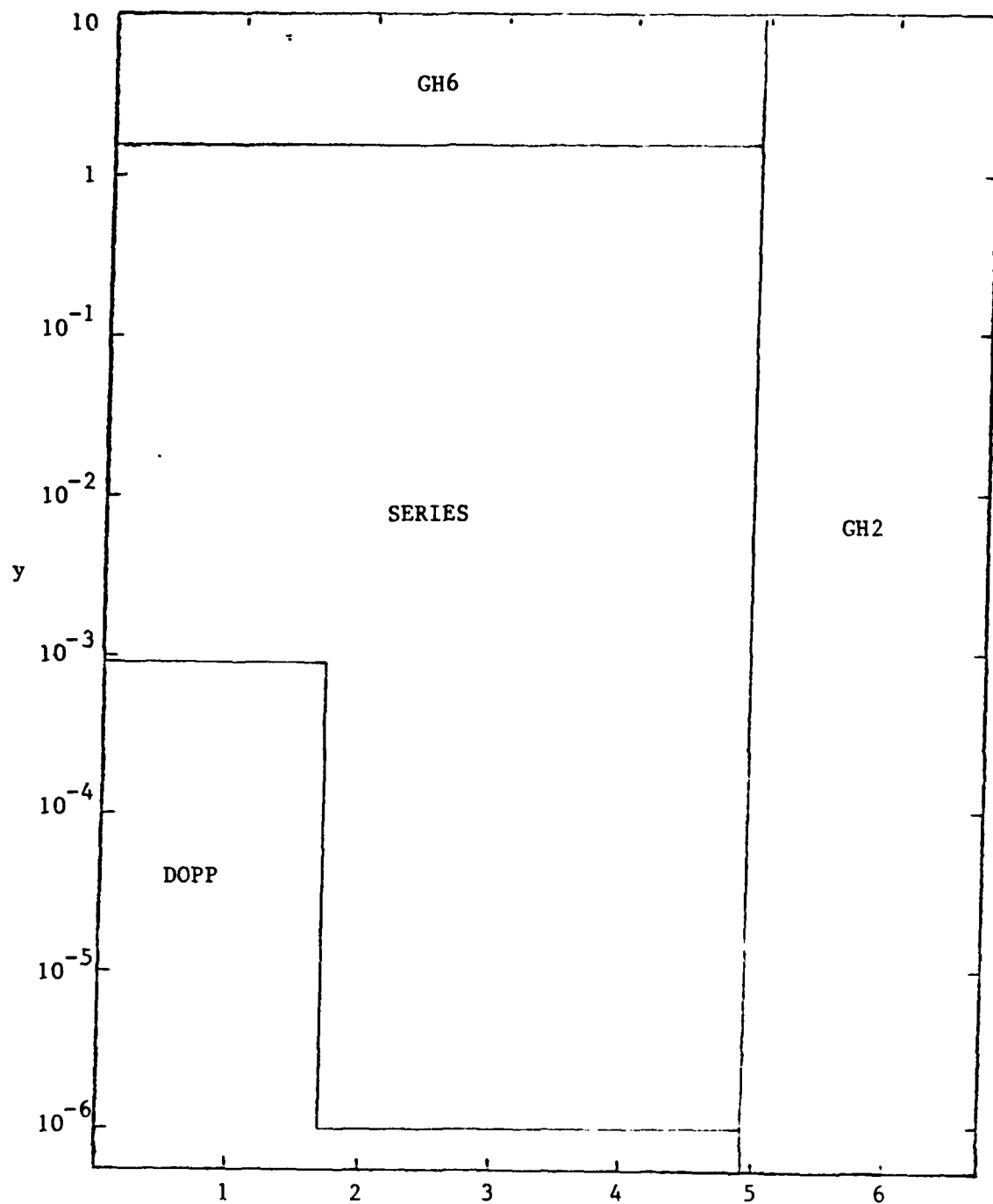


Figure 31. Partition of the x-y plan into regions for function ZVGT. 2-point Gauss-Hermite quadrature is used for $x > 4.9$. The 6-point rule is used for $(y > 1.5, x < 4.9)$. The Doppler function is used for $(x < 1.7, y < .0009)$ and for $(y < 10^{-6}, x < 4.9)$.

The extra time required for these functions is greater, in a typical run with parameters distributed as in Table 4, than the time saved by implementing the faster arithmetic.

As noted above, ZVGT calculates $V(v)$ with a fractional error of less than 10^{-3} for $x \leq 1.2$ and 5×10^{-3} for $x > 1.2$. That is, the function is accurate to at least .1% in the line center and .5% elsewhere. In fact, these limits are approached only at the boundaries of the sections. Over most of the x-y plane the routine is much more accurate than this, especially for small x.

Table 7 gives the average execution time required by a single call and return to function ZVGT for different regions of the x-y plane. For the distribution of calls given in Table 4, the average execution time is about 46 μ sec. For the distribution of calls required for tangent heights between 50 and 100 km, the average execution time ranges between 36 and 49 μ sec using ZVGT. Because of the emphasis on very large x, where the routine is very fast, the lower tangent paths require a smaller average time; of course, they also require a larger number of calls.

We note that by calculating a large array of values at one time rather than calling the routine for each sepeate evaluation, an additional 9 μ sec could be saved, per average evaluation.

The source listing of ZVGT is given in Appendix A.

4. NUMERICAL INTEGRATION ALGORITHM

4.1 General Description

NLTE computes the band radiance, in watt/cm²-ster, by performing a numerical integration over the spectral radiance profile computed for each line, and then summing over the lines in the band. In the first release, the numerical integration procedure was awkward to use because it was necessary to specify both a frequency interval sufficiently small for the compounded Simpson's rule to be accurate, and also a number of integration points sufficiently large to avoid a significant truncation error in the far wing of the strongest lines. This inevitably led to unnecessary work in the wings of weak lines.

We have replaced the original integration algorithm with a new procedure which avoids these input requirements and also is more efficient for three reasons. First, it uses Gauss-Legendre integration formulas, which are inherently more accurate than Simpson's rule, given a certain number of points in a fixed interval. This allows us to use fewer points throughout the profile. Second, it is sensitive to the characteristics of individual lines rather than to those of an entire band, so it cuts off the calculation at distances from the line center which are correct for both strong lines and weak lines. Moreover, it recognizes that numerical integration in the far wings of the radiance profile, where the integrand decreases monotonically and quite slowly, can be carried out with fewer points per frequency interval than it can nearer the center where the function may have a non-central maximum and in any event varies more rapidly. This allows us to use still fewer points per frequency interval in the wings. Third, we use an analytical approximation to evaluate the integrated contribution of the far tail of the radiance profile, thereby eliminating the truncation error and allowing the numerical evaluation to be cut off closer to the line center.

On the whole, these three changes have succeeded in reducing the number of function evaluations, and hence the run time, by a considerable amount. They are discussed, one by one, in the following sections. Some of the work described below relies heavily on analysis first presented by Bullitt et al <12>.

4.2 Integration Rule

We use Gauss-Legendre formulas for our numerical integration in NLTE because of their high accuracy <8>. Two-, four-, or eight-point rules can be specified. Built-in flexibility is provided because the program divides the frequency range into successive "panels", or intervals, within which it applies the Gauss formula. The first panel comprises the interval from the line center out to one "standard Doppler width". For all paths, the integrated radiance in this interval is determined before the second panel is considered. The second panel comprises the

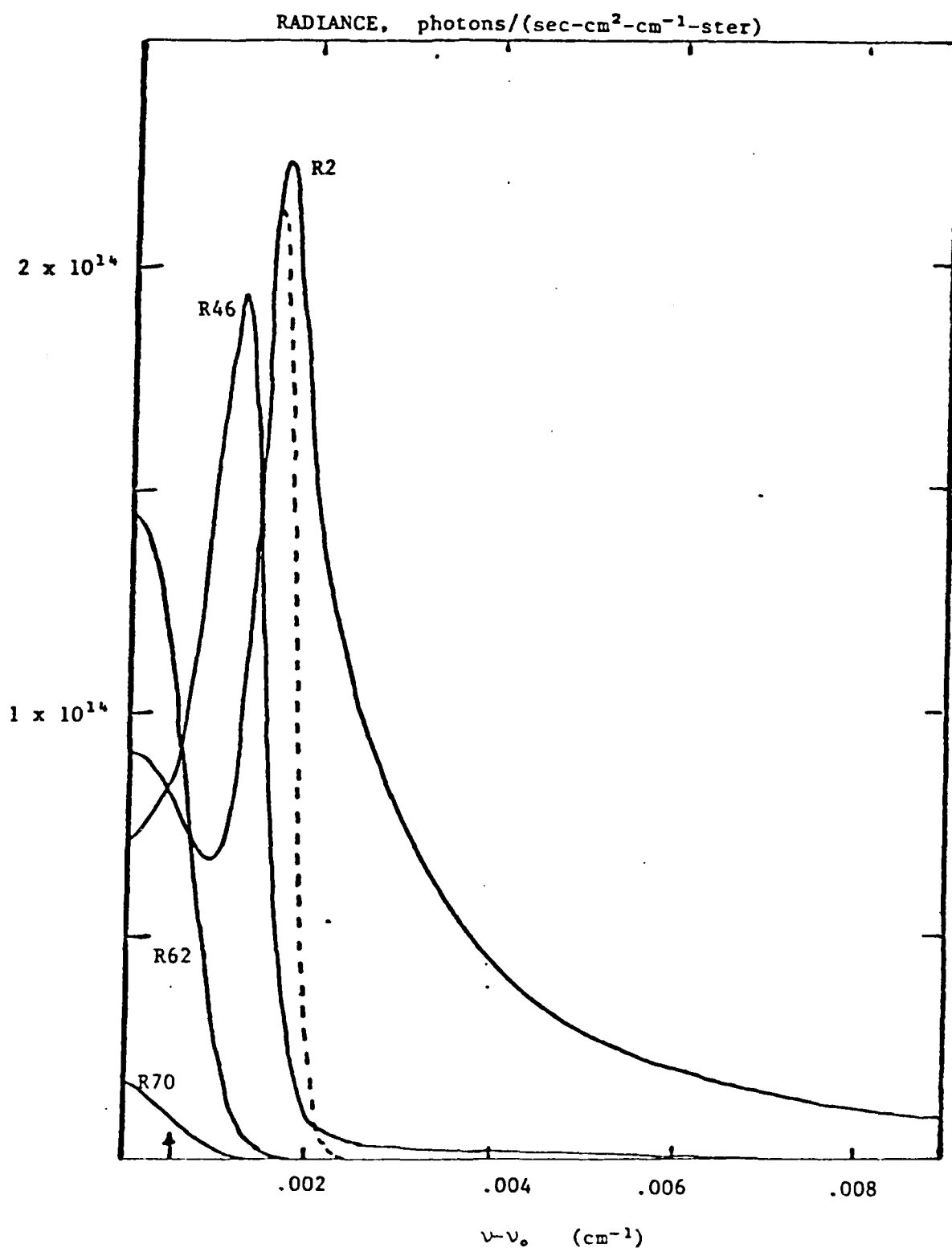


Fig. 32. Radiance profiles of 4 lines of the R branch of the $\text{CO}_2(\nu_2)$ fundamental near 667 cm^{-1} . The curves, which were calculated by program NLTE were plotted for limb-look geometry for a tangent-height of 70 km . The solid lines were found assuming a Voigt lineshape. The dotted line is the R2 profile assuming a Doppler lineshape. The arrow at the bottom indicates the Doppler linewidth at the tangent-height.

frequency interval between one and two "standard Doppler widths", and so on. This gives us an accumulating total for the integrated intensity of the line as we proceed, which is useful for evaluating the cutoff criterion in the wing.

A "standard Doppler width" is defined as a Doppler width determined by using the band center for the frequency and the lowest temperature in the altitude range under consideration for the kinetic temperature.

We have found that the default value of four points per panel is sufficient for very accurate results. Use of two points per Doppler width often gives errors in the band radiance which are less than errors introduced by other approximations built into the program.

4.3 Adjustments for Different Lines

Figure 32 illustrates the great differences which characterize radiance profiles of different lines within the same band, provided some of the lines are self-absorbed along the viewing path. The weakest lines mimic Doppler lines; stronger lines decrease monotonically from the center but have much more pronounced wings; and, for typical temperature profiles, the strongest lines have maxima and possibly minima away from the line center, as well as wings where the function decreases smoothly and monotonically but very slowly over a large range of frequencies.

As mentioned above, four points per Doppler width usually give accurate results for the numerical integration over the whole profile. Since the regions where the integrand varies most rapidly, which in general are the central region and wherever else extrema occur, are the most difficult to integrate accurately, it stands to reason that the regions where the integrand is smoothest require fewer points than this. In our case, the wings of the radiance profile can be integrated very efficiently by expanding the panel width and using the same number of points per panel as near the line center. Of course, it is necessary to be able to specify the frequency, beyond which the radiance profile is smooth enough to expand the panels, on a line-by-line basis.

Bullitt et al <12> have shown that the radiance profile can be represented as the product of two quantities. The first is the absorptivity, $(1 - \exp(-\tau_\nu))$, where τ_ν is the optical depth along the line-of-sight path at frequency ν . The second is $\langle R \rangle / \langle R_\infty \rangle$, where $\langle R \rangle$ is an effective blackbody radiance averaged over the path with a certain weighting function <12>, and $\langle R_\infty \rangle$ is its limiting value in the far wing.

The second of these two factors smoothly approaches unity in the wings, so the functional dependence of the radiance profile there is essentially that of the absorptivity. In fact, for $\tau_\nu \ll 1$, one sees by expanding the exponential that the frequency-dependence is entirely contained in τ_ν , which is proportional to $V(\nu)$.

On the other hand, if $\tau_\nu \gg 1$ in the line center, the absorptivity is nearly constant (and nearly unity) so the functional dependence of the radiance profile is basically that of the second factor. This second factor, being akin to a blackbody radiance, is influenced by the temperature along the path and is thereby responsible for maxima and minima appearing near the center of the profile if $\tau_\nu \gg 1$. That is, the observer "sees" emission from portions of the path only a certain distance into the atmosphere because of self-absorption, and the amount of radiation reaching him depends on the temperature along those portions. Since the portions "seen" depend on frequency through the optical depth, the radiance profile may have extrema if the temperature profile varies rapidly.

The considerations introduced in the last two paragraphs, which are illustrated quite effectively in Figure 9 of Reference 12, imply that beyond the frequency at which the absorptivity departs significantly from its value at ν_0 , there will be no extrema in the radiance profile. That is, for all frequencies greater than some ν such that $\tau_\nu \ll 1$, the observer will "see" the entire path and the frequency-dependence of $\langle R \rangle / \langle R_\infty \rangle$ will be slight; however, this is exactly the range in which the monotonic decrease in the absorptivity begins to dominate the function. For these reasons the program uses $\tau_\nu = 1.5$ as a flag for the frequency beyond which the functional dependence of the radiance profile is sufficiently slowly-varying to expand the panel width. This is actually a

fairly conservative benchmark; we find that the outermost peak in typical thick-line radiance profiles comes between $\tau_v \sim 2$ and $\tau_v \sim 5$.

The rule for expanding the panel width was established by trial and error. We double the panel width for each panel occurring past the aforementioned "flag". This obviously carries the numerical integration into the far wings very rapidly. The reason it works as well as it does can be seen in the error term for four-point Gauss-Legendre quadrature, which for a fixed interval size goes as the eighth derivative of the integrand at some point in the integration interval. For the wings, as we pointed out earlier, the integrand goes as $V(v)$, which is very nearly proportional to the Lorentzian $L(v)$ there. The eighth derivative of $L(v)$ is proportional to $(v-v_0)^{-10}$. With such a rapidly decreasing error for fixed intervals, one can see how the intervals can be expanded rapidly as $(v-v_0)$ increases without compromising the accuracy of the calculation.

Weak lines with $\tau_v \ll 1$ at the line center can be evaluated by the "thin-line" approximation which neglects absorption along the viewing path. When $\tau_v \lesssim 5$ and the thin-line approximation is not used the panel widths are not doubled until the fourth panel is reached. Usually the truncation procedure is invoked quite quickly for such lines, anyway.

4.4 Truncation Procedure

The third component of our revised procedure for integrating the radiance profile is a cutoff of the numerical evaluation. The radiance profile is of course originally written as an integral over the viewing path $\langle 12 \rangle$. If s'' parameterizes the path and s and s' are its near and far ends, respectively, the radiance is $\langle 4, 12 \rangle$

$$I_v(s) = \frac{A}{4\pi} \int_{s'}^s n_u(s'') V_v(s'') \exp(-\tau_v(s, s'')) ds'' \quad (7)$$

where A is the Einstein coefficient for spontaneous emission, n_u is the number density of the upper radiating state in molecules/cm³, and the path-dependence

of the Voigt profile has been made explicit. At the path's end, the integrated radiance in the tail, that is in the region $v_c \leq |v - v_0| < \infty$ is

$$T(v_c, s) = 2 \int_{v_c}^{\infty} I_v(s) dv \quad (8)$$

which, with $\tau_v \ll 1$, can be written as

$$T(v_c, s) = \frac{A}{2\pi} \int_{s'}^s n_u(s'') \left[\int_{v_c}^{\infty} V_v(s'') dv \right] ds'' \quad (9)$$

Using any of several representations of the tail of the Voigt function, one can show that the v -integral is equal to $\frac{y}{\pi x} = \frac{\alpha_L}{\pi(v - v_c)}$ to order $(y/x_c)^3$ where y and x are the Voigt parameters of Eqs. (3) and x_c is x evaluated at $v = v_c$. This quantity is of course altitude-dependent through the Lorentz width, α_L , and must be integrated over s'' . In NLTE, the s'' integral is just a sum over homogeneous layers, however, and is done on the initial pass through the atmosphere as the thin-line approximation is evaluated for each path. Given this, it is easy to calculate $T(v_c, s)$ for any given v_c for all the paths.

The difficult part is determining how accurate the truncation term is. Our procedure for determining where to cut off the numerical integration and invoke the truncation approximation is based on empirical tests and is likely to be refined in the future. At present we evaluate the truncation term at the end of each panel past the third one and compare it with the quantity α , defined as

$$\alpha = \frac{6\epsilon I_c}{\tau_{v_c}}$$

where I_c is the cumulative integrated radiance in the panels treated so far, τ_{v_c} is the optical depth for the path at the end of the last panel, and ϵ is the desired accuracy of the integrated radiance in the line, expressed as a fractional error. If α is greater than $T(v_c, s)$, the expression for the tail is presumed to be valid and the numerical evaluation of the radiance profile is cut off.

5. REFERENCES

1. R. A. McClatchey, W. S. Benedict, S. A. Clough, D. E. Burch, R. F. Calfee, K. Fox, L. S. Rothman, and J. S. Garing, "AFCRL Atmospheric Absorption Line Parameters Compilation," AFCRL-TR-73-0096 (1973), NTIS #AD762904.
2. L. S. Rothman, R. R. Gamache, A. Barbe, A. Goldman, J. R. Gillis, L. R. Brown, R. A. Toth, J. M. Flaud, and C. Camy-Payret, "AFGL Atmospheric Absorption Line Parameters Compilation: 1982 Edition," App. Opt. 22, 2247 (1983).
3. L. S. Rothman, A. Goldman, J. R. Gillis, R. R. Gamache, H. M. Pickett, R. L. Poynter, N. Husson and A. Chedin, "AFGL Trace Gas Compilation: 1982 Version," App. Opt. 22, 1616 (1983).
4. R. D. Sharma, R. Siani, M. Bullitt, and P. P. Wintersteiner, "A Computer Code to Calculate Emission and Transmission of Infrared Radiation through a Non-Equilibrium Atmosphere," AFGL-TR-83-0168 (1983), NTIS #ADA137162.
5. M. Abramowitz and I. A. Stegun, eds., Handbook of Mathematical Functions with Formulas, Graphs, and Mathematical Tables, N.B.S. Applied Math. Series, U.S. Government Printing Office, Washington, 1964, pp. 297-302.
6. A Method due to Rybicki, described in B. H. Armstrong and R. W. Nichols, Emission, Absorption and Transfer of Radiation in Heated Atmospheres, Pergamon, N.Y., 1972.
7. J. H. Pierluissi, P. C. Vanderwood, and R. B. Gomez, "Fast Computational Algorithm for the Voigt Profile," J. Quant. Spectrosc. Radiat. Transfer, 18, 555 (1977).
8. F. B. Hildebrand, Introduction to Numerical Analysis, McGraw-Hill, N.Y., 2nd ed., 1974.
9. Reference 5, p. 924.
10. Committee on Extension to the Standard Atmosphere, (M. Dubin, A. R. Hull, and K. S. W. Champion, co-chairmen), U.S. Standard Atmosphere, 1976, NOAA-S/T 76-1562, U.S. Gov. Printing Office, 1976.
11. J. E. Kalshoven, Jr. and H. Walden, "Laser Bandwidth and Frequency Stability Effects on Remote Sensing of Atmospheric Pressure as Applied to a Horizontal Path Measurement", topical meeting on Optical Techniques for Remote Probing of the Atmosphere, Incline Village, NV, Jan. 11-12, 1983.
12. M. K. Bullitt, P. M. Bakshi, R. H. Picard, and R. D. Sharma, "Numerical and Analytical Study of High-Resolution Limb Spectral Radiance from Non-Equilibrium Atmospheres", J. Quant. Spectr. Rad. Transfer (to be published, 1985).

IV. ATMOSPHERIC AURORAL RADIANCE CODE

1. INTRODUCTION

Over the past several months, much effort has been devoted to the construction of the computer program, AARC, whose overall purpose is the calculation of infrared emissions from nitric oxide excited by energetic auroral electrons and background earthshine radiation.

Many of the procedures involved in the calculation are new, while others had already existed. Several improvements and corrections were made to these pre-existing procedures, including modifications to ensure compatibility with other segments of AARC.

The calculation of nitric oxide radiance observed over a line of sight passing through various regions of the atmosphere, and possibly through a zone of auroral dosing, requires that AARC divide the line of sight into segments. For each segment, AARC calculates the altitude, temperature, atmospheric composition and the presence and intensity of auroral NO excitation. These data allow AARC to calculate for each segment the band emission rates for the NO and NO+ fundamental and overtone bands. These are then summed over all segments to obtain the band radiance at the point of observation.

AARC then distributes the band radiances to all the rotational lines which make up the band according to the emission strength of the line as determined from the A.F.G.L. Atmospheric Absorption Line Parameters Compilation <1>.

This set of line intensities and positions is then convolved with a spectrometer response function to generate the synthetic spectrum, which is output to a file in a form readable by a subsequent plotting routine.

AARC allows the user to specify all of the parameters which characterize the observation situation. These include the position of the observer and the geometry of the line of sight, the character and boundaries of the auroral dosing, and the wavelength range of the synthetic spectrum along with the nature of the spectrometer response function. The parameter input procedure has been designed to be highly user friendly by presenting the user a series of menus, allowing

the modification of any or all parameters. All parameters default to the values used in the previous run of AARC. This is accomplished by storing the values of the parameters in a data file which is updated with each run of AARC.

In addition, AARC may be run in a non-interactive mode which does not poll the user for input. In this mode, the user may specify input parameters by making modifications to the data file holding the defaults for the input parameters.

A complete report describing the first release of AARC, and showing exactly what forms are required for the input data, is being prepared with the help of ARCON personnel, and will be released early in 1985. The following sections provide a functional outline of the sections of the code which have been developed or substantially modified by ARCON personnel.

2. CALCULATION OF ELECTRON-ION PAIR PRODUCTION PROFILE

The calculation of the volume emission rate along the line of sight requires AARC to first calculate the rate of electron energy deposition as a function of altitude for the electron energy distribution function specified by the user.

The energy distribution function of the electron flux at the top of the atmosphere may be specified in terms of a Maxwellian distribution,

$$f(E) = A \cdot E \cdot \exp(-E/\alpha) \quad , \quad (1)$$

where $f(E)$ is the flux of electrons of energy E at the atmospheric ceiling in electrons/cm²-sec-keV, α is the characteristic energy in keV, and A is a normalization constant depending upon α and Q_m , the total energy incident on the atmosphere in ergs/cm²-sec:

$$A = \frac{Q_m}{2 \cdot 1.602 \times 10^{-9} \cdot \alpha^3} \quad . \quad (2)$$

To define this distribution, the user must specify the characteristic energy, α , and the total energy flux, Q_m .

The electron flux may also be specified via a Gaussian distribution,

$$f(E) = A \cdot E \cdot \exp \left[- \frac{(E - E_0)^2}{w} \right] \quad (2)$$

where E_0 the energy at the distribution maximum, w is the characteristic width of the distribution, and A is a normalization constant determined from the total energy flux. Here the user must specify the two constants, E_0 and w , and also the total energy flux.

The choice of Maxwellian distribution is appropriate for continuous aurora, while Gaussian distribution is more appropriate for discrete aurora.

The calculation of the corresponding energy dosing profile employs a semi-empirical method due to Rees <2>, which utilizes an experimentally determined energy dissipation function <3> shown in Figure 33. Here $\lambda\left(\frac{z}{R}\right)$ is the fractional energy dissipation, z is the air mass penetrated by the monoenergetic electron beam in gm/cm^2 , and R is the maximum range of the beam given by <3>:

$$R = 4.57 \times 10^{-6} E^{1.75}, \quad (3)$$

where E is the energy of the beam in keV. The energy dissipation function, $\lambda\left(\frac{z}{R}\right)$, is relatively insensitive to the beam energy for energies ranging from 0.4 keV to 200 keV.

The ion-pair production rate in pairs/ cm^3 -sec is given by

$$q(z) = \frac{\rho(z)}{\Delta E_{\text{ion}}} \int dE \frac{E}{R} \lambda\left[\frac{z}{R}\right] f(E), \quad (4)$$

where $\rho(z)$ is the atmospheric density in gm/cm^3 at the altitude z , and ΔE_{ion} is the energy for production of one electron-ion pair (0.035 keV/pair).

AARC employs Gaussian quadrature to integrate eq. (4) over the energy range of interest.

Alternatively, the user may choose from one of three program-defined dosing profiles appropriate for auroras of IBC classes II, III and III⁺. AARC will then

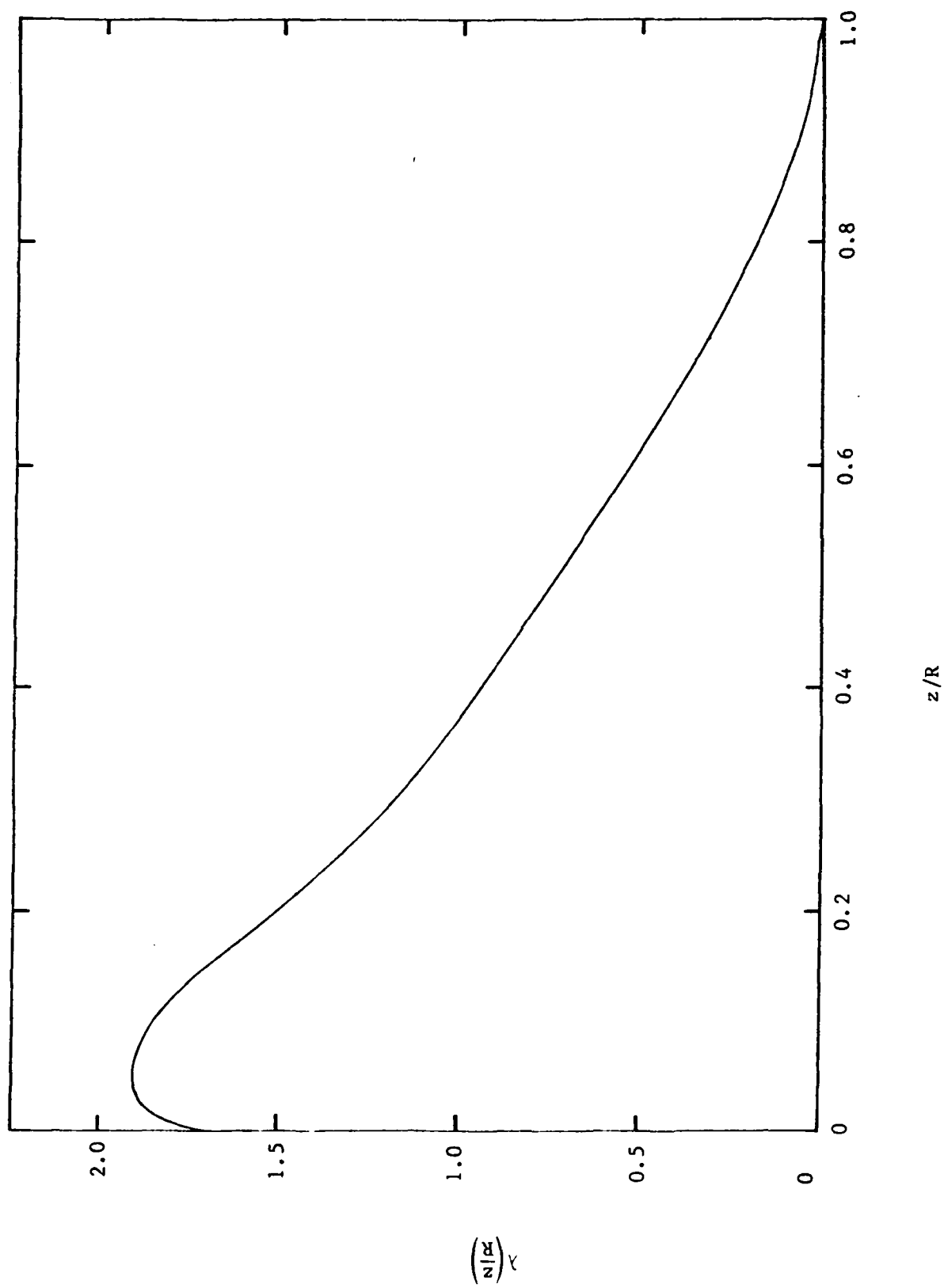


Figure 33. Normalized dissipation function

use dosing profiles stored within the program which were previously calculated using a Maxwellian distribution and parameters given in Table 8. Figure 34 shows the electron-ion pair production profile for these three distributions.

3. CALCULATION OF VOLUME EMISSION RATE

The calculation of the auroral NO infrared volume emission rate requires the solution of a set of balance equations involving the production of $N(^2D)$ and $N(^4S)$ via collision of energetic electrons with N_2 and NO^+ and the reaction of N_2^+ with O_2 and O , the production of $NO(v)$ by reaction of $N(^2D)$ and $N(^4S)$ with O_2 and emission and absorption from $NO(v+1)$ and $NO(v-1)$, and depletion of $NO(v)$ by collision with $N(^2D)$ and $N(^4S)$ and also by emission or absorption of infrared radiation.

AARC does not explicitly solve these balance equations, but instead uses a set of production efficiencies which have been previously calculated by assuming an electron-ion pair production rate, solving the balance equations for the corresponding volume emission rate, and then dividing the emission rate by pair production rate assumed. These efficiencies are used as input to AARC, where they are used to calculate band emission rates for an arbitrary dosing rate.

The calculation of the excitation of $NO(v=1)$ from the ground state via earthshine in the quiescent atmosphere is more explicit.

We assume that the earthshine excitation rate is constant over the line-of-sight and is given by:

$$R_E = 1.06 \times 10^{-4} \text{ excitations } NO(v=1) / \text{sec} \cdot \text{molecules } NO(v=0) \quad (5)$$

Relaxation of $NO(v=1)$ proceeds via atomic oxygen collision



$$k_1 = 6.5 \times 10^{-11} \quad ,$$

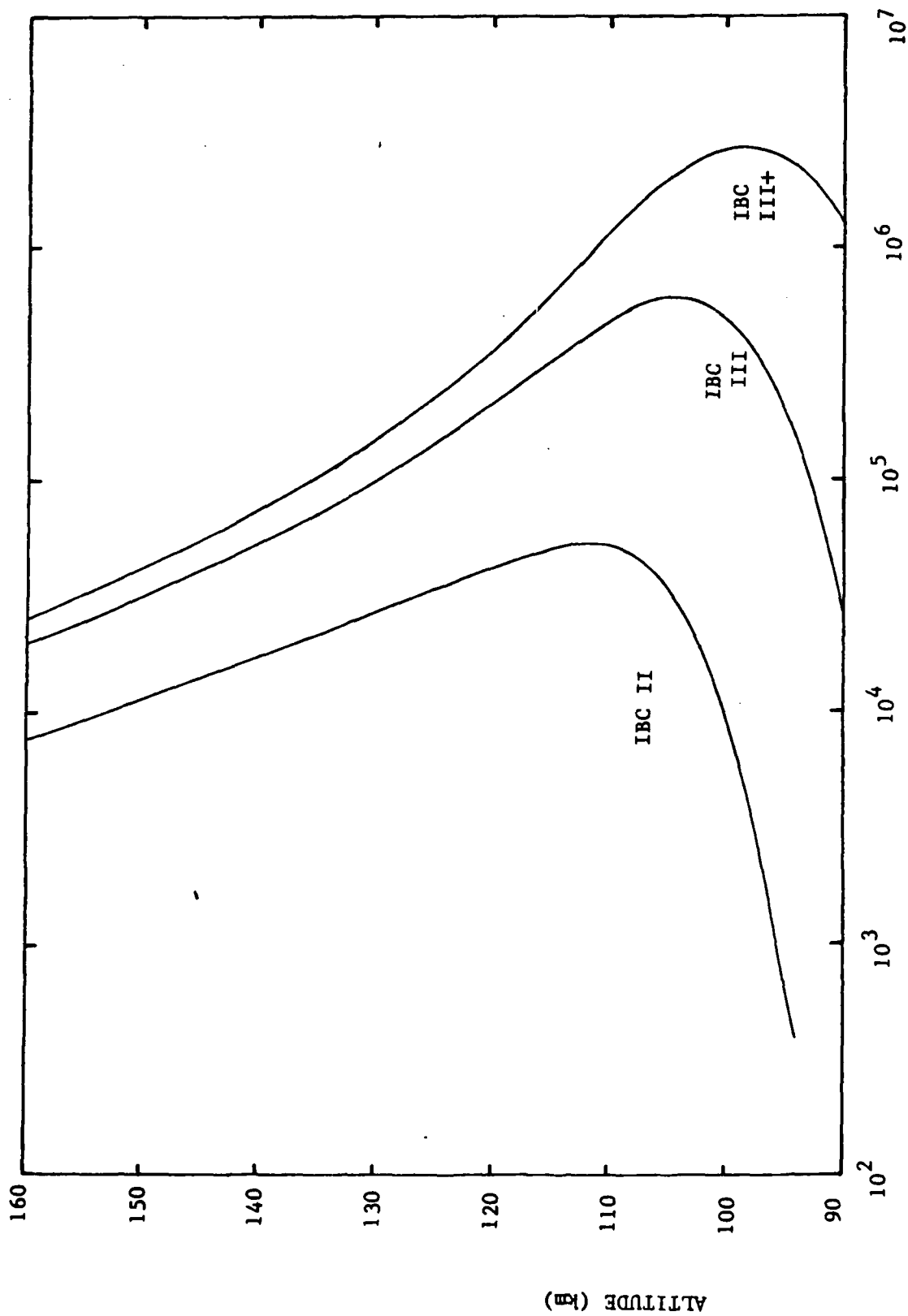
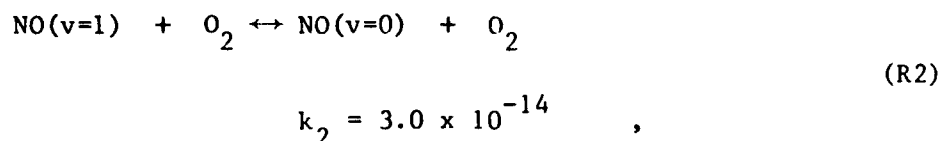


Figure 34. ELECTRON-ION PAIR PRODUCTION RATE (pairs/cm³-sec)

via collision with molecular oxygen:



and also via spontaneous emission.

Under equilibrium conditions,

$$[\text{NO}(v=1)] = \frac{R_E + k_{-1}[\text{O}] + k_{-2}[\text{O}_2]}{A_{10} + k_1[\text{O}] + k_2[\text{O}_2]} \quad , \quad (6)$$

where A_{10} is the Einstein coefficient for emission from $\text{NO}(v=1)$. The volume emission rate is, of course, just this times A_{10} .

4. CALCULATION OF RADIANCE AT THE OBSERVATION POINT

To calculate the radiance, AARC must sum the emission rate, which depends upon the composition of the atmosphere, temperature, pressure, and auroral energy deposition rate, over the entire line of sight. The line of sight passes through a range of altitudes and regions characterized by presence or absence of auroral dosing. Thus AARC must partition the line of sight into segments, and calculate the altitude for each segment so that the appropriate atmospheric parameters may be determined via linear interpolation, and also calculate the geographic location of the segment, via simple spherical geometry, so that the presence of auroral dosing may be determined. AARC compares the coordinates of the segment with the boundaries of the auroral zone, which the user may specify using either geographic or geomagnetic coordinates.

The summation of the NO infrared emissions begins at the far end of the line of sight, where it passes through the maximum altitude of interest specified by the user, continues through the tangent point to the near point, where it passes through the maximum altitude again. The boundaries of each segment are chosen so that each segment subtends the same angle at earth center. Currently, AARC is suited for limb-look geometry only.

IBC CLASS	α (kev)	Q_m (ergs/cm ² -sec)
II	2.9	12.9
III	5.0	100.0
III ⁺	10.0	400.0

Table 8 Pair production profile parameters included
in AARC for three classes of auroras.

5. GENERATION OF SYNTHETIC SPECTRUM

The summation over the line of sight produces a set of band radiances for the NO and NO+ fundamental and overtone bands up to the vibrational state $v'=15$. In addition, AARC calculates, via a weighted average over the line of sight, an effective band temperature associated with each band.

The next step is to distribute the band radiances over all ro-vibrational transitions in the bands.

The intensity of a particular line is proportional to the probability that the upper state is occupied, as calculated from the Boltzmann factor using the effective band temperature and the degeneracy of the state, and proportional to the Einstein spontaneous emission coefficient as calculated from the AFGL database <1>. The calculation of individual line intensities is subject to the constraint that the sum of all lines in a band must be equal to the total band radiance.

This calculation results in a set of line positions and intensities, which is then convolved with a triangular spectrometer function to generate a synthetic spectrum over a range of wavenumbers specified by the user.

6. REFERENCES

1. R. A. McClatchey, W. S. Benedict, S. A. Clough, D. E. Burch, R. F. Calfee, K. Fox, L. S. Rothman, and J. S. Garing, "AFCRL Atmospheric Absorption Line Parameters Compilation," AFCRL-TR-73-0096 (1973), NTIS #AD762904.
2. M. H. Rees, "Auroral Ionization and Excitation by Incident Energetic Electrons," Planet. Space Sci., 11, 1209 (1963).
3. A. E. Grun, Z. Naturf. 12a, 89 (1957) as referenced in <2>.

V. APPENDIX

The source code for function ZVGT is given in the following pages.

```

C      FUNCTION ZVGT(XX,Y)
C
C      VOIGT PROFILE ALGORITHM DESIGNED FOR FAST EXECUTION IN PROGRAM NLTE.
C      DOPPLER PROFILE IS SUBSTITUTED IN SOME REGIONS. THE METHOD EMPLOYED
C      IN REGION 1 WAS ORIGINALLY OUTLINED BY PIERLUISSI ET AL,
C      JQSRT 18,555(1977). THE ROUTINE HAS BEEN TESTED FOR 0<XX<30 AND Y=0,
C      .000001<Y<10. IT GIVES AN ACCURACY OF BETTER THAN .1% FOR XX<1.5 AND
C      BETTER THAN .5% EVERYWHERE ELSE IN THIS REGION. THAT IS, THE
C      ABSOLUTE ERROR IS LESS THAN .001 OR .005 TIMES THE CORRECT FUNCTION
C      VALUE. FOR Y<.000001, WHERE THE DOPPLER PROFILE IS SUBSTITUTED,
C      THE FRACTIONAL ERROR MAY BE GREATER FOR XX>4 BUT THE ABSOLUTE ERROR
C      IS VERY SMALL.
C
C      Y = A = SQRT(LN2)*ALFL/ALFD
C      XX = (NU-NU0)/ALFD = X/SQRT(LN2)
C
C      AN = 1/(N|*(2N+1)), N = 0,...,56
C      W6 = WEIGHT FOR 2-PT GAUSS-HERMITE QUADRATURE TIMES 2/PI
C      W1-W3 = WEIGHTS FOR 6-PT GAUSS-HERMITE QUADRATURE TIMES 2/PI
C      U6 = SQUARE OF ZERO FIXED BY 2-PT GAUSS-HERMITE QUADRATURE
C      U1-U3 = SQUARES OF ZEROES FIXED BY 6-PT GAUSS-HERMITE QUADRATURE
C      PISQ = 2/SQRT(PI); SL = SQRT(LN2); SLP = SQRT(LN2/PI)
C
C      DIMENSION AN(57)
C      DATA (AN(N),N=1,57)/1.,.33333333333333,.10,
1 .2380952380952E-01, .4629629629630E-02, .7575757575758E-03,
2 .1068376068376E-03, .1322751322751E-04, .1458916900093E-05,
3 .1450385222315E-06, .1312253296380E-07, .1089222103715E-08,
4 .8350702795147E-10, .5947794013638E-11, .3955429516459E-12,
5 .2466827010264E-13, .1448326464360E-14, .8032735012416E-16,
6 .4221407288807E-17, .2107855191442E-18, .1002516493491E-19,
7 .4551846758928E-21, .1977064753878E-22, .8230149299214E-24,
8 .3289260349176E-25, .1264107898899E-26, .4678483515519E-28,
9 .1669761793417E-29, .5754191643982E-31, .1916942862110E-32,
A .6180307588223E-34, .1930357208815E-35, .5846755007469E-37,
B .1718856062802E-38, .4908923964523E-40, .1363041261779E-41,
C .3682493515461E-43, .9687280238871E-45, .2483069097455E-46,
D .6205657919638E-48, .1513107949541E-49, .3601579309810E-51,
E .8373419683872E-53, .1902541227290E-54, .4225789754194E-56,
F .9186429502399E-58, .1954102582324E-59, .4070135277853E-61,
G .8304614505929E-63, .1660580513451E-64, .3255395462013E-66,
H .6259184116949E-68, .1180761838912E-69, .2186210422954E-71,
I .3974252722665E-73, .7095717391818E-75, .1244665977389E-76/
C
C      DATA SLP /.4697186393498/
C      DATA PISQ,SL /.128379167096, .8325546111577/
C      DATA W1,W2,W3/.4613135279626, .09999216171035,.2883893874868E-02/
C      DATA U1,U2,U3/.1901635091935, 1.784492748543, 5.525343742263/
C      DATA W6 /.5642150484/
C      DATA U6 /.5/
C
C      X = XX*SL
C      IF(XX.GT.5.9)GO TO 120
C      IF(Y.LT.1.0E-06)GO TO 130
C      IF(Y.GT.1.5)GO TO 105
C      IF(Y.LT..0005.AND.XX.LT.2.)GO TO 130
C
C      REGION ONE
C
C      S = X*X - Y*Y

```

AD-A173 633

DEVELOPMENT OF MODELS FOR INFRARED EMISSION IN THE
UPPER ATMOSPHERE(U) ARCON CORP WALTHAM MA
P P WINTERSTEINER ET AL 01 MAY 86 AFGL-TR-86-0163
F19628-84-C-0071

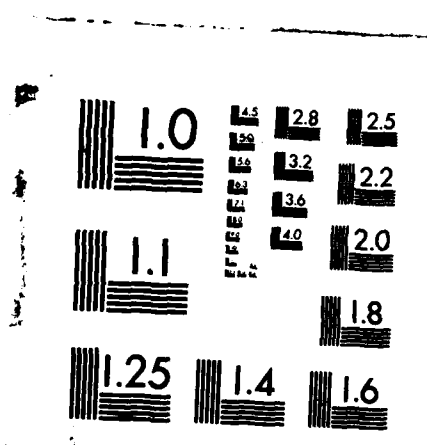
2/2

UNCLASSIFIED

F/G 4/1

NL





XEROCOPY RESOLUTION TEST CHART
NATIONAL BUREAU OF STANDARDS-1963-A

T = 2.0*X*Y

SER = Y

SEI = -X

FPR = Y

FPI = -X

NMAX = INT(8.7*XX) - 4 + 6*INT(Y)

N = 8 + 4*INT(Y)

IF(NMAX.LT.N)NMAX = N

DO 100 N = 1,NMAX

FNR = FPR*S - FPI*T

FNI = FPI*S + FPR*T

SER = SER + FNR*AN(N+1)

SEI = SEI + FNI*AN(N+1)

FPR = FNR

100 FPI = FNI

ZVGT = SLP*EXP(-S)*(COS(T)*(1.0 - PISQ*SER) - SIN(T)*PISQ*SEI)

RETURN

REGION TWO: 6-PT GAUSS-HERMITE QUADRATURE; Y>1.5

105 S = X*X - Y*Y

T = 2.0*X*Y

T2 = T*T

T = T*X

F1 = S - U1

F2 = S - U2

F3 = S - U3

ZVGT = SLP*(W1*(T - Y*F1)/(F1*F1 + T2) +

1 W2*(T - Y*F2)/(F2*F2 + T2) +

2 W3*(T - Y*F3)/(F3*F3 + T2))

RETURN

REGION THREE: 2-PT GAUSS-HERMITE QUADRATURE (FASTER THAN DOPP); XX>5.

120 T = 2.0*X*Y

SEI = T*T

T = T*X

FPR = X*X - Y*Y - U6

ZVGT = SLP*W6*(T - Y*FPR)/(FPR*FPR + SEI)

RETURN

REGION FOUR: SUBSTITUTE DOPPLER PROFILE

130 ZVGT = SLP*EXP(-X*X)

RETURN

END